12-2007

Major and Trace-Element Chemistry of Minerals in Lithologies A and B in Martian Meteorite EETA79001: Petrogenesis Revisited

Michael Joseph Mellin
University of Tennessee - Knoxville

To the Graduate Council:

I am submitting herewith a thesis written by Michael Joseph Mellin entitled "Major and Trace-Element Chemistry of Minerals in Lithologies A and B in Martian Meteorite EETA79001: Petrogenesis Revisited." I have examined the final electronic copy of this thesis for form and content and recommend that it be accepted in partial fulfillment of the requirements for the degree of Master of Science, with a major in Geology.

Lawrence A. Taylor, Major Professor

We have read this thesis and recommend its acceptance:

Harry Y. McSween, Theodore C. Labotka

Accepted for the Council:
Carolyn R. Hodges

Vice Provost and Dean of the Graduate School

(Original signatures are on file with official student records.)

To the Graduate Council:

I am submitting herewith a thesis written by Michael Joseph Mellin entitled "Major and Trace-Element Chemistry of Minerals in Lithologies A and B in Martian Meteorite EETA79001: Petrogenesis Revisited." I have examined the final electronic copy of this thesis for form and content and recommend that it be accepted in partial fulfillment of the requirements for the degree of Master of Science, with a major in Geology.

Lawrence A. Taylor

We have read this thesis
and recommend its acceptance:

Harry Y. McSween

Theodore C. Labotka

Accepted for the Council:

Carolyn R. Hodges
Vice Provost and
Dean of the
Graduate School

(Original signatures are on file with official student records.)

MAJOR AND TRACE-ELEMENT CHEMISTRY OF MINERALS IN LITHOLOGIES A AND B IN MARTIAN METEORITE EETA79001: PETROGENESIS REVISITED

A Thesis
Presented for the
Masters of Science Degree
The University of Tennessee, Knoxville

Michael Joseph Mellin
December 2007

ACKNOWLEDGEMENTS

I would like to thank the many people who assisted me with this project. Larry Taylor, Harry McSween, Yang Liu, and Darren Schnare invested countless hours and provided invaluable project guidance. It would not have been possible without their support. Allan Patchen and Marc Norman helped to obtain and interpret quality data from the electron microprobe and LA-ICP-MS. James Day procured the samples and assisted with data interpretation, and Dawn Taylor provided technical assistance. Financial support was provided by the Tennessee Space Grant Consortium. I would like to thank my amazing wife, JoEllen, for all of her encouragement.

ABSTRACT

EETA79001 is a unique shergottite composed of two mafic lithologies (termed LithA and LithB) that are separated by an igneous contact. Both lithologies have basaltic compositions; however, LithA contains megacrysts of olivine, orthopyroxenes, and chromite whereas LithB does not; also, LithA is finer-grained than LithB. Currently, the literature is in disagreement regarding the formation of this unique meteorite, especially regarding LithA. Different formational theories (e.g. fractional crystallization, magma mixing, assimilation, and impact melting) have their own constraints (chemical, thermal, or petrographic). This study uses petrographic observations combined with major- and trace- element compositions within minerals to investigate the petrogenesis of LithA. Previous formational theories are addressed and a new model is proposed.

The groundmass composition of LithA is important in explaining the relationship between megacrysts and the groundmass. Previous estimates do not consider weighted compositional averages or overgrowths on olivine megacrysts. In this study, a new estimate of the LithA groundmass composition is obtained using weighted averages of zoned minerals (major-element), and includes the overgrowth rims on megacrysts.

Here, I introduce a new LithA formational model that involves the mixing of cold megacrysts with magma. This hybrid model suggests that the interaction of the megacrysts and magma altered the heat balance and changed the crystallization sequence, as evidenced by the major-element trend in pyroxenes and the finer grain size of the LithA groundmass. The megacryst overgrowths and groundmass then crystallized, and was later followed by the removal of the late-stage fractionated melt (liquid ~Mg# 20). This new model would explain the formation of the overgrowths and avoids the heat

constraints associated with magma mixing and assimilation. However, a short-coming of this theory lies in the necessity for the late-stage removal of the last ~10% of the melt, necessary to modify the original magma composition to that of the observed LithA groundmass composition.

TABLE OF CONTENTS

LIST OF TABLES

Table Page

LIST OF FIGURES

1. INTRODUCTION

Of the tens of thousands of meteorites collected worldwide, thirty-eight have been identified as having a Martian origin, and are classified as SNC (Shergottite, Nakhlite, and Chassignite) meteorites. These meteorites are unique among the achondrite group. They are unbrecciated, tend to have a high oxidation state, show complex REE patterns, have young crystallization ages, and contain shock-implanted gases that show compositional similarities to the Martian atmosphere (Bogard and Johnson, 1983; Treiman et al., 2000). The SNC meteorites are particularly important because they are the only samples we have from Mars. They provide invaluable information about the geologic, geochemical, and atmospheric evolution of the red planet. The study of EETA79001, one of the most well-known SNC meteorites, has contributed significantly to our current knowledge of Martian petrology.

Elephant Moraine A79001 (EETA79001) may be considered the most unique SNC meteorite, because it is composed of two texturally distinct, mafic lithologies that are separated by a gradational geologic contact (McSween and Jarosewich, 1983). This 7.94 kg shergottite was discovered during the 1979 ANSMET field expedition in Antarctica. Lithology A (hereafter referred to as LithA), is classified as an olivine-phyric shergottite, whereas LithB (hereafter referred to as LithB) is a basaltic shergottite . The two lithologies show obvious differences in texture (porphyritic versus non-porphyritic for LithA and LithB respectively), and subtle differences in grain size, bulk chemistry, and mineral compositions (Steele and Smith, 1982; McSween and Jarosewich, 1983; Wadhwa et al., 1994).

The formation of the two juxtaposed lithologies is currently under debate, and numerous theories have been proposed (Ma et al., 1982; McSween, 1982; Steele and Smith, 1982; Wooden et al., 1982; McSween and Jarosewich, 1983; Nyquist et al., 1984; Nyquist et

al., 1986; Wadhwa et al., 1994; Warren, 1997; Boctor et al., 1998; Kaiden et al., 1998; Mikouchi et al., 1999; Mittlefehldt et al., 1999, Goodrich, 2003). Most formational theories have suggested an igneous origin (such as magma mixing, fractional crystallization, or assimilation), but one (Mittlefehldt et al., 1999) implied an impact melt origin.

The first model (as discussed here) suggests that LithA formed by mixing LithB magma with an ultramafic, phenocryst-bearing magma, similar in composition to a spinel-harzburgite or a lherzolitic shergottite (McSween and Jarosewich, 1983; Wadhwa et al., 1994). Mittlefehldt et al. (1999) reported that previous magma mixing models overestimated the LREE abundance in LithA, and the ultramafic endmember must be a LREE-depleted lherzolitc magma. This magma could have only formed by high degrees of melting, a process unlikely to occur because of heat constraints. Therefore, Mittlefehldt et al. (1999) argued that the magma mixing model is not plausible.

The second formational model favored assimilation of ~36% spinel-harzburgite rock by a magma having a similar composition to LithB (McSween and Jarosewich, 1983; Wadhwa et al., 1994). However, the amount of heat need to assimilate such an ultramafic material may be greater than the heat provided by the latent heat of crystallization (Wadhwa et al., 1994).

A third model suggests that LithA is an impact melt composed of a mixture of approximately 44% LithB and 56% light lithology (incompatible-element poor) ALHA77005 (Mittlefehldt et al., 1999). The LithA impact melt incorporated LithB as a clast. According to this model, the Au enrichment in the LithA groundmass indicates that the LithA groundmass is of meteoritic origin. However, Warren and Kallemeyn (1997) state that the Au does not correlate with Ir, so the Au enrichment is most likely terrestrial contamination.

The fourth formational model states that LithA formed by various degrees of partial melting of a peridotite source rock (McSween and Jarosewich, 1983). According to the partial melting model, the megacrysts originated from the residue of the partial melt. A strong argument against this model contends that garnet exists in the shergottite source region (Ma et al., 1981; Wooden et al., 1982), and the chromium megacrysts found in LithA are unlikely to occur with garnet (McSween and Jarosewich, 1983).

Finally, the possibility that LithA and LithB formed by fractional crystallization of a common parent melt has been considered. McSween and Jarosewich (1983) and Ma et al. (1982) discounted this theory because the olivine and orthopyroxene megacrysts were believed to be out of equilibrium with the groundmass. Also, Goodrich (2003) used the quartz-olivine-plagioclase phase system to demonstrate that the LithA whole-rock composition (Mg# 61) "does not become cosaturated with orthopyroxene until ~26% olivine has crystallized". Therefore, the olivine and orthopyroxene megacrysts cannot be in equilibrium with a melt having this whole-rock composition.

In the present study, we approach the petrogenesis of these two lithologies by analyzing major- and trace-element variations within minerals obtained by electron microprobe analysis (EMP) and laser-ablation inductively-coupled-plasma mass-spectrometry (LA-ICP-MS). Specifically, this study addresses the nature of the relationship between the megacrysts in LithA and its groundmass, and the relationship between lithologies A and B.

2. METHODOLOGY

Six polished sections (four thin and two thick) were obtained from NASA Johnson Space Center Astromaterials Curation. Two sections were cut from LithA (,616; ,439), two from LithB (,457; ,392), and two at the contact between the lithologies (,615; ,39). All slides range in surface area from 50-78 mm^2, except ,39, which has a surface area of approximately 170 mm^2. The initial petrography of each section was examined using a petrographic microscope. Crystal sizes were determined optically by averaging two perpendicular measurements of crystal diameters. Up to 20 crystals per mineral were measured.

A Cameca SX-50 electron microprobe (EMP) was used to obtain major-element chemistry on minerals. All minerals (except maskelynite and glass) were examined using an excitation voltage of 15 keV, a beam current of 20 nA, and a spot size of 1 μm. To reduce Na loss, maskelynite and glass were examined using a beam current of 10 nA and a spot size of 5 μm. Standard PAP corrections were used to remove matrix effects. The detection limits (3σ above background) for SiO_2, TiO_2, Al_2O_3, MgO, CaO, Na_2O, K_2O, and Cl are <0.03 wt%. For Cr_2O_3, MnO, FeO, P_2O_5, NiO, and Co, the detection limits are <0.05 wt%. All other oxides and elements have detection limits between <0.05-0.1 wt%.

Modes were obtained on all sections using an Oxford Instrument energy dispersive spectrometer (EDS), coupled to the EMP. Modal analyses acquisition used an excitation voltage of 15 keV, a beam current of 20 nA, a spot size of 1 μm, 70 msec counting time, and a step-size of 4 μm. A total of ~250,000 points per slide were analyzed, using the *Feature Scan Phase Distribution Software* (developed by Oxford Instruments) and following the procedure of Taylor et al. (1996).

Trace-element abundances of all minerals and melt veins in the thick sections (LithA, 616; and LithB, 615) were analyzed *in-situ* using a laser-ablation, inductively-coupled-plasma mass-spectrometer (LA-ICP-MS) at the Australian National University in Canberra, Australia. Trace-element data were obtained by following the analytical procedure of Norman et al. (1996). Laser ablation was performed using a 193 nm Excimer UV laser system utilizing a 25% reduction mirror. The laser beam spot size ranged between 24-54 μm with a repetition rate set at either 5 Hz or 10Hz**.** Each analysis totaled 60 sec, and included 20 sec for background acquisition followed by 40 sec of ablation. Each ablated spot resulted in a circular hole having a depth of 20 to 40 μm, depending on the spot size and laser-repetition rate. Ablation was performed under an argon atmosphere, and the ablated product was transported to the ICP-MS by an argon-helium gas flow.

A NIST 612 glass was used as a calibration standard along with the following USGS basaltic glass standards: TB-1G, BIR-1G, BCR-2G, and BHVO-2G. The detection limits were calculated by Lamtrace, a software program developed by Simon Jackson at Macquarie University, Sydney, Australia. The detection limits were calculated following the method of Longerich et al. (1996). The amount of ablation product varied for each spot analyzed; therefore, detection limits were calculated after every analysis. The average detection limits for all elements analyzed (calculated at 3σ of the sample) are listed as follows: <0.02 wt % for Na_2O, MgO, Al_2O_3, SiO_2, CaO, and FeO; 0.01 -0.06 ppm for Mn, Co, Ga, Rb, Sr, Y, Zr, Nb, Ba, La, Ce, Pr, Nd, Sm, Eu, Tb, Gd, Dy, Ho, Er, Yb, Lu, Hf, Ta, Pb, Th, Cs, and V; 0.13-0.16 ppm for Sc and Zr; and 0.2-1.0 ppm for Ni and Ti. The resulting time-resolved data were reduced using Lamtrace. This program allowed for the adjustment of the integration interval for each ablated spot and assured that the data represents the ablation of one mineral.

Finally, each ablation spot was normalized to the corresponding EMP analysis using wt% CaO for pyroxene, maskelynite, glass, and phosphate, and wt% FeO for olivine, chromite, ilmenite, and pyrrohotite.

3. PETROGRAPHY AND COMPOSITION

The petrography, modal abundances, and major-element compositions of minerals are discussed below. Mineral modal abundances (Table 1) were determined for all sections; however, only the sections that do not contain the contact are compared to values obtained by previous studies (McSween and Jarosewich, 1983; Schwandt et al., 2001). This is because the sections that contain the contact have the largest variations in mineral modes, and may not be representative of each lithology as a whole. We report the major-element compositions of minerals from all six sections (summarized in Table 2) because the actual mineral compositions do not appear to vary with distance from the contact. These modal and major-element observations are supported by the EMP and modal analysis work by Steele and Smith (1982) and McSween and Jarosewich (1983).

3.1 Lithology A

LithA is a porphyritic basalt that contains megacrysts of olivine, orthopyroxene, and chromite. The groundmass is comprised of pyroxene (mainly pigeonite), maskelynite, chromite, ilmenite, pyrrohotite, whitlockite, ulvöspinel, and a silica phase (possibly tridymite?). The LithA groundmass crystals are finer-grained than the crystals in LithB.

Lithology A Megacryst Assemblage

The LithA megacrysts (in the analyzed sections) exist as large individual crystals (Fig. 1 a-c), although a few clusters of two or more olivine megacrysts have been identified. Previous studies (Steele and Smith, 1982; McSween and Jarosewich, 1983) reported areas of composite megacrysts of olivine and orthopyroxene, which were interpreted

Table 1. Average modal abundances of LithA and B.

Section #	pig	aug	opx	mask	ol	whit	po	chr	sil	il	usp
Mellin (LithA Megacrysts + Groundmass)											
,616 (A)	60.4	5.47	2.08	21.1	8.02	1.73	0.35	0.30	0.02	0.34	0.24
,439 (A)	58.0	5.25	5.04	17.8	10.8	1.64	0.41	0.42	0.01	0.34	0.23
Average	59.2	5.36	3.56	19.5	9.43	1.68	0.38	0.36	0.01	0.34	0.23
Mellin (LithA Groundmass Only)											
,616 (A)	66.4	6.01	1.02	23.3	0.23	1.90	0.39	0.10	0.02	0.38	0.26
,439 (A)	68.2	6.20	1.05	21.2	0.05	1.93	0.48	0.20	0.01	0.40	0.27
Average	67.3	6.11	1.04	22.3	0.14	1.92	0.44	0.15	0.02	0.39	0.27
Mellin (LithB)											
,392 (B)	37.0	11.8	0.08	44.4	0.00	3.75	0.39	0.00	0.84	0.87	0.80
,457 (B)	57.9	7.35	1.14	29.4	0.02	2.55	0.48	0.06	0.24	0.55	0.31
Average	47.5	9.59	0.61	36.9	0.01	3.15	0.44	0.03	0.54	0.71	0.56

McSween and Jarosewich (1983)

	pig	aug	opx	mask	ol	whit	meso	opaq
,75 (A)	62.8	3.20	3.40	18.3	10.3	trace	0.00	2.20
,68 (A)	60.7	6.50	5.70	15.9	7.20	trace	trace	4.00
,79 (A), 80 (A)	54.5	8.50	7.2	17.0	9.10	0.40	0.30	3.00
*Average	61.8	4.85	4.55	17.1	8.75	0.40	0.00	3.10
,79 (B), 80 (B)	54.4	11.6	0.00	28.2	0.00	0.70	1.10	3.40
,71 (B)	32.2	23.9	0.00	29.4	0.00	0.20	0.50	3.80
,69 (B)	31.8	24.5	0.00	29.6	0.00	0.20	0.50	3.40
*Average	43.3	17.8	0.00	28.8	0.00	0.45	0.80	3.60

Schwandt et al. (2001)

	pig	aug	opx	mask	ol	whit	meso	opaq
,68 (A)	42.0	18.0	3.00	22.0	10.0	2.00	0.00	3.00

*Only thin sections ,75, 68, 71, and ,69 are included because the exact location of the gradational geologic contact is subjective and abundances may not be representative

Mineral Abbreviations: pig - pigeonite, aug - augite, opx - orthopyroxene, mask - maskelynite, ol - olivine, whit - whitlockite, po - pyrrhotite, chr - chromite, sil - silica, il - ilmenite, usp - ulvospinel, opq - opaques, meso - mesostasis

Table 2. Major-element compositional ranges for all phases in LithA and B, obtained from EMP analyses.

Phase	Pigeonite				Augite				Opx				Olivine		Chromite		Maskelynite				Ilmenite		Ulvöspinel		Silica	
	core	rim	core	rim	core	rim	core	rim	core	rim	core	rim	core	rim	core	rim	core	rim	core	rim						
Lith.	A	A	B	B	A	A	B	B	*A	*A	B	B	*A	*A	*A	*A	A	A	B	B	A	B	A	B	A	B
wt%																										
SiO2	54.1	49.7	53.4	47.8	52.8	49.2	52.3	49.9	53.9	49.9	54.2	49.1	38.0	34.6	0.16	0.03	52.6	56.4	52.6	57.1	0.06	0.03	0.05	0.09	96.8	95.9
TiO2	0.13	0.45	0.12	0.80	0.24	0.94	0.28	0.58	0.05	0.96	0.07	0.76	–	–	0.67	16.5	–	–	–	–	52.0	51.9	29.3	27.6	0.32	–
Al2O3	0.32	0.95	0.74	0.67	1.45	1.04	1.48	1.05	0.56	0.76	0.47	1.31	–	–	9.39	4.24	29.0	27.3	29.8	26.2	0.00	0.07	1.51	1.78	2.0	1.6
Cr2O3	0.52	0.36	0.49	0.08	0.60	0.19	0.88	0.13	0.55	0.06	0.51	0.35	0.15	0.08	54.8	26.6	–	–	–	–	0.38	0.01	0.74	0.53	–	–
MgO	25.1	12.4	23.2	8.1	16.9	10.0	17.4	12.2	25.9	12.7	26.2	12.0	38.3	23.4	4.81	2.90	0.10	0.06	0.17	0.04	1.76	0.14	0.60	0.35	0.00	0.02
CaO	3.43	6.98	4.24	7.39	15.4	14.5	14.7	13.0	2.15	8.48	2.04	9.70	0.33	0.22	0.01	0.08	12.6	9.7	13.0	9.2	0.09	0.02	0.02	0.01	0.39	0.30
MnO	0.59	0.68	0.56	0.78	0.47	0.66	0.48	0.57	0.48	0.70	0.50	0.72	0.46	0.78	0.44	0.52	–	–	–	–	0.69	0.64	0.66	0.58	–	–
FeO	16.3	27.7	17.3	33.0	12.8	22.9	12.4	21.3	15.3	26.2	15.0	25.1	21.4	41.2	27.7	46.5	0.75	0.63	0.52	0.78	44.1	46.6	65.9	66.7	0.27	0.19
Na2O	0.04	0.09	0.05	0.07	0.15	0.12	0.17	0.10	0.03	0.07	0.03	0.11	–	–	–	–	4.08	5.54	3.84	5.71	–	–	–	–	0.13	0.45
K2O	–	–	–	–	–	–	–	–	–	–	–	–	–	–	–	–	0.12	0.27	0.07	0.68	–	–	–	–	–	–
Total	100.5	99.3	100.0	98.7	100.8	99.5	100.0	98.8	99.0	99.8	99.1	99.2	98.7	100.3	97.9	97.4	99.2	99.9	100.0	99.7	99.1	99.5	98.8	97.7	99.9	98.5
Si	1.97	1.96	1.97	1.96	1.95	1.94	1.95	1.96	1.98	1.96	1.98	1.94	1.00	0.99	0.01	0.00	2.41	2.54	2.39	2.58	0.00	0.00	0.00	0.00	0.98	0.98
Ti	0.00	0.01	0.00	0.03	0.01	0.03	0.01	0.02	0.00	0.03	0.00	0.02	–	–	0.02	0.46	–	–	–	–	0.99	0.99	0.85	0.81	0.00	–
Al	0.01	0.04	0.03	0.03	0.06	0.05	0.07	0.05	0.02	0.04	0.02	0.06	–	–	0.39	0.18	1.56	1.45	1.59	1.40	0.00	0.00	0.07	0.08	0.02	0.02
Cr	0.02	0.01	0.01	0.00	0.02	0.01	0.03	0.00	0.02	0.00	0.02	0.01	0.00	0.00	1.52	0.78	–	–	–	–	0.01	0.00	0.02	0.02	–	–
Mg	1.36	0.73	1.27	0.50	0.93	0.59	0.96	0.71	1.42	0.74	1.43	0.71	1.50	1.00	0.25	0.16	0.01	0.00	0.01	0.00	0.07	0.01	0.03	0.02	0.00	0.00
Ca	0.13	0.30	0.17	0.32	0.61	0.61	0.59	0.55	0.08	0.36	0.08	0.41	0.01	0.01	0.00	0.00	0.62	0.47	0.63	0.45	0.00	0.00	0.00	0.00	0.00	0.00
Mn	0.02	0.02	0.02	0.03	0.02	0.02	0.02	0.02	0.02	0.02	0.02	0.02	0.01	0.02	0.01	0.02	–	–	–	–	0.02	0.01	0.02	0.02	–	–
Fe	0.50	0.92	0.53	1.13	0.40	0.76	0.39	0.70	0.47	0.86	0.46	0.83	0.47	0.99	0.81	1.43	0.03	0.02	0.02	0.03	0.93	0.99	2.11	2.18	0.00	0.00
Na	0.00	0.01	0.00	0.01	0.01	0.01	0.01	0.01	0.00	0.01	0.00	0.01	–	–	–	–	0.36	0.48	0.34	0.50	–	–	–	–	0.00	0.01
K	–	–	–	–	–	–	–	–	–	–	–	–	–	–	–	–	0.01	0.02	0.00	0.04	–	–	–	–	–	–
Total	4.01	4.00	4.01	4.00	4.01	4.01	4.01	4.01	4.00	4.00	4.00	4.01	3.00	3.01	3.01	3.03	5.00	4.99	4.99	4.99	2.01	2.00	3.11	3.13	1.01	1.01
Mg#	73.1	44.3	70.5	30.6	69.9	43.7	71.4	50.5	75.1	46.3	75.7	46.0	76.1	50.3	23.6	10.0										
%An																	62.6	48.5	64.9	45.2						
Wo	6.53	15.3	8.51	16.6	31.4	31.3	30.2	27.9	4.27	18.2	4.07	21.1														
En	68.3	37.5	64.5	25.5	47.9	30.1	49.8	36.4	71.9	37.8	72.6	36.3														
Fs	25.1	47.2	27.0	57.9	20.6	38.7	19.9	35.7	23.9	43.9	23.3	42.6														

* Megacrysts

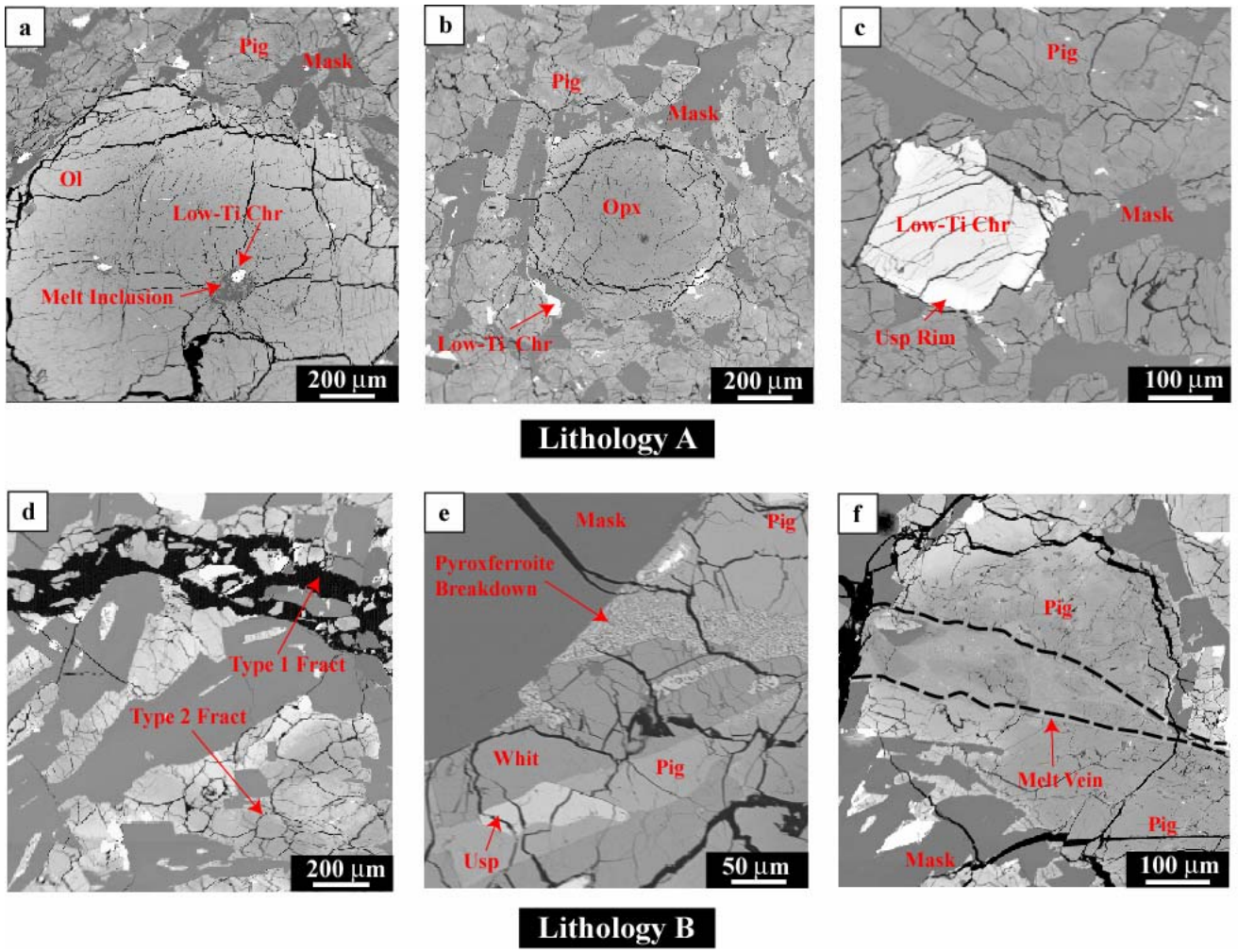

Figure 1. BSE images of LithA and B. (a-c) show LithA megacrysts of (a) olivine (b) orthopyroxene and (c) chromite. Features found in both lithologies include (d) Type 1 and Type 2 fractures, (e) pyroxferroite breakdown textures, and (f) melt vein (outlined)

to be xenoliths. This type of megacryst clustering is not observed in the sections analyzed for this study.

The abundance of megacrysts (olivine plus orthopyroxene) in the LithA sections (Table 1) ranges from 9.1 to 14.8 vol%. The large size of the megacrysts (> 0.5 mm) suggests that this variation may be due to a sampling effect. The reported abundances of olivine and orthopyroxene megacrysts from McSween and Jarosewich (1983) (excluding the contact-bearing slides ,79 and ,80), however, show only slight variations that range between 12.9-13.7 vol%. The differences in megacryst abundance between this study and McSween and Jarosewich (1983) may be due to differences in analytical technique. This study obtained mineral abundances by image processing of BSE maps while McSween and Jarosewich (1983) used a point-counting method. Chromite megacrysts in the analyzed sections, however, only vary in abundance from 0.20-0.22 vol%.

The olivine megacrysts are large (1-3mm) subhedral to anhedral grains with irregular crystal boundaries which may be the result of shear deformation due to shock (Goodrich 2003) or resorption (Steele and Smith 1982). Shock veins and microfaults were reported in the olivine megacrysts by Goodrich (2003), and the presence of these features is confirmed in this study. Some olivine-crystal shapes are difficult to distinguish because these megacrysts display extensive shock-induced fracturing at the contact of the megacryst with the groundmass.

Olivine megacrysts (in the analyzed sections) are commonly zoned from Mg-rich (Fo_{76}) cores to Fe-rich (Fo_{50}) rims (Fig. 2c). Steele and Smith (1982), however, reported olivine megacryst compositions of up to Fo_{81}. Calcium contents in

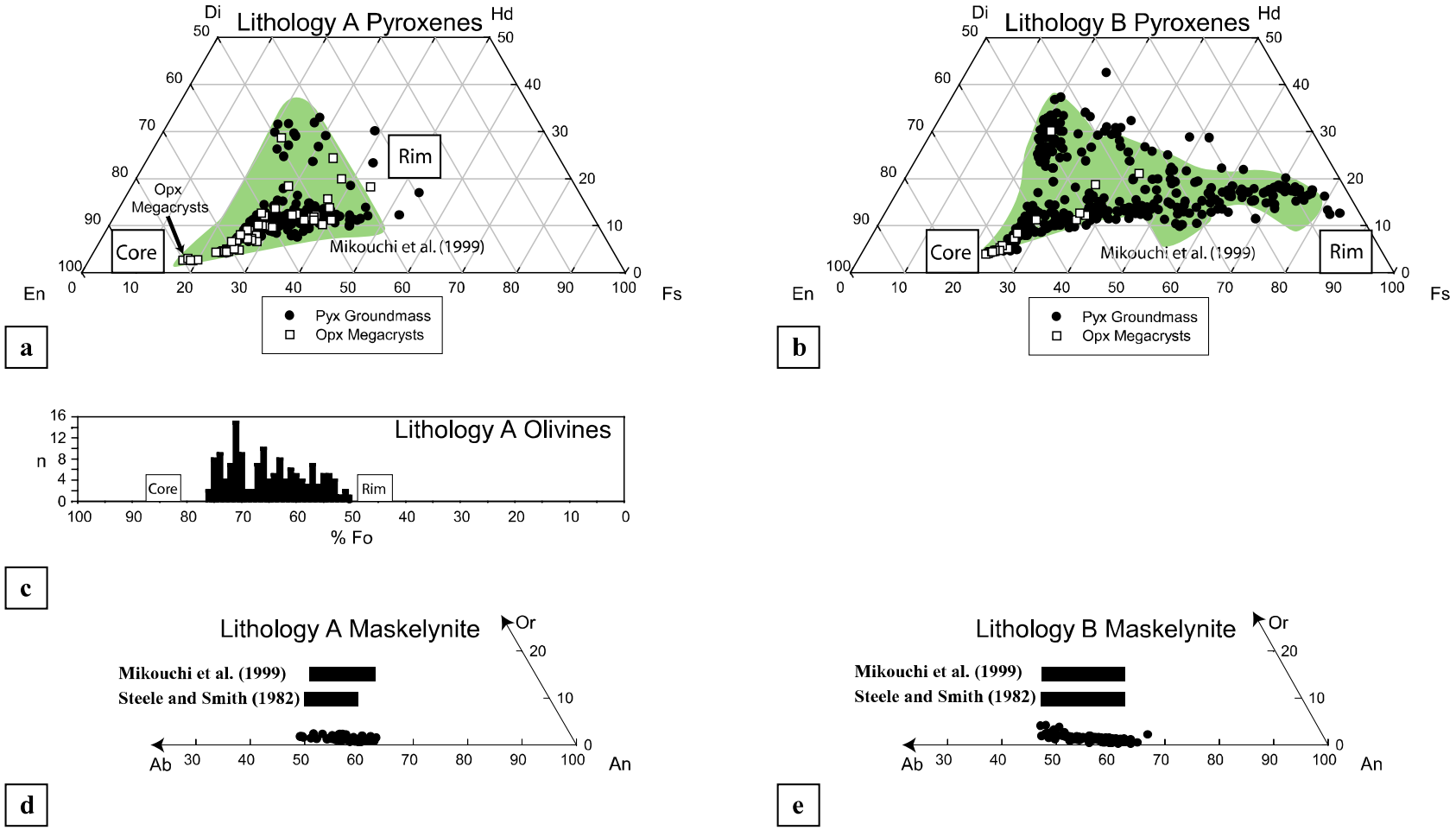

Figure 2. Mineral compositions for pyroxene, olivine, and maskelynite in lithologies A and B. Pyroxene data are compared to values (solid field) obtained from Mikouchi et al. (1999).

three olivine megacrysts are plotted relative to distance from the rim in Figs. 3a-c. These figures show an enrichment of CaO at the rim (or overgrowth) having a thickness of 100-200 μm. Plotting calcium versus forsterite content (Fig. 3d) shows that enrichment starts at a composition of ~Fo69. Interestingly, a similar enrichment was also reported in another olivine-phyric shergottite, Yamato 980459 (Usui et al., 2007).

The pyroxene megacrysts in LithA (Fig. 1b) range in size from 0.5 mm to 1 mm and have subhedral to anhedral shapes. These megacrysts are zoned with orthopyroxene composing the core ($En_{72}Fs_{24}Wo_4$), and pigeonite ($En_{55}Fs_{33}Wo_{12}$) or augite ($En_{48}Fs_{23}Wo_{29}$) composing the rim (Fig. 2a). The composition of the pigeonite rimming the orthopyroxene core is similar to the composition of the groundmass pyroxenes. Chromite inclusions are found in the orthopyroxene and, less commonly, in the olivine megacrysts.

Chromite megacrysts exist only in LithA, have diameters >100 μm (e.g. Fig. 1c), and have subhedral to anhedral crystal boundaries. These megacrysts have low-Ti cores and ulvöspinel-rich rims (Fig. 4). The ulvöspinel rims have a lower-Ti composition compared to ulvöspinel in the groundmass. The chromite cores show extensive fracturing; however, this texture terminates at the core/rim boundary.

Lithology A Groundmass

The LithA groundmass pyroxenes have an average crystal size of 0.29 mm (Table 3), and have complex Mg-Fe zoning patterns from core to rim. A Ti-Al plot (Fig. 5a) of groundmass pyroxenes and orthopyroxene megacrysts show that they initially crystallize along a 1:6 slope; however, plagioclase crystallization begins when the Al

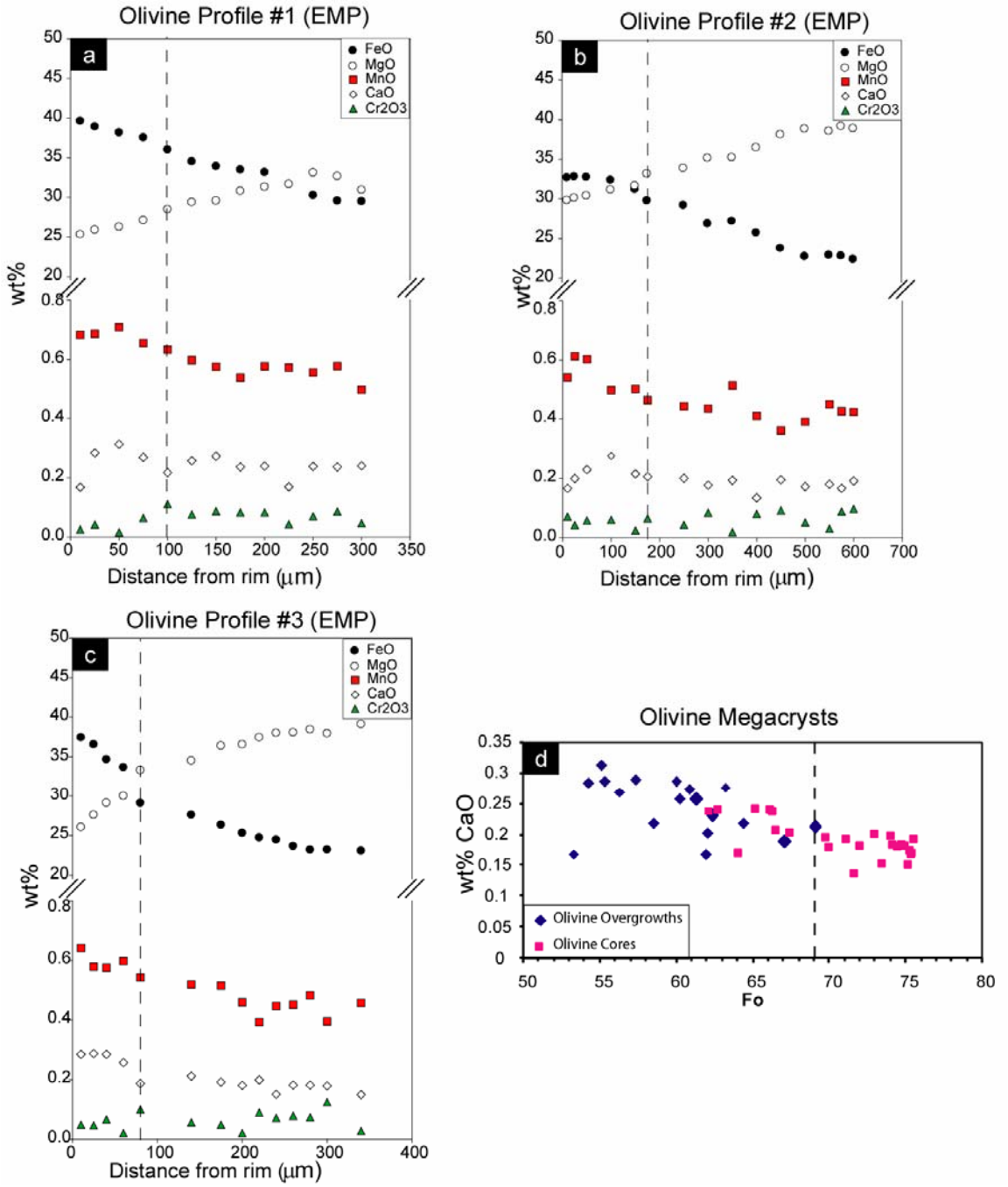

Figure 3. (a-c) Major-element distribution profiles of selected olivine megacrysts. Olivine rims show thicknesses that range from ~80-200 μm. Major-element enrichments are interpreted to start at the location of the vertical dashed line. (d) A plot of wt% CaO vs Fo, shows CaO enrichments begin at approximately Fo 69. All values (a-d) are obtained by EMP

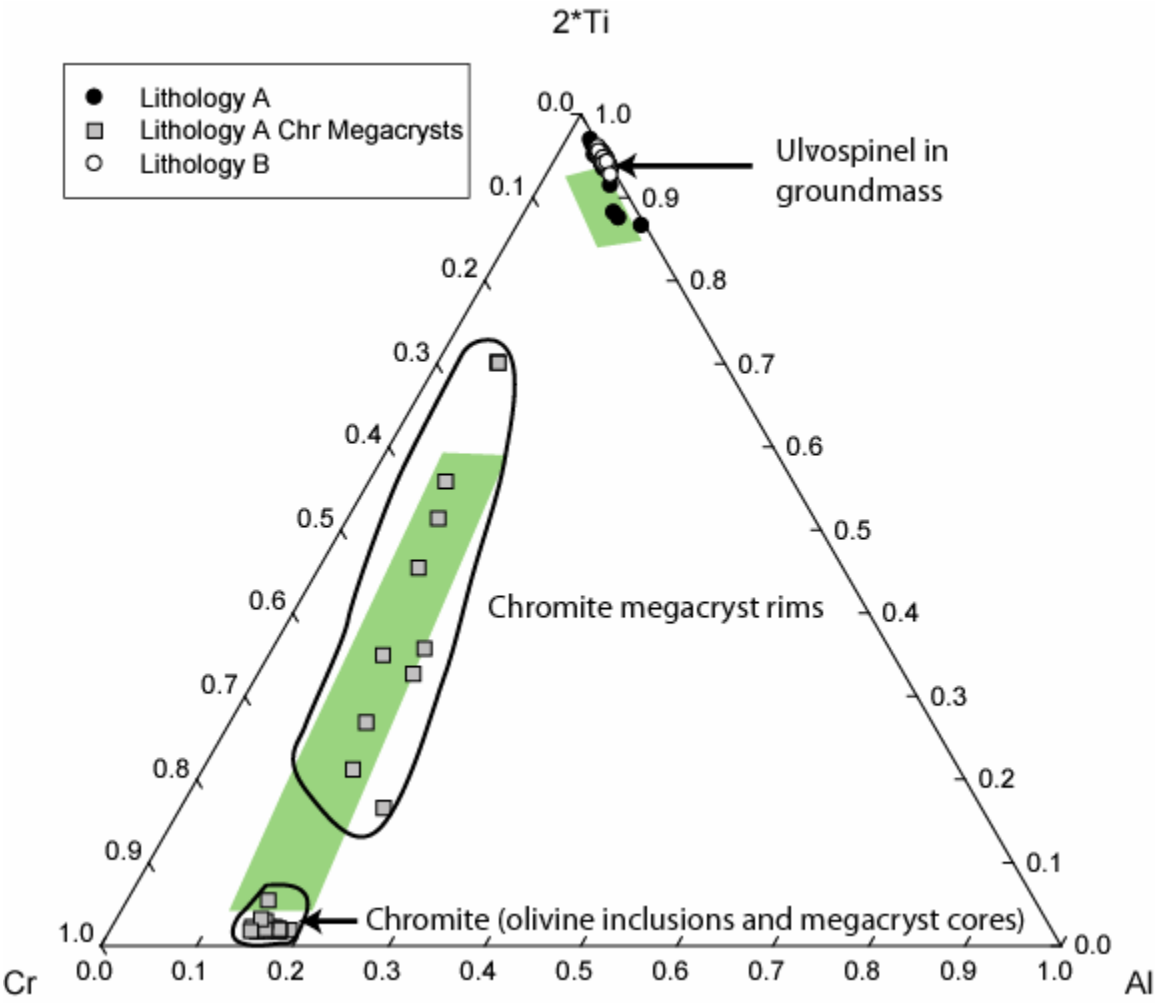

Figure 4. Plot of spinel compositions in LithA and B. Chromite megacrysts have high-Ti rims that trend toward ulvöspinel. Shaded region represent values obtained by McSween and Jarosewich (1983).

Table 3. Average crystal sizes of selected minerals in LithA and LithB.

Lithology A	Mean Crystal Size (mm)				
	616 (A)	439 (A)	39 (A)	615 (A)	Average
Oliv megacryst	1.16	1.18	0.91	0.69	0.99
Opx megacryst	0.77	0.77	0.50	0.52	0.64
Chrom megacryst	0.17	0.10	0.15	0.12	0.14
Pyx groundmass	0.25	0.27	0.31	0.32	0.29
Maskelynite	0.19	0.14	0.29	0.27	0.22

Lithology B	Mean Crystal Size (mm)				
	39 (B)	615 (B)	457 (B)	392 (B)	Average
Pyxroxene	0.42	0.37	0.58	0.46	0.46
Maskelynite	0.61	0.33	0.49	0.62	0.51
Opx crystals	–	–	0.83	–	0.83

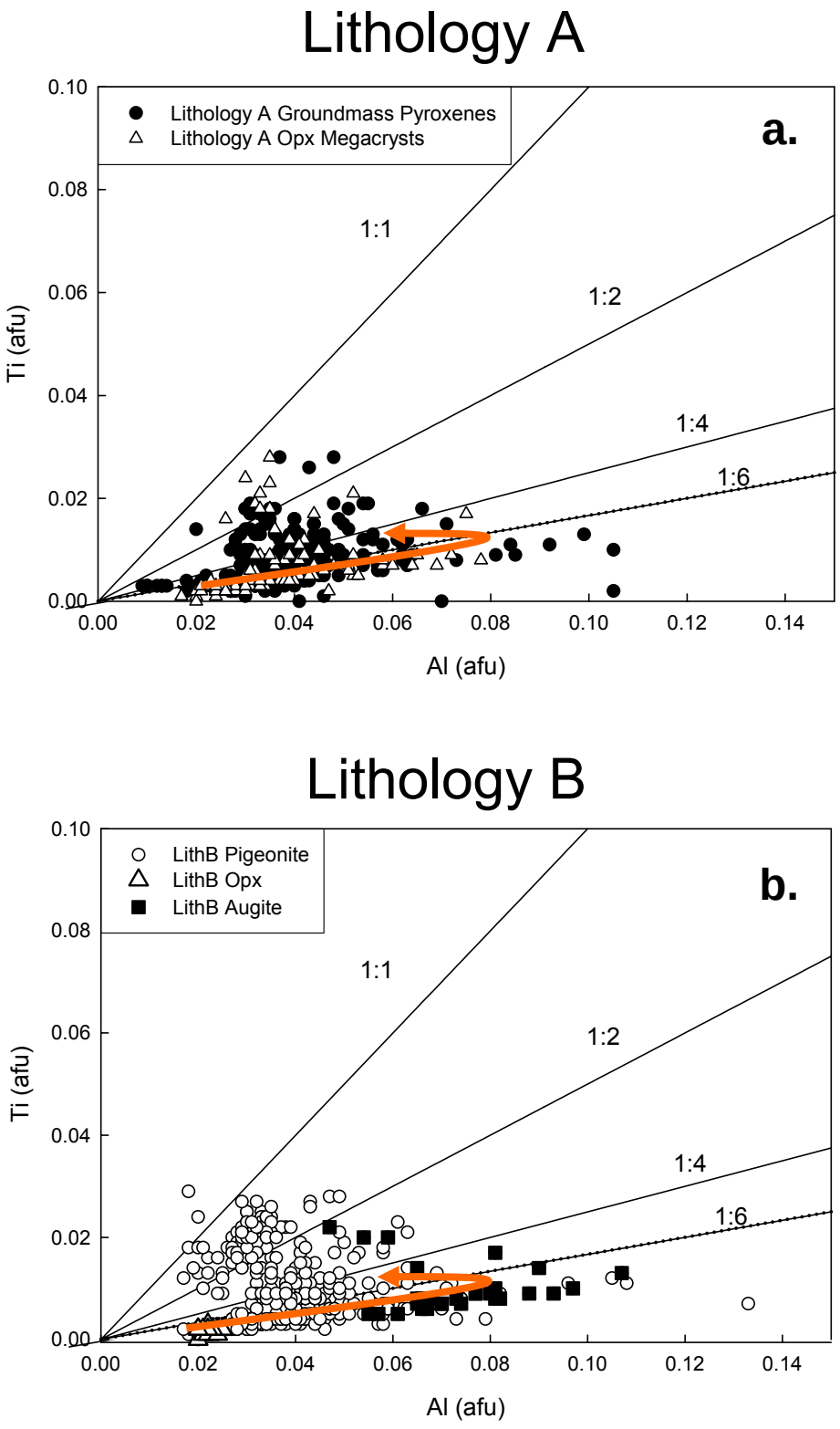

Figure 5. Pyroxene compositions of Ti versus Al of LithA and B (afu-atomic formula units). Arrow denotes crystallization trend. Values obtained from EMP analysis.

concentration of the residual melt reaches 0.105 afu and 0.08 afu for pyroxene groundmass and orthopyroxene megacrysts, respectively. Interestingly, the pyroxenes in the LithA groundmass and LithB (Fig. 5a and 5b) show similar crystallization trends.

Plagioclase grains in LithA have been transformed to maskelynite as a result of intense shock. Maskelynites are lath-shaped, with no preferential orientation, and show compositional zonations from An_{63} in the core to An_{49} in the rim (Fig. 2d), consistent with results of Mikouchi et al. (1999).

Chromite crystals in the groundmass and chromite inclusions within other megacrysts are uniformly low in Ti. Ilmenite, ulvöspinel, and pyrrhotite generally occur as subhedral crystals that are <100 μm in size, and show no chemical zoning from core to rim. Whitlockite occurs as subhedral crystals, <200 μm, and is typically bounded by pyroxene and maskelynite.

3.2 Lithology B

LithB is a non-porphyritic basalt composed of augite, pigeonite, maskelynite, ilmenite, whitlockite, ulvöspinel, and a silica phase (tridymite?). It is more coarse-grained than LithA and has crystal sizes that range from 0.33-0.83 mm, whereas LithA crystal sizes range from 0.14-0.32 mm (Table 3).

The LithB sections studied here generally have a higher abundance of pigeonite and lower abundance of augite than reported by McSween and Jarosewich (1983). These differences may be due to the use of an alternate method of obtaining modes. McSween and Jarosewich (1983) used the optical point counting method. The x-ray digital modal-analysis technique used in the present study is more exacting than optical techniques in mineral identification. However, if the total vol% of pigeonite + augite in the LithA

sections studied here is compared to the total vol% of pigeonite + augite determined by McSween and Jarosewich (1983), the results are similar (64.6% and 66.7%, respectively).

The LithB pyroxenes have compositions that range from Mg-rich pigeonite cores to Fe-rich pigeonite or augite rims (Fig. 2b). These Fe-rich rims extend into the "forbidden region," which is common of basalts that have undergone extreme differentiation. This is not observed in pyroxenes in LithA. Also, pyroxferroite breakdown textures (Fig. 1e) exist in the LithB groundmass. Bladed maskelynite crystals are similar in composition to those in LithA and other studies (Fig.2e). LithB maskelynite display wider compositional variation (An_{65-45}) relative to maskelynites in LithA (An_{63-49}). Ulvöspinel, ilmenite and pyrrhotite show similar characteristics to those reported in LithA.

The analyzed sections reveal distinctive features that have been previously unreported. Contrary to previous studies (Steele and Smith, 1982; McSween and Jarosewich 1983; Mikouchi et al., 1999; Goodrich, 2003), large orthopyroxene crystals were observed in LithB section ,457. These crystals have similar compositions and abundances as the orthopyroxene megacrysts in LithA (Tables 1 and 2, Fig. 2b). These orthopyroxenes occur as subhedral grains (0.5–1.2 mm). Melt inclusions may exist in the largest orthopyroxene crystals (>1.0 mm). These crystals are zoned from Wo_4En_{73} in the cores, and are rimmed by pigeonite having a composition of $Wo_{21}En_{36}$. Other than the presence of orthopyroxene crystals, thin-section ,457 resembles the other LithB sections (in mineral abundance and compositions) analyzed in this study.

Shock Features

Evidence of shock deformation includes numerous fractures and melt veins that cross-cut all minerals in both lithologies (Fig. 1d and 1f). Intense fracturing occurs on both large and small scales. Type 1 fractures are laterally continuous, often dendritic, and have depths that extend through the bottom of the cut section. Type 2 fractures are abundant in all minerals, except maskelynite and silica. These fractures are less than 5 μm in width, are bounded by the minerals occupied, and often result in the formation of polygonal units within the minerals. Melt veins are often linear and non-branching. They may extend for several millimeters and have variable widths that range between 10 and 50 μm. Many areas within the glass veins (especially near the edges) show a heterogeneous mixture of partially melted minerals such as pyroxene and maskelynite, as seen in Fig. 1f.

All lithologies in EETA79001 show evidence of intensive-shock metamorphism (Bocter et al., 1998). Pyroxenes display shock twinning, and olivines possess patchy extinction and strong mosaicism (Steele and Smith, 1982; McSween and Jarosewich, 1983). Pockets and veins of impact-generated melt occupy lithologies A and B, and plagioclase from both lithologies has been converted to maskelynite (Steele and Smith, 1982; McSween and Jarosewich, 1983). It is estimated that EETA79001 has experienced shock pressures of approximately 34 ±2 GPa (Lambert, 1985).

Mikouchi et al., (1999) reported compositional lamellae in some pyroxenes in LithA groundmass and LithB. The lamellae were described as having widths and spacing on the nanometer scale and are not observed optically or in back-scattered-electron imaging. Shock lamellae (Fig. 6) exist in pyroxenes of both lithologies, but tend to be

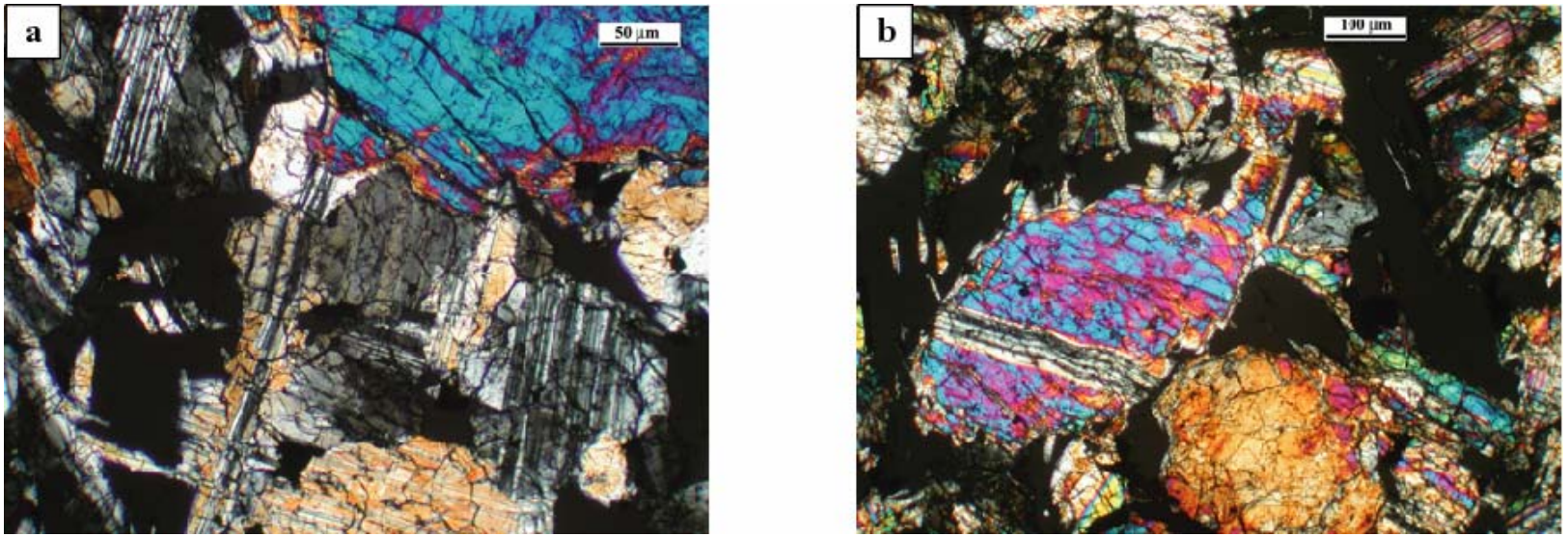

Figure 6. Shock lamellae in pyroxenes in (a) lithology A, and (b) lithology B. EMP analyses reveal no major-element variation among lamellae.

more prevalent in lithology A. All lamellae rarely exceed widths of 50 μm and may have a slight curvature as shown in Fig. 6b. Pyroxenes and olivines show undulatory extinction, a feature reported in other shergottites (Steele and Smith, 1982, Kaiden et al., 1998).

3.3 Trace-Element Composition

Pyroxene REE patterns (CI-normalized) for lithologies A and B are displayed in Fig. 7. Both lithologies display typical concave-downward patterns, with distinct LREE-depletions, slight HREE-enrichments, and weak negative-Eu anomalies. The REE concentrations progressively increase with Ca and Fe enrichment, consistent with fractional crystallization. Figure 8 shows the range of pyroxene compositions that were sampled by LA-ICP-MS. Pyroxenes with similar compositions in LithA and LithB show strong similarities in their REE patterns, a fact well illustrated by a La/Sm versus La/Yb plot (Fig 9). It is expected that the extremely fractionated pyroxenes in LithB (Fe-rich pigeonite) contain highly enriched REEs. This is not shown in Fig. 8 because the beam spot used in our LA-ICP-MS analysis (54 μm) was larger than the Fe-rich rim analyzed. The REE patterns overlap data from Wadhwa et al. (1994) for pyroxenes with similar compositions.

Figure 10 shows REE patterns from LithA and LithB maskelynite. These patterns display typically strong positive-Eu anomalies and have relatively constant concentrations from LREE to HREE. The patterns become enriched with decreasing An content, as expected from studies of REE behavior by Jones (1995). The analyzed sections from this study show a higher average Eu anomaly than reported in Wadhwa et al. (1994).

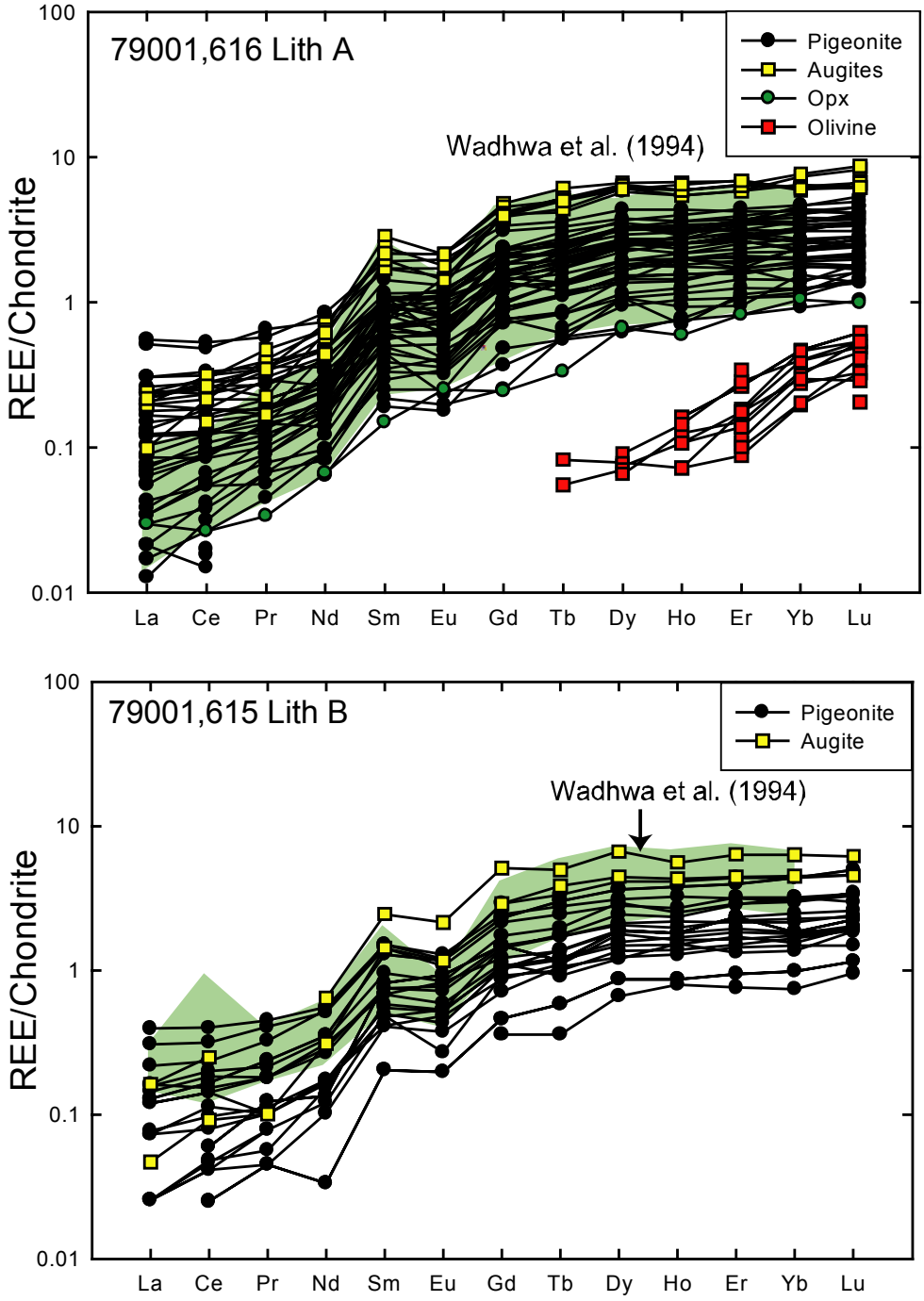

Figure 7. Normalized REE plots of (a) LithA pyroxene and olivine and (b) LithB pyroxene. The shaded region in both plots show the compositional range for low and high Ca pyroxenes from Wadhwa et al. (1994). The REE patterns are normalized to primitive CI carbonaceous chondrite using the values of Anders and Grevesse (1989).

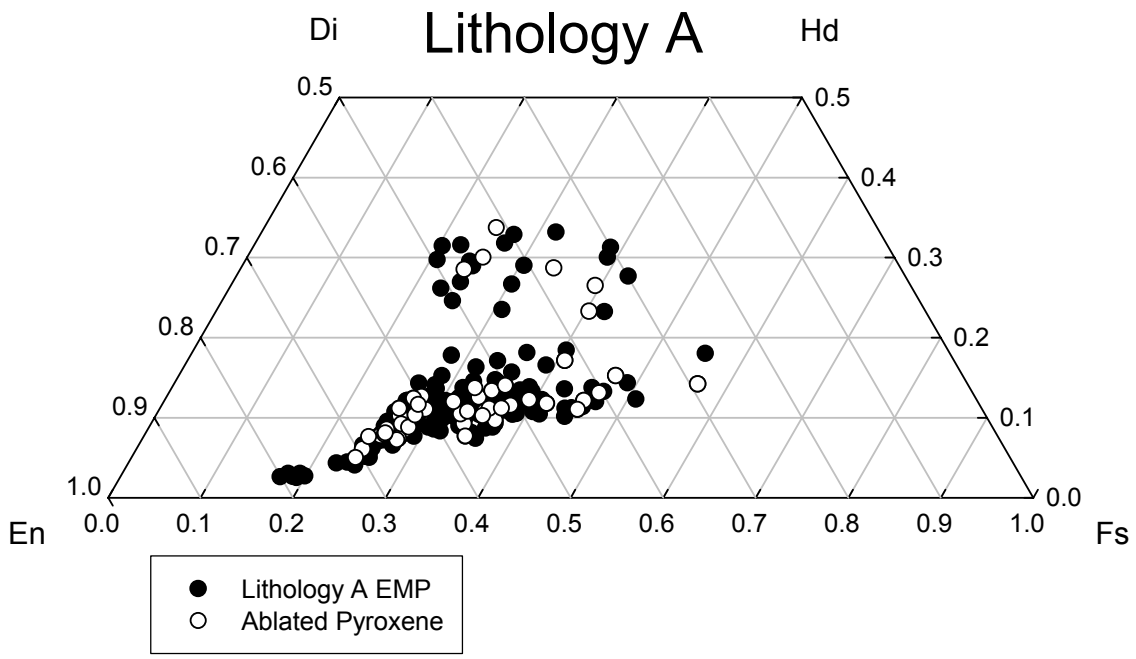

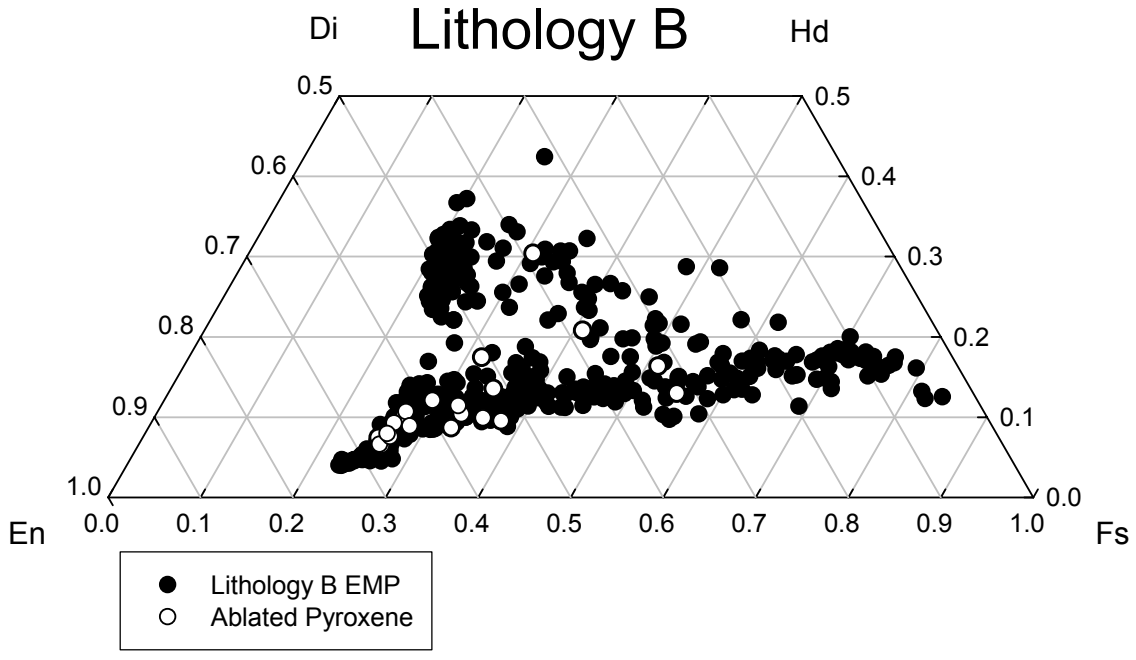

Figure 8. Locations of all pyroxene compositions analyzed by EMP (closed circles) and LA-ICP-MS (open circles) for lithologies A and B.

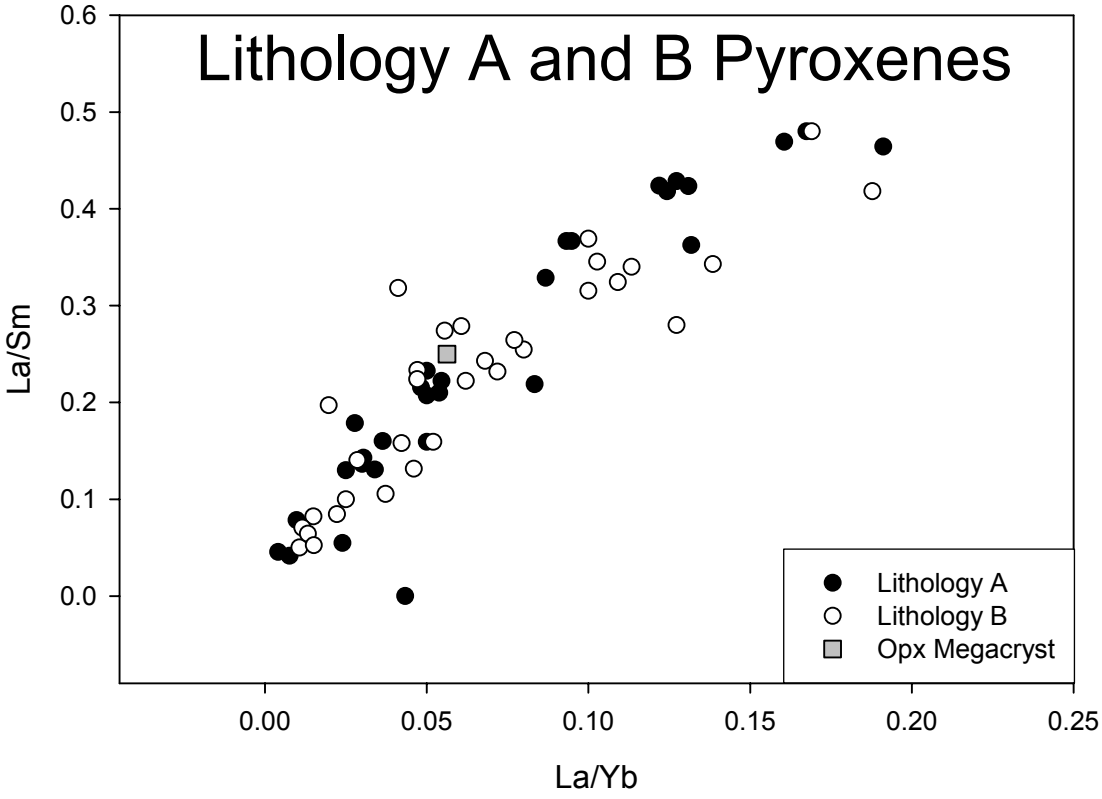

Figure 9. La/Sm vs La/Yb of pyroxenes within lithologies A and B.

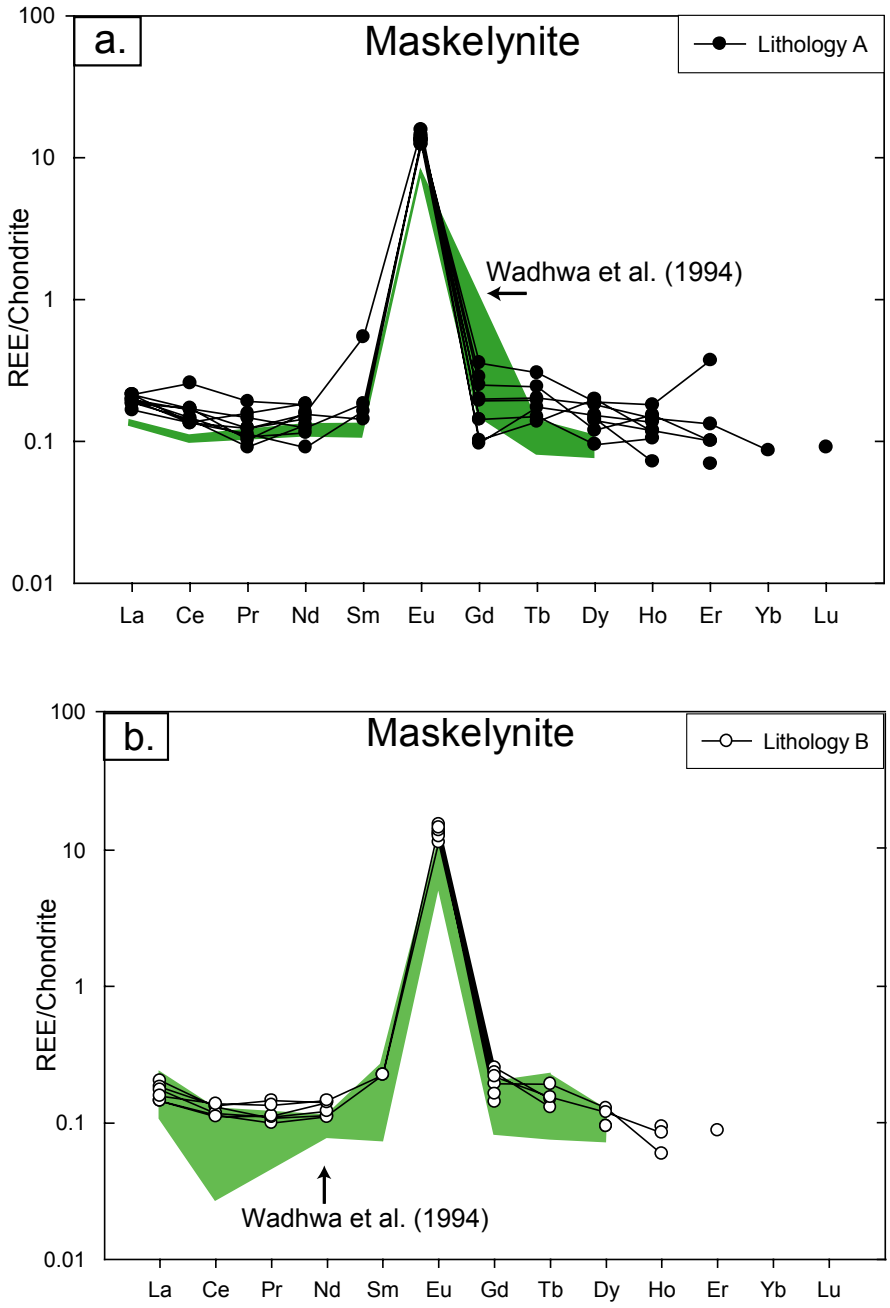

Figure 10. Normalized REE compositions of maskelynite of (a) LithA and (b) LithB. Both plots show prominent (+)Eu anomalies. The shaded region shows the average maskelynite composition (including error) reported by Wadhwa et al. (1999)

Figure 7a shows normalized REEs for megacrystic olivines in LithA. The LREEs are undetectable, and the HREEs increase in concentration from Tb to Lu. The olivines contain a high concentration of Ni (164-493 ppm) and Ga (0.27-0.69 ppm) (Table 4). Nickel concentration generally decreases with decreasing Mg#, whereas zinc concentration generally increases with decreasing Mg#. As expected, whitlockite contains the highest concentrations of REEs (Table 4), followed in decreasing abundances by melt veins, pyroxene, maskelynite, olivine, and opaque phases (chromite, ilmenite, and pyrrhotite), which typically have REE values below the detection limits.

3.4 Parental Melt

The LithA and LithB parental-melt REE compositions that equilibrated with primitive groundmass pyroxenes (Wo_{12}) were calculated twice (Figs. 11a and 11b), using separate sets of distribution coefficients ($D^{pyx\text{-}melt}$). The first parental-melt calculation used distribution coefficients from McKay et al. (1986), shown in Fig. 11a. These coefficients were determined experimentally by analyzing synthetic Shergotty pyroxenes and melts. The values are listed as follows: 0.002 (La), 0.004 (Ce), 0.019 (Nd), 0.031 (Sm), 0.016 (Eu), 0.043 (Gd), 0.09 (Er), 0.13 (Yb), and 0.13 (Lu). McKay et al. (1986) stated that their LREE values (namely La and Ce) exhibit uncertainties of up to 50%. Therefore, the parental-melt composition was also calculated using a different set of distribution coefficients from Lundberg et al. (1990), Fig. 11b. These values are based on mineral-melt experiments from Lundberg (1988) on ALHA77005, a lherzolitic shergottite with pyroxenes that are similar in composition to the EETA79001

Table 4. Sample trace-element analyses of LithA and B using LA-ICP-MS.

	pig		aug		opx	mask		ol	Si-rich glass		whit		chr	il		po	
(ppm)	A	B	A	B	*A	A	B	*A	A	B	A	B	*A	A	B	A	B
Sc	36.5	50.2	90.4	75.2	22.4	1.07	0.76	6.48	24.5	37.0	64.8	–	8.45	71.8	–	<0.58	–
Ti	1226	1507	3363	1968	580	384	286	26.1	3508	6783	13.0	–	3270	287278	–	<2.65	–
V	188	266	343	306	124	4.13	3.34	28.9	127	145	4.98	–	2273	466	–	3.72	–
Cr	2624	3419	3718	3153	2446	2.76	<1.81	1720	2452	1547	14.6	–	274295	2106	–	319	–
Co	44.1	56.6	43.7	43.9	42.6	0.62	0.50	81.2	73.0	37.6	2.31	–	95.5	29.6	–	206	–
Ni	93.8	87.1	116	56.0	112	0.83	0.85	493	391	130	7.25	–	120	52.8	–	6923	–
Zn	–	72.9	65.9	57.9	–	–	–	65.2	77.6	79.1	2.54	–	486	52.6	–	1.59	–
Ga	3.39	3.98	8.24	4.94	1.61	43.5	35.4	0.45	13.0	30.2	10.5	–	43.1	4.59	–	0.13	–
Rb	0.89	0.17	0.03	0.04	0.09	7.96	0.25	<0.04	0.91	2.00	1.09	–	<0.25	<0.19	–	<0.15	–
Sr	1.37	1.18	1.52	0.77	0.30	78.9	64.9	0.02	16.0	36.7	93.5	–	0.14	2.94	–	1.38	–
Y	3.49	4.29	9.23	6.01	1.23	0.11	0.09	0.07	9.10	7.11	727	–	<0.06	0.34	–	<0.05	–
Zr	4.41	4.71	16.30	2.46	1.03	0.10	0.04	0.03	22.6	46.8	82.5	–	3.14	2389	–	<0.16	–
Nb	0.12	0.13	0.09	0.03	0.04	0.00	<0.01	0.02	0.87	1.70	0.13	–	3.37	26.1	–	<0.04	–
Cs	–	0.02	0.02	0.01	–	–	–	<0.01	0.08	0.13	0.38	–	<0.13	<0.11	–	<0.06	–
Ba	0.70	0.59	0.15	0.05	0.13	7.09	4.69	0.03	4.26	10.6	8.81	–	<0.05	<0.06	–	0.53	–
La	0.06	0.07	0.02	0.01	0.01	0.05	0.04	<0.01	0.33	0.20	32.1	–	<0.04	<0.04	–	<0.04	–
Ce	0.17	0.19	0.13	0.06	0.03	0.09	0.08	<0.01	0.87	0.55	84.3	–	<0.03	<0.06	–	<0.03	–
Pr	0.03	0.04	0.04	0.01	0.00	0.01	0.01	0.00	0.18	0.11	14.0	–	<0.03	<0.05	–	<0.02	–
Nd	0.19	0.23	0.29	0.14	0.04	0.05	0.06	<0.02	0.96	0.52	85.2	–	<0.14	<0.21	–	<0.11	–
Sm	0.13	0.21	0.42	0.21	0.04	<0.02	<0.05	<0.02	0.72	0.34	56.5	–	<0.38	<0.29	–	<0.16	–
Eu	0.06	0.06	0.12	0.07	0.01	0.78	0.74	<0.01	0.35	0.41	17.8	–	<0.07	<0.07	–	<0.05	–
Tb	0.07	0.09	0.22	0.14	0.02	0.00	0.00	0.00	0.20	0.16	18.9	–	<0.03	<0.03	–	<0.03	–
Gd	0.36	0.42	0.94	0.57	0.10	0.06	0.03	<0.02	1.33	0.84	115	–	<0.15	<0.18	–	<0.14	–
Dy	0.61	0.68	1.61	1.08	0.20	0.04	<0.02	<0.02	1.44	1.39	138	–	<0.15	<0.11	–	<0.13	–
Ho	0.13	0.15	0.37	0.24	0.05	0.00	<0.01	0.00	0.32	0.29	27.9	–	<0.04	<0.04	–	<0.03	–
Er	0.42	0.51	1.08	0.70	0.15	<0.01	0.04	<0.02	0.94	0.83	74.4	–	<0.17	<0.14	–	<0.05	–
Yb	0.38	0.52	0.96	0.73	0.16	<0.03	<0.04	<0.02	0.95	1.06	55.1	–	<0.23	<0.31	–	<0.17	–
Lu	0.07	0.08	0.16	0.11	0.03	0.00	<0.01	0.01	0.10	0.15	7.75	–	<0.03	<0.05	–	<0.03	–
Hf	0.17	0.20	0.69	0.16	0.04	<0.01	<0.03	<0.01	0.89	1.41	2.77	–	<0.13	65.5	–	<0.10	–
Ta	0.00	0.01	0.00	0.00	0.00	0.00	<0.01	0.00	0.06	0.07	<0.02	–	<0.05	1.63	–	<0.04	–
Pb	0.03	0.03	0.12	0.01	0.01	0.04	0.02	–	–	–	–	–	–	–	–	–	–
Th	–	–	–	–	–	<0.01	<0.01	–	<0.08	0.10	4.21	–	–	<0.10	–	<0.04	–
U	–	–	–	–	–	<0.01	<0.01	–	<0.04	<0.05	0.45	–	–	0.20	–	<0.04	–

* Megacrysts

* Abbreviations are similar to those in Table 1.

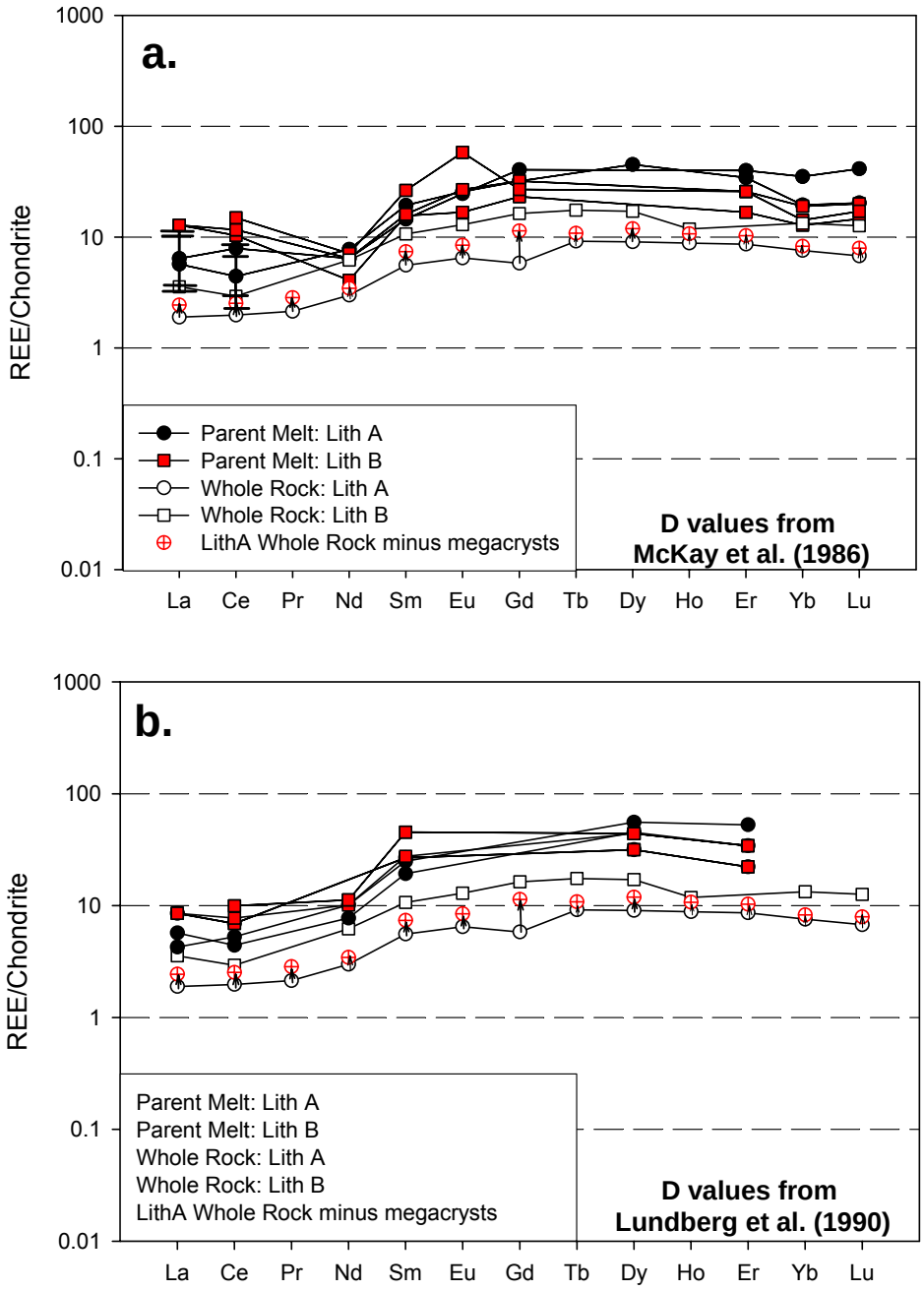

Figure 11. Parental-melt compositions of Wo_{12} groundmass pyroxenes using distribution coefficients from (a) McKay et al. (1986) and (b) Lundberg et al. (1990). LithA whole-rock values are averaged analyses from Burghele et al. (1983), Kong et al. (1999), and Neal et al. (2001). LithB whole-rock values are averaged analyses from Burghele et al. (1983), Laul (1986), and Ma et al. (1982).

pyroxenes (Lundberg et al., 1990). The distribution coefficients were modified by Lundberg et al. (1990) to adjust for Wo content, and are as follows: 0.003 (La), 0.006 (Ce), 0.012 (Nd), 0.018 (Sm), 0.043 (Dy), and 0.068 (Er).

The calculated parental melts for LithA and LithB low-Ca pigeonites (Fig. 11a and 11b) have similar REE patterns, and calculation results lie above their averaged published whole-rock values from Burghele et al. (1983), Kong et al. (1999), and Neal et al. (2001) for LithA, and Ma et al. (1982), Burghele et al. (1983), and Laul (1986) for LithB. The higher REE values in the calculated melts versus the whole-rock values could be due to: (1) inaccurate D values; (2) mixing-effect of megacrysts in LithA; and/or (3) some fractionation of the melt some before pigeonite formation. The whole-rock data of LithA are expected to be lower than the melt that formed groundmass pigeonite, because Mg-rich olivine and orthopyroxene take little REEs and these two minerals are early liquidus phases. Indeed, the differences between calculated-melt and whole-rock compositions are larger for LithA than those for LithB (Fig. 11), which indicate the diluting effects of the olivine and orthopyroxene megacrysts (especially the cores; discussed below). However, the abundances of the megacrysts cannot fully explain the differences in some elements (e.g. La, Eu), which could be the result of uncertainties in D values and fractionation of minerals. The calculated LithB melt has slightly higher REEs than those of LithA, possibly indicating that LithB melt may have undergone a higher degree of crystallization before pigeonite formation.

3.5 Previous estimates on LithA groundmass

There are several existing theories for the petrogenesis of EETA79001 and the contact between lithologies A and B (e.g., McSween and Jarosewich, 1983; Wadhwa et

al. 1994; Mittlefehldt et al. 1999). Most of the early formational theories were developed with the idea that the megacrysts in LithA are out of equilibrium with the groundmass, and therefore must be xenocrysts (Ma et al., 1982; Steele and Smith 1982; McSween and Jarosewich 1983). Perhaps the strongest assertion for the xenocrystic origin of the megacrysts was based on the Fe-rich rims present on olivine and orthopyroxene (Steele and Smith 1982; McSween and Jarosewich 1983). Although Herd et al. (2002) stated that orthopyroxene megacrysts are xenocrysts, they are rimmed by overgrowths that crystallized from a melt similar in composition to the LithA groundmass. However, Goodrich (2002) suggested that most of the megacrysts are phenocrysts.

Much of the controversy about the petrogenesis of LithA and LithB stems from uncertainty in the relationship between the megacrysts and groundmass in LithA; this is a key issue that needs to be further investigated. Here, we review previous calculations of the groundmass compositions and introduce new, hopefully more-precise, compositional estimates. The results of the new groundmass estimates, along with petrographic and chemical data from the present study, are later integrated into various formation hypotheses.

There have been several estimates of groundmass composition of LithA (e.g., McSween and Jarosewich, 1983; Longhi and Pan, 1989, Schwandt et al. 2001; Herd et al., 2002). In the present study, the bulk composition of LithA Groundmass is referred to as "AG". McSween and Jarosewich (1983) calculated the AG by averaging analyses on megacrysts, and then, along with their modes and densities, subtracted the averaged total-megacryst composition from their measured LithA whole-rock composition. This subtraction method resulted in a groundmass composition having Mg# of 58.6, and is

labeled as AG_1 in Table 5. However, because megacrysts are zoned and most of the mass of a grain resides in the outer portion of a crystal (especially near the rims), a direct average of random compositional data could be biased (depending on the number of analyses). A more accurate method for obtaining the chemical abundance of compositionally zoned megacrysts would be to apply a weighting-factor based on volume (i.e., mass) considerations for various EMP analyses; this accounts for analyses further from the cores of concentrically zoned crystals representing larger volumes/masses. In addition, mineral modes by McSween and Jarosewich (1983) were obtained by optical point counting, which is subjective to some extent, and has a lower precision than newer methods that use compositionally-sensitive x-ray digital imaging.

Longhi and Pan (1989) modeled the crystallization sequence for a melt using the LithA composition, AG_1 of McSween and Jarosewich (1983). Their results showed AG_1 to be strongly olivine-normative. Because no olivine was reported to occur in the LithA groundmass, they concluded that McSween and Jarosewich (1983) over-estimated the groundmass MgO content. Longhi and Pan (1989) recalculated AG_1 by subtracting a higher percentage of olivine megacrysts from LithA whole-rock composition, so that no olivine would crystallize in the "groundmass" melt they modeled. Their revised bulk composition resulted in a quartz-normative magma having a Mg# of 53.8 (AG_2, Table 5).

Schwandt et al. (2001) re-analyzed mineral modes and compositions from section 79001, 68, one of the original six sections petrographically described by McSween and Jarosewich (1983). The mineral modes were obtained by using a digital-mapping method based upon processing of x-ray elemental maps obtained by WDS on the EMP. A total of 330,000 points were collected by Schwandt et al. (2001), which provided a

Table 5. Bulk-chemical compositions for EETA79001 LithA groundmass (AG).

	AG_1	AG_2	AG_3	AG_4	AG_5	AG_6	AG_7
SiO2	49.2	50.7	48.4	49.0	50.4	50.2	50.2
TiO2	0.78	0.86	1.98	1.70	0.7	0.8	0.61
Al2O3	6.44	7.10	7.20	7.40	6.5	6.5	5.42
Fe2O3	0.39	0.00	0.00	0.00	0.00	0.00	0.00
Cr2O3	0.12	0.12	0.00	0.15	0.5	0.4	0.37
FeO	18.1	18.7	17.7	18.4	16.8	17.7	19.5
MnO	0.51	0.52	0.55	0.52	0.5	0.5	0.55
MgO	14.4	12.2	12.0	11.5	15.6	14.9	15.7
NiO	0.00	0.00	0.00	0.00	0.00	0.00	0.00
CoO	0.00	0.00	0.00	0.00	0.00	0.00	0.00
CaO	7.96	8.74	9.00	9.20	7.9	8.0	6.64
Na2O	0.97	1.07	0.80	0.90	1.0	1.0	0.92
K2O	0.06	0.07	0.00	0.00	0.00	0.00	0.00
P2O5	0.75	0.00	0.00	1.20	0.00	0.00	0.00
Mg#	58.6	53.8	54.7	52.7	62.4	60.1	59.0

AG_1 McSween and Jarosewich (1983)

AG_2 Longhi and Pan (1989)

AG_3 Schwandt et al. (2001)

AG_4 Herd et al. (2002)

AG_5 This study: LithA Whole Rock (McSween and Jarosewich, 1983) minus weighted average of megacryst cores and rims (includes overgrowths)

AG_6 This study: LithA Whole Rock (McSween and Jarosewich, 1983) minus weighted average of megacryst cores (excludes overgrowths)

AG_7 This study: Weighted average of cores and rims of groundmass crystals plus overgrowths of megacrysts

more precise approximation of modal abundances than the optical point-counting method (1000 points per slide) performed by McSween and Jarosewich (1983). Schwandt et al. (2001) determined modes with significantly lower abundances of pigeonite but higher abundances of augite (Table 1), which resulted in a lower Mg# of 54.7 (AG_3 in Table 5), versus the Mg# of 58.6 from McSween and Jarosewich (1983). To obtain the bulk-composition of the groundmass, Schwandt et al. (2001) used the "average" compositions of mineral, but details are not given on the averaging method used. As discussed above, a direct average of random analyses could be erroneous because crystals are zoned and most of the volume (mass) of a grain is located in the near-rim locales.

Herd et al. (2002) recognized the need to obtain a better estimate of the LithA bulk-groundmass composition, because the megacrysts rims, if formed by overgrowth, should not be considered part of the megacryst chemistry, and should not be subtracted from the LithA whole-rock composition. Based on their experimental data of Cr and V partitioning, Herd et al. (2002) suggested that the pigeonite rims on orthopyroxene megacrysts are simple overgrowths, because they have the same Cr and V abundance (within error) as pigeonite in the groundmass. The Cr and V concentrations of liquid derived from olivine rims are reported to be much lower than the Cr and V concentrations of the groundmass pyroxene. Therefore, they concluded that olivine rims are possibly not overgrowths, but formed before incorporation into the LithA groundmass. Herd et al. (2003) then modified AG_3 (from Schwandt et al., 2001) by adding pigeonite overgrowth rims on orthopyroxene megacrysts to the LithA groundmass, resulting in a lower bulk Mg# of 52.7 (AG_4, Table 5).

When Herd et al. (2002) analyzed the Cr and V concentrations in the calculated liquid-olivine rims and pyroxene groundmass, they compared different liquid Mg#'s of the aforementioned phases (Mg# 34 and Mg# 30 for pyroxene groundmass and olivine rims, respectively). Also, the D values of late-stage melts are kinetically influenced, and may be unreliable to use in modeling and determining disequilibrium effects. Later in this study, we suggest that the olivine rims are overgrowth features.

In summary, previously reported estimates of the bulk-groundmass composition (AG_1 – AG_4, Table 5) have large differences. Part of these discrepancies may be attributed to the methodology of obtaining "average" compositions for the megacryst crystals. Here, we advance a more realistic means of obtaining the compositions of zoned megacrysts. If one assumes a constant spacing of compositional analyses from core to rim, each consecutive analysis away from the core represents a larger volume (mass) of the crystal. Therefore, an analysis at the core represents a significantly smaller volume (mass) than one taken at the rim. Another reason for the AG differences may be the variations in megacryst abundances between studies: 10 vol% olivine from Schwandt et al. (2001) compared to 7 vol% in McSween and Jarosewich (1983). Apparent differences in modes appear to be due to the different analytical methods used. However, the different modes in the LithA groundmass between Schwandt et al. (2001) and McSween and Jarosewich (1983) could be a result of "the chemical criterion rather than McSween's optical one" as quoted from Schwandt et al. (2001). In order to address the bulk composition of LithA groundmass, we conducted extensive modal recombinations of megacrysts taken from the several polished sections studied here.

3.6 NEW LithA Groundmass Reconstructions

In this study, we calculated LithA bulk-groundmass compositions (AG_5, AG_6, AG_7) by modal recombination using three methods (Table 5). To obtain a different methodology for obtaining the groundmass compositions, we used the "weighted average" compositions of the groundmass phases and their modal analyses from our x-ray digital imaging technique. For this, we used a modification of simply averaging EMP compositions, whereby we took into consideration the placement of each EMP analysis within a crystal, with a weighing factor. Although each method used averaged LithA mineral modes (Table 1), the main difference between our study and previous ones is that we used a position-sensitive method for obtaining "a weighted average" for the zoned crystals.

The first method for determining the bulk-composition of the groundmass (AG_5, Table 5) is by subtracting the weighted-average compositions of megacrysts from the LithA whole-rock composition reported by McSween and Jarosewich (1983). Megacrysts commonly have a diameter of approximately 1 mm and rims that are 150 μm thick based upon CaO profiles (Fig. 3a-c). Using an approximate-spherical shape approximation, cores and rims comprise approximately 35 vol% and 65 vol%, respectively, of the crystal. Therefore, the compositions of megacrysts were averaged by weighting the compositional analyses of the cores and rims according to the volumes they represented. This method results in the highest Mg# reported (Mg# 62.4), but there was no consideration here for the possibility of the megacryst overgrowth being secondary (e.g., after incorporation into a melt of a different composition).

The second method of calculating bulk-groundmass LithA assumes the rims of olivine, orthopyroxene, and chromite are overgrowths. Herd et al. (2002) and Goodrich (2003) indicated that orthopyroxene and chromite megacrysts have overgrowths of pigeonite and ulvöspinel, respectively. Here, we suggest that Fe-rich rims of olivine megacrysts are also overgrowth features. The olivine megacrysts show sudden CaO enrichment at Mg# 69, at an average of ~150 μm from the rim (Fig. 3d). This suggests that those rims are overgrowths and may represent the onset of olivine (and orthopyroxene) crystallization from a secondary magma in contact with the megacrysts. Therefore, to obtain the LithA groundmass-melt composition, instead of subtracting the entire megacryst from the whole-rock total, only the compositions of the megacryst cores (including chromite cores) were subtracted from the LithA whole-rock from McSween and Jarosewich (1983), (AG_6, Table 5). The resulting Mg# of 60.1 for AG_6 is significantly lower than AG_5. Importantly, this assumes that the rims on the megacrysts are direct crystallization from the groundmass melt.

3.7 LithA Groundmass Composition Direct

The third method calculates the bulk-groundmass composition directly using the weighted-averages of minerals in the groundmass and includes overgrowths on the olivine, orthopyroxene, and chromite megacrysts (AG_7, Table 5). The groundmass crystals are zoned, and the cores and rims share similar volume percentages as the megacryst cores and rims. Therefore, the composition of the groundmass minerals (that display zonations) are given a weight of 65% for the rims and 35% for the cores. We consider this AG calculation as the most reasonable and precise of all reported compositions. Unlike some of the previous calculations (AG_1-AG_4), its derivation is

based upon groundmass mineral abundances (from multiple sections) that were obtained from the x-ray digital-imaging technique with the EDS on the EMP (~250,000 points/section). These data were used with the weighted compositional averages of the minerals (and their densities), and are independent of any LithA whole-rock compositional values. Interestingly, the resultant Mg# of 59.0 is similar to the value of Mg# 58.6 reported by McSween and Jarosewich (1983). The results of this method (AG_7) can be interpreted to indicate that McSween and Jarosewich (1983) may have fortuitously subtracted a representative amount of olivine and orthopyroxene megacrysts from the whole-rock composition when calculating AG_1. Therefore, the modification of AG_1 to form AG_2 by Longhi and Pan (1989) may be inappropriate. Also, slight changes in AG_7 overgrowth abundances result in only minor changes in the calculated AG_7 composition.

4. DISCUSSION

In the following discussion, we investigate the various formation models and possible relationships between the two lithologies using our petrographic observations, major- and trace-element chemistry data, and the newly derived LithA groundmass composition (AG_7). The formation models that we will address include fractional crystallization, assimilation, and magma-mixing scenarios. Other theories such as an impact origin or partial melting have been discounted by Warren (1997) and McSween and Jarosewich (1983), respectively, and will not be addressed further.

4.1.1 Fractional Crystallization

The fractional crystallization model was examined by McSween and Jarosewich (1983) but was dismissed because of the megacrysts were identified as being out of equilibrium with the groundmass. However, Goodrich (2003) suggested that most megacrysts may actually be phenocrysts, based on textures, olivine CSD data, orthopyroxene trends in Al_2O_3 versus Cr_2O_3 plots, and chromite textures. The olivine and orthopyroxene megacrysts from the analyzed sections have continuous Fe-Mg zonations from core to rim that suggest they formed under fractional crystallization conditions. Further support can be found in the trace-element chemistry of pyroxenes; the REE trends show progressive enrichment with increased Mg#.

The LithA crystallization history was modeled using the MELTS software package (Ghiorso and Sack, 1995). This software was chosen over similar computer modeling software because it has been reportedly shown by Thompson et al. (2003) to successively model a Martian meteorite better than MAGPOX or COMAGMAT. A

starting pressure of 0.01 GPa and oxygen fugacity of QFM -2 (Herd et al. 2001) were used. The results show that MELTS does not reproduce the observed mineral compositions (e.g., pyroxenes) and mineral abundances (e.g., excess of orthopyroxene). This appears to be an insurmountable obstacle to overcome for the fractional crystallization formation model.

4.1.2 Assimilation-Fractional Crystallization (AFC)

McSween and Jarosewich (1983) explored the possibility of an assimilation scenario. Their mixing calculation suggested that LithA can be formed by adding ~36% harzburgite to a LithB-type magma. Thermal calculations by Wadhwa et al. (1994) showed that the heat needed to assimilate this amount of ultramafic material is greater than the heat that can be provided by the latent heat of crystallization. However, mixing models by Mittlefehldt et al. (1999) suggested that there may be just enough heat generated by the latent heat of crystallization to drive assimilation. The concurrent fractionation of a melt and assimilation of a rock (where the energy is provided by the latent heat of crystallization) is called assimilation-fractional crystallization (AFC). Here, we model an AFC process by following the method of DePaulo (1981), using whole rock trace-elements; the results are shown in Figure 12.

As assumed by previous studies (e.g. McSween and Jarosewich 1983; Wadhwa et al. 1994), LithB is taken to be the melt, and lherzolitic shergottite ALHA77005 is the composition of the rock being assimilated. These two end-members are appropriate because LithA megacrysts show close similarities in both major- and trace-element chemistry to minerals in ALHA77005 (Steele and Smith, 1982; McSween and Jarosewich, 1983; Wadhwa et al., 1994). In our AFC modeling, we have assumed an "r"

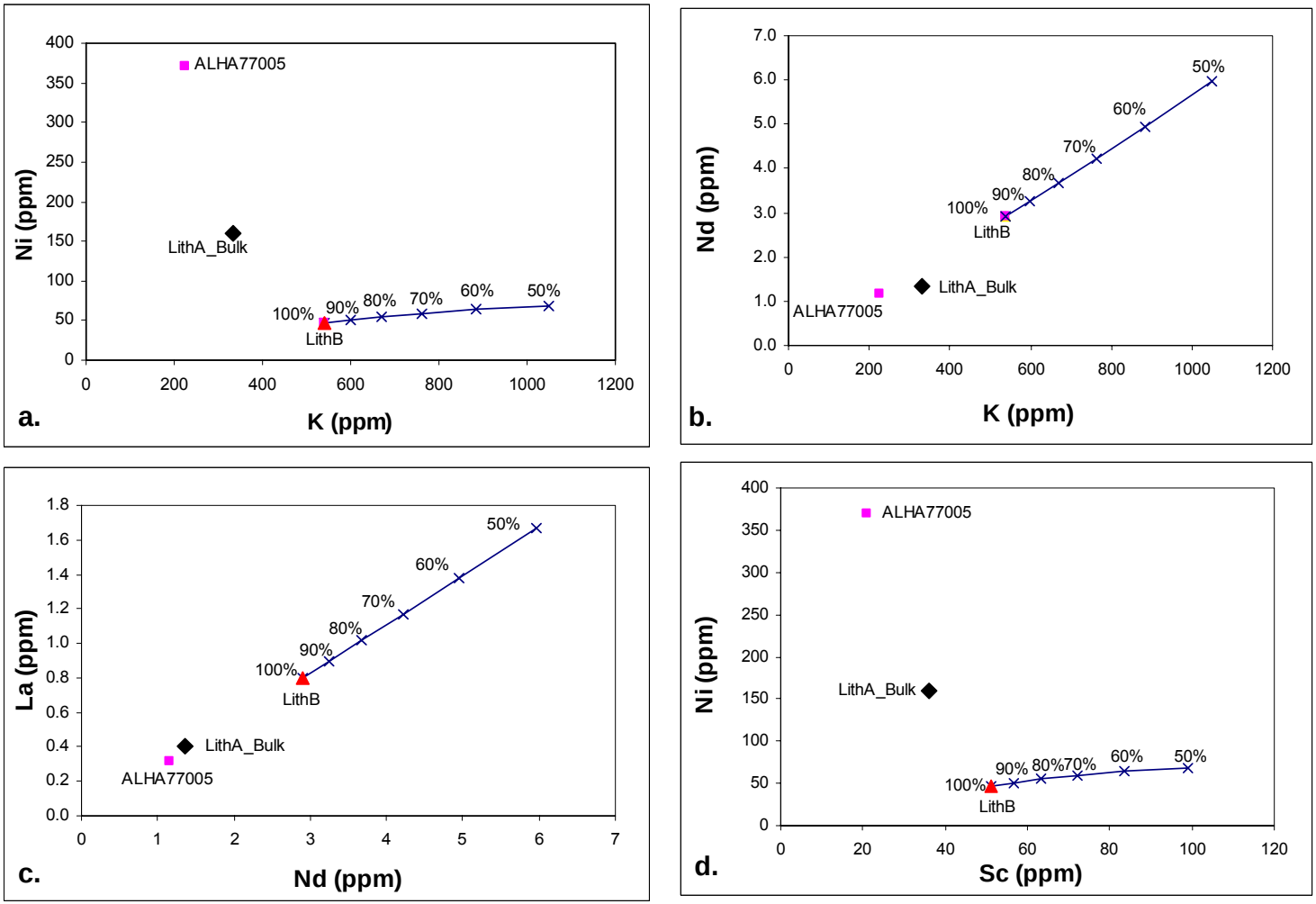

Figure 12. Modeled AFC crystallization pathway (solid line) of trace elements at various melt fractions between LithB (melt) and ALHA77005 (assimilated rock). Trace-element concentrations of the assimilating liquid start at LithB and move away from ALHA77005.

value (mass assimilated/melt) of 0.2 (or 20% assimilation), because it has been shown to be a conservative estimate of similar basalt-high-Mg basalt interactions in lunar systems (Neal and Taylor, 1989). Figure 12 shows the change in minor- and trace-element concentrations with decreasing liquid-mass fraction (solid line) of several trace elements. At the onset of AFC, the initial concentration of elements in the liquid is bulk LithB. With progressive assimilation-fractional crystallization, the trace-element concentration in the liquid becomes enriched and moves away from the ALHA77005 and LithB end-members, as well as away from both whole-rock LithA and LithA groundmass compositions. The same results are obtained when r values are varied from 0.1 to 1.0. The fact that LithA lies on the wrong side of the predicted trend by AFC suggests that at least one of the end- members is incorrectly assumed.

4.1.3 Magma Mixing

The magma-mixing model suggests that LithA formed by mixing a LithB type magma with a lherzolitic and phenocryst-bearing magma similar in composition to ALHA77005 (McSween and Jarosewich, 1983; Wadhwa et al., 1994). Wadhwa et al., (1994) favored a magma-mixing process over assimilation because of the temperature constraints associated with the latter. Mixing models by Mittlefehldt et al. (1999) suggested that an incompatible-element-poor lherzolite is needed to generate LithA, and the suitable end-member would be a cumulate lherzolite with minor-trapped melt. They suggested that it was unlikely that magma with the composition of a trace element-poor lherzolite would occur on Mars. It would require that the melts formed by high degrees of melting (to dilute incompatible trace elements) of an ultramafic-cumulate-source region (Mittlefehldt et al., 1999).

Magma mixing is likely if both magmas had similar compositions and existed at similar temperatures before they mixed. It is assumed that a high degree of mixing of two magmas would be required to form LithA. The mixing of basaltic magma with lherzolitic magma may result in incomplete mixing because of possible differences in density, viscosity, and melt temperatures between the two magmas. Therefore, the following mixing scenarios include other possible types of end-members:

The first mixing scenario suggests that LithA melt mixed with cumulate olivine/orthopyroxene crystals that are homogeneous in composition from core to rim (Fo_{80}, Fo_{73}). The olivine and orthopyroxene then re-equilibrated with the crystallizing groundmass, so that the Fe-rich rims were formed. This theory is unlikely because the kinetics of Fe-Mg exchange in olivine is much faster than orthopyroxene; the olivine should be homogenized for the duration that formed the rim of pyroxenes. This mixing scenario is also unlikely because the olivine megacrysts are large (~800 μm in diameter), and the groundmass is fine-grained; this suggests the cooling conditions may have been faster than that needed for reequilibration of the megacrysts.

The second mixing scenario for the formation of LithA involves a LithB magma that mixed with olivine cumulate crystals (Fo 81 cores). This theory would require LithB to mix (or back-react) with a significant amount of megacrysts to increase its whole rock composition from Mg# 42.6 to that of LithA (Mg# 61). This mixing scenario is possible, especially because the REE concentration of LithA whole rock lies under the LithA parental melt (Fig. 11a-b).

The third mixing scenario suggests that a magma (M_1), having the composition of AG_7, begins to crystallize olivine crystals (Fo81-70) that are removed from the melt. This

M_1 magma (megacryst free) then mixes with megacryst cumulate crystals form a separate magma (M_2) forming overgrowths that begin at ~Fo 69 for olivine. This scenario may be unlikely because it requires M_1 magma to be in equilibrium with the cumulate crystals it incorporates. Also, the olivine cumulate crystals (from M_2) are likely to have been entrained in a late-stage Fe-rich magma. Mixing M_1 of AG_7 composition with this late-stage magma may significantly lower the Mg# of the melt to values lower than Mg# 59, and would not match the LithA whole rock composition of Mg# 61.

4.1.4 Formation of Lithology A

The groundmass composition of LithA presents a unique problem when the crystallization sequence is modeled by the MELTS software program. The MELTS results for the AG_7 composition indicates that approximately 6 vol% olivine crystallizes, starting at approximately Fo 83.9. No olivine is observed in the groundmass; therefore, olivine must be present as overgrowths on the olivine megacrysts. If the crystallization sequence of AG_5 is modeled by MELTS (the groundmass composition only, no megacryst overgrowths), olivine still crystallizes in the groundmass.

The bulk-chemical composition of each lithology and the composition of the megacryst cores (including the start of the inferred overgrowths) are given in Table 6. Based on these values, we suggest the following model (Fig. 13).

1. The megacrysts form as phenocrysts from a peridotitic magma.
2. The megacrysts are incorporated by an evolved magma, having a liquid Mg# of 40. This magma is the LithA groundmass parent (AGP). It is imagined that the megacrysts are part of the peridotite wallrock through which the AGP magma intrudes.

Table 6. Megacryst compositions, and LithA and LithB whole-rock chemistry.

LithA Megacrysts	Olivine	Mg# Liquid (Kd=0.3)	Orthopyroxene	Mg# Liquid (Kd=0.27)
Core	Fo 81	Mg# 57	Mg# 75	Mg# 45
Start of overgrowths	Fo 69	Mg# 40	Mg# 71	Mg# 40
End of overgrowth	Fo 50	Mg# 23	Mg# 45	Mg# 18
Type of overgrowth	Olivine		Pigeonite	

LithA Whole Rock*	Mg# 61.0
LithB Whole Rock*	Mg# 42.6
AG7	Mg# 59.0

*McSween and Jarosewich (1983)

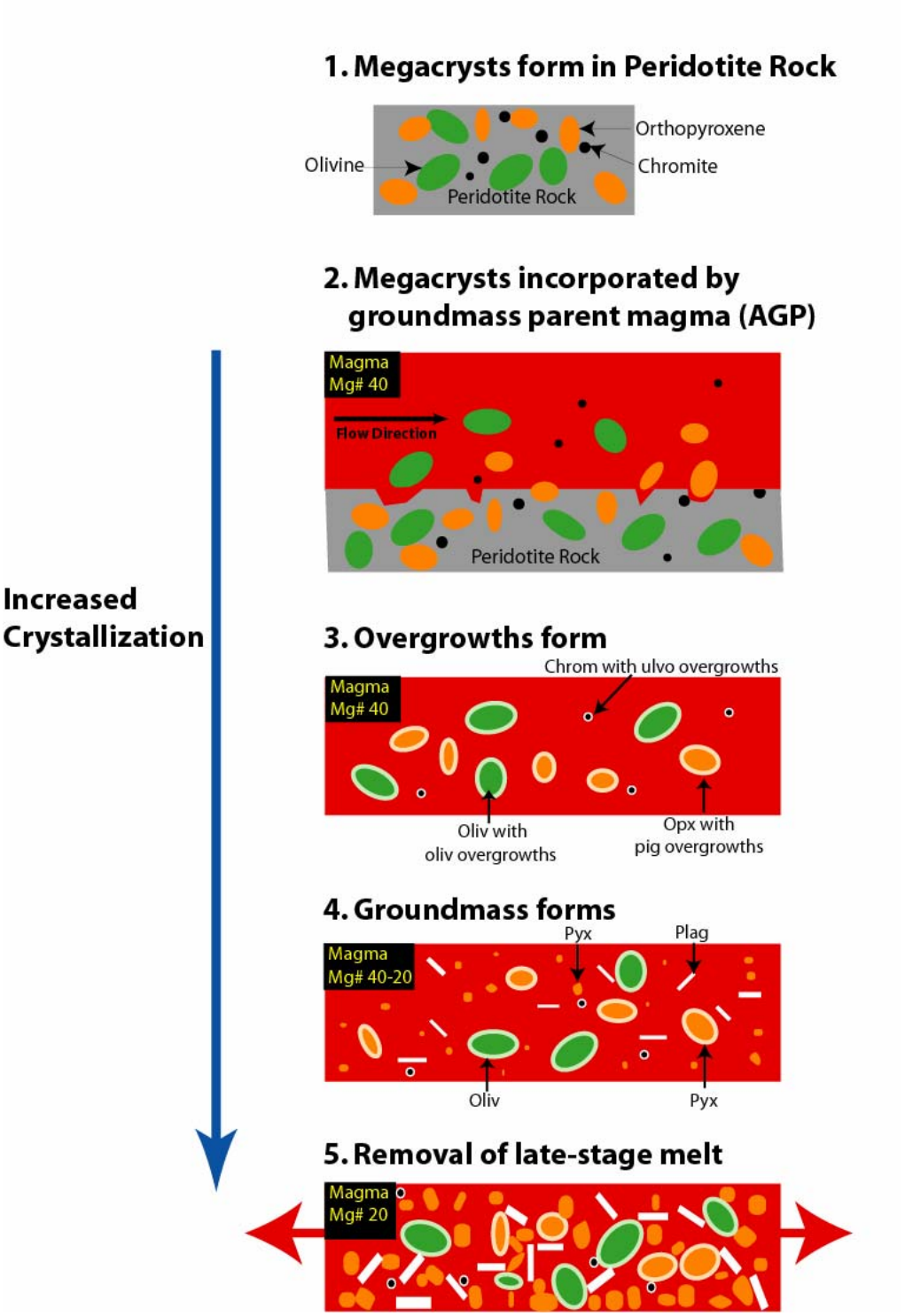

Figure 13. Suggested model for the formation of LithA. Megacrysts mix with magma having a composition of Mg# 40. Overgrowths and groundmass form, and late-stage melt is removed.

3. Overgrowths form on the megacrysts.
4. Groundmass crystals form until the liquid reaches ~Mg# 20.
5. Removal of late-stage liquid. This process is required to raise the AGP composition (Mg# 40) to the observed AG_7 composition (Mg# 59).

There will undoubtedly be some interaction (e.g. resorption, diffusion, etc…) between the megacrysts and the melt, which will disrupt the heat balance of the magma and alter the crystallization of minerals. This may explain why LithB pyroxenes crystallize toward the Fe-rich compositions, whereas LithA pyroxenes do not (Fig. 2a-b). This may also explain why the LithA groundmass is finer-grained than LithB (i.e. faster crystallization). A disruption in the heat balance of the magma requires the megacrysts to exist at cool temperature before incorporation. One scenario in which this might happen is if the AGP magma intruded a peridotite rock, and removed megacrysts of olivine, orthopyroxene, and chromite off of the wall rock (Fig. 13).

One benefit of this model is that it is able to explain the overgrowth features on the olivine and orthopyroxene megacrysts. Also, it avoids the heat constraints associated with the magma mixing and assimilation theories. This model requires the removal of the remaining late-stage melt, because the liquid that initially forms the overgrowths on the megacrysts (Mg# 40) does not match the observed groundmass composition derived by modal recombination (Mg# 59). Therefore, there must have been some late-stage melt removal after the overgrowths formed (liquid Mg# 20). One shortcoming of this model is that only ~10 wt% liquid remains at Mg# 20. Removing ~10 wt% liquid may not be enough to fully raise the groundmass composition. Also, the removal of late-stage melt would require a process such as filter processing, possibly an unrealistic process.

4.1.5 Radiogenic Isotope Relationships between LithA and LithB

Radiogenic isotope work by Wooden et al. (1982) suggested that LithA and LithB contain different initial Sr isotope values. They concluded that LithA and LithB cannot be related by co-magmatic processes, and must have come from two different sources. Nyquist (1984) stated that the initial Rb-Sr data for handpicked megacrysts lies below the LithA isochron, and suggested an assimilation theory (that includes LithB) for the formation of LithA. However, Wadhwa et al. (1994) described a conversation with Nyquist where he stated that there were problems with the Sr blanks when analyzing the megacrysts; the megacrysts now lie on the LithA isochron. This suggests that the megacrysts may be related to the LithA groundmass. No further work has been done on this subject, and the issue remains unresolved (L. Nyquist, pers. commun.).

5. SUMMARY

- Mineral trace-element compositions show that LithA and B share similar REE patterns and concentrations; therefore, a relationship between the two lithologies is inferred.
- An entirely new LithA bulk-groundmass composition was derived (AG_7, Mg# 59.0), using weighted compositional analyses of the phases and mineral modes from x-ray digital-imaging modal-analysis techniques.
- The newly derived LithA groundmass composition confirms that McSween and Jarosewich (1983) subtracted, perhaps fortuitously, the correct amount of olivine from their whole-rock composition. Alternative derivations, e.g. Longhi and Pan (1989), appear inaccurate.
- Modeling of the crystallization sequence of AG7, and CaO profiles across olivine megacrysts, suggest the olivine rims are overgrowths.
- All formational theories have their pros and cons (some more than others). Our data suggest fractional crystallization is improbable.
- The AFC formational theory cannot be modeled using the suggested endmembers from the literature (LithB and ALHA77005). Either one (or both) of the endmembers is not correct, or AFC is not a viable explanation.
- The magma mixing model may be feasible if different end-members are chosen.
- Our preferred petrogenetic model for LithA details the origin of the xenocrystic assemblage, the overgrowths on these xenocrysts, and requires the observed

primitive groundmass composition to be misrepresentative due to late-stage melt removal of the late-stage melt.

- The proposed model, involving late-stage melt removal, would explain the overgrowth formations; however, there may not have been enough late-stage melt removed in order to raise the composition of the groundmass parent melt (Mg# 40) to the observed groundmass composition (Mg# 59).

REFERENCES

Anders E. and Grevesse N. (1989) Abundances of the elements: Meteoritic and solar. *Geochimica et Cosmochimica Acta* 53:197-214.

Bocter N.Z., Fei Y., Bertka C.M., Alexander C.M.O.'D., and Hauri E. (1998) Vitrification and high pressure phase transition in olivine megacrysts from lithology A in martian meteorite EETA79001. *Lunar Planet. Sci. XXXIX*. Abstract #1492.

Bogard D.D. and Johnson P. (1983) Martian gases in an Antarctic meteorite? *Science*. 221, 651-654.

Burghele A., Dreibus G., Palme H., Rammensee W., Spettel B., Weckwerth G. and Wänke H. (1983) Chemistry of shergottites and the shergottite parent body (SPB): Further evidence for the two component model for planet formation. (abs) *Lunar Planet. Sci. XIV*, 80-81.

DePaolo D. (1981) Trace element and isotopic effects of combined wallrock assimilation and fractional crystallization. *Earth and Planetary Science Letters*, 53, 189-202.

Ghiorso, M.S., and Sack, R.O. (1995) Chemical mass transfer in magmatic processes. IV. A revised and internally consistent thermodynamic model for the interpolation and extrapolation of liquid-solid equilibria in magmatic systems at elevated temperatures and pressures. *Contributions to Mineralogy and Petrology*, 119, 197-212

Goodwich C.A. (2003) Petrogenesis of olivine-phyric shergottites Sayh al Uhaymir 005 and Elephant Moraine A79001 lithology A. *Geochimica et Cosmochimica Acta*, 67, No. 19, 3735–3771.

Herd C.D.K., Schwandt C.S., Jones J.H. and Papike J. (2002) An experimental and petrographic investigation of Elephant Moraine 79001 lithology A: Implications for its petrogenesis and the partitioning of chromium and vanadium in a martian basalt. *Meteoritics & Planetary Science*, 37, 987-1000.

Herd C.D.K., Papike J.J., Brearley A.J. (2001) Oxygen fugacity of martian basalts from electron microprobe oxygen and TEM-EELS analyses of Fe-Ti oxides. American Mineralogist, 86, 1015-1024.

Jones, J. H. (1995) Experimental trace element partitioning, rock physics and phase relationships, a handbook of physical constants, *American Geophysical Union*, 74-104.

Kaiden H., Mikouchi T., Miyamoto M. (1998) Cooling rates of olivine xenocrysts in EETA79001 shergottite. Antarct. Meteorite Res., 11, 92-102.

Kong P., Ebihara M. and Palme H. (1999) Siderophile elements in Martian meteorites and implications for core formation in Mars. *Geochim. Cosmochim. Acta* 63, 1865-1875.

Laul J. C. (1986) The Shergotty consortium and SNC meteorites: An overview. *Geochim. Cosmochim. Acta* 50, 875-888.

Longerich, H.P., Jackson S.E., and Gunther D. (1996) Laser ablation inductively coupled plasma mass spectrometric transient signal data acquisition and analyte concentration calculation. *Journal of Analytical Atomic Spectrometry*. 11, 899-904.

Longhi J., and Pan V. (1989) The parent magmas of the SNC meteorites. *Lunar Planet. Sci. XIX*, 451-464.

Lundberg L.L., Crozaz G., and McSween H.Y., Jr. (1990) Rare earth elements in minerals of the ALHA77005 shergottite and implications for its parent magma and crystallization history. *Geochimica et Cosmochimica Acta,* 54, 2535-2547.

Lundberg L.L., Crozaz G., McKay G., Zinner E. (1988) Rare earth element carriers in the Shergotty meteorite and implications for its chronology. *Geochimica et Cosmochimica Acta,* 52, 2147-2163.

Ma M.-S., Laul J.C., Smith M.R. and Schmitt R.A. (1982) Chemistry of shergottites Elephant Moraine A79001 and Zagami. (abs) *Lunar Planet. Sci. XIII*, 451-452.

McKay G., Wagstaff J., and Yang S. R. (1986) Clinopyroxene REE distribution coefficients for Shergottites - the REE content of the Shergotty melt. *Geochimica Et Cosmochimica Acta* 50(6), 927-937.

McSween H.Y. Jr. and Jarosewich E. (1983) Petrogenesis of the Elephant Moraine A79001 meteorite: multiple magma pulses on the shergottite parent body. *Geochim. Cosmochim. Acta* 47, 1501–1513.

McSween H.Y. Jr. (1982) An example of igneous layering on a meteorite parent body. *Lunar Planet. Inst.*, 106-107.

Mikouchi T., Miyamoto M., McKay G. (1999) The role of undercooling in producing igneous zoning trends in pyroxenes and maskelynites among basaltic Martian meteorites. *Earth and Planetary Science Letters*, 173, 235-256.

Mittlefehldt D.W., Lindstrom D.J., Lindstrom M.M., Martinez R.R. (1999) An impact-melt origin for lithology A of martian meteorite Elephant Moraine A79001. Meteoritics and Planetary Science, 34, 357-367.

Neal C.R., Ely J.C. and Jain J.C. (2001) New platinum-group element (PGE) data for Martian meteorites: The influence of igneous processing. (abs) *Lunar Planet. Sci. XXXII*, #1682. Lunar Planetary Institute, Houston. (CD-ROM)

Neal C.R. and Taylor L.A. (1989) High alumina (HA) and very high potassium (VHK) basalt clasts from Apollo 14 breccias, part 2 – Whole rock geochemistry: further evidence for combined assimilation and fractional crystallization within the lunar crust. *Lunar Planet. Sci. XIX,* 147-161.

Norman M.D., Pearson N.J., Sharma A., and Griffin W.L. (1996) Quantitative analysis of trace elements in geologic materials by laser ablation ICPMS: instrumental operating conditions and calibration values of NIST glasses. *Geostandards Newsletter*, vol 20, No. 2, 247-261.

Nyquist L., Weismann H., Shih C.-Y., and Bansal B. (1986) Sr isotopic systematics of EETA 79001 glass. *Lunar Planet. Sci. XVII,* 624-625.

Nyquist L., Wooden J., Bansal B., Wiesmann H., and Shih C.-Y. (1984) Sr and Nd isotopic systematics of EETA 79001. *Meteoritics,* 19, Pg. 284.

Schwandt C.S., Jones J.H., Mittlefehldt D.W., and Treiman A.H. (2001) The magma composition of EET79001A: The first recount. *Lunar Planet. Sci. XXXII*. Abstract 1913.

Steele and Smith (1982) Petrography and mineralogy of two basalts and olivine-pyroxene-spinel fragments in achondrite EETA79001. *Lunar Planet. Sci. XIII*, A375-A384.

Taylor L.A., Patchen A., Taylor D.H.S., Chambers J. G., and McKay D. S. (1996). X-ray digital imaging petrography of lunar mare soils: Modal analyses of minerals and glasses. *Icarus* 124:500-512

Thompson C.K, Slater V.P., Stockstill K.R., Anand M., Nettles J., Milam K., Cahill J., and Taylor L.A. (2003) An evolution of the igneous crystallization programs – MELTS, MAGPOX, and COMAGMAT part I: Does one size fit all? *Lunar Planet. Sci. XXXIV*. Abstract 1881.

Treiman A.H., Gleason J.D., and Bogard D.D. (2000) The SNC meteorites are from Mars. *Planet Space Sci.* 48, 1213–1230.

Usui T., McSween H.Y., and Floss C. (2007) Petrogenesis of olivine-phyric shergottite Yamato 980459, revisited. Geochimica et Cosmochimica Acta, (submitted).

Wadhwa M., McSween H.J., and Crozaz G. (1994) Petrogenesis of shergottite meteorites inferred from minor and trace element microdistributions. *Geochimica et Cosmochimica Acta*. Vol. 58, Issue 19, 4213-4229.

Warren P.H. and Kallemeyn G.W. (1997) Origin of the "A" lithology in presumed Martian meteorite Elephant Moraine 79001: Assimilation mixing more likely than impact melting. *Meteoritics and Planetary Science*, Vol. 32, No. 4, Supplement. A135-A136.

Wooden J., Shih C.-Y., Nyquist L., Bansal B., Wiesmann H., and McKay G. (1982) Rb-Sr and Sm-Nd isotopic constraints on the origin of EETA79001: A second Antarctic shergottite. *Proc. Lunar Planet. Sci. XIII*, 879–880 (abstract).

APPENDIX

Optical Photomosaics and Back Scattered-Electron Images

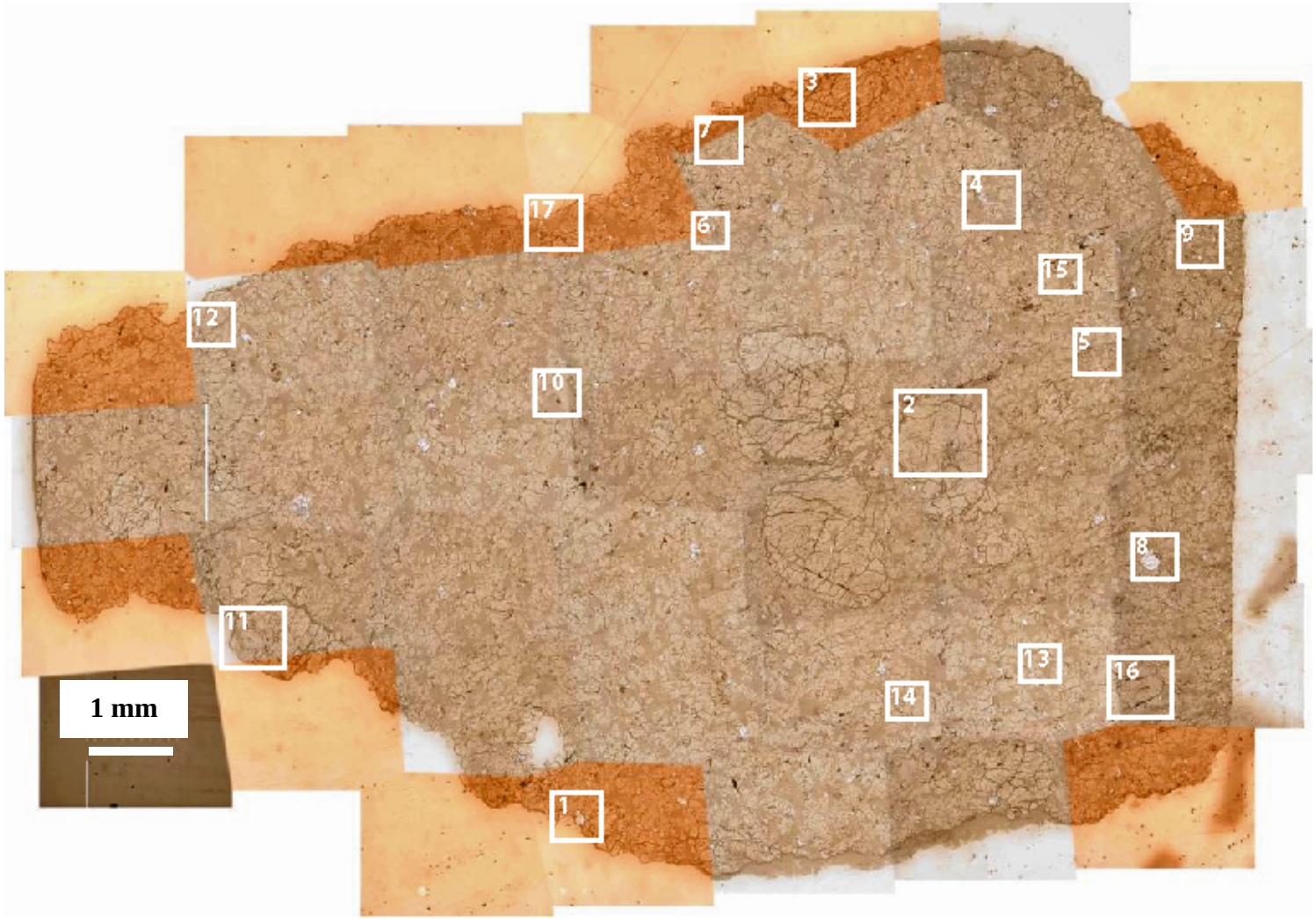

79001.616 (LithA)

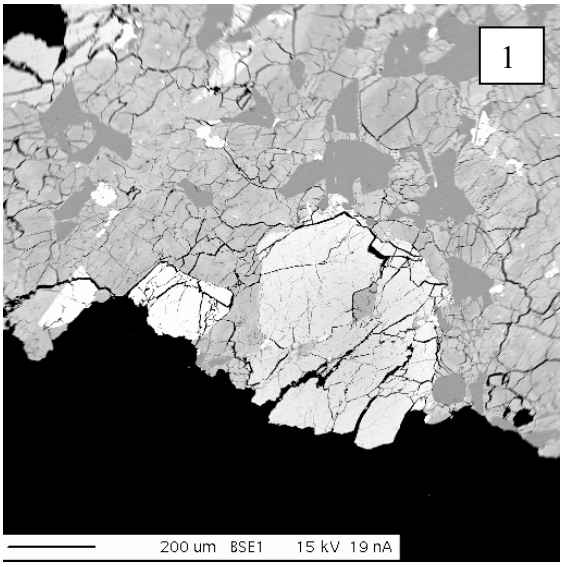
1
200 um BSE1 15 kV 19 nA

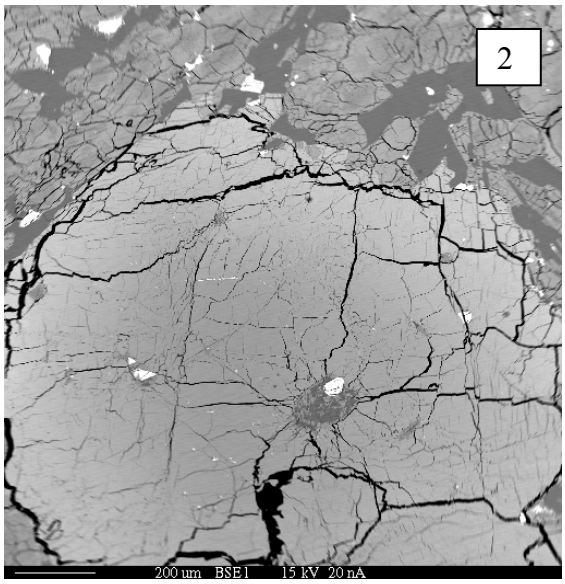
2
200 um BSE1 15 kV 20 nA

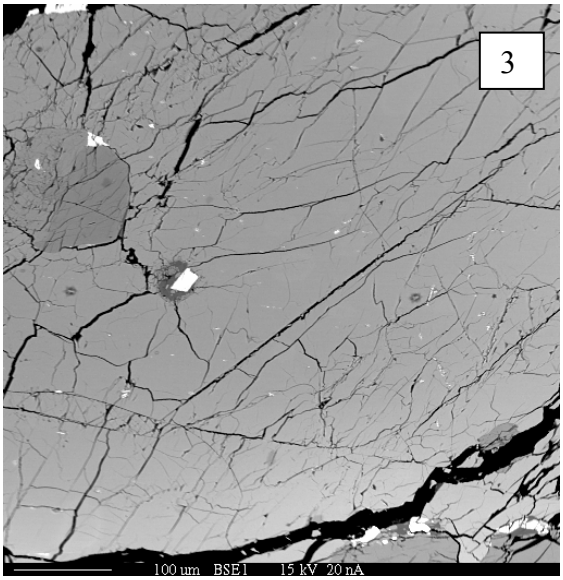
3
100 um BSE1 15 kV 20 nA

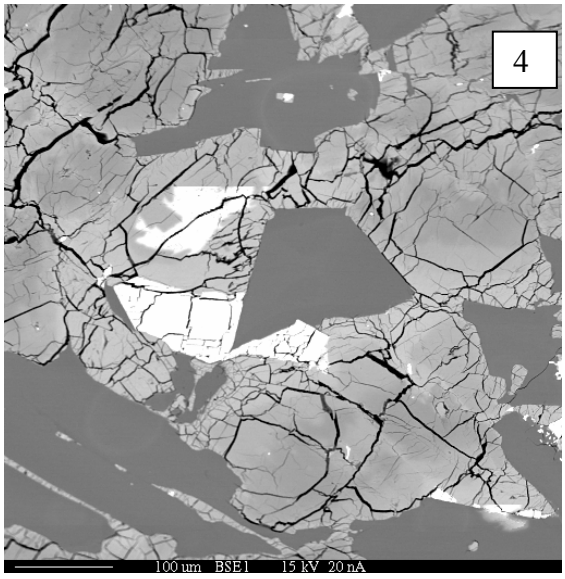
4
100 um BSE1 15 kV 20 nA

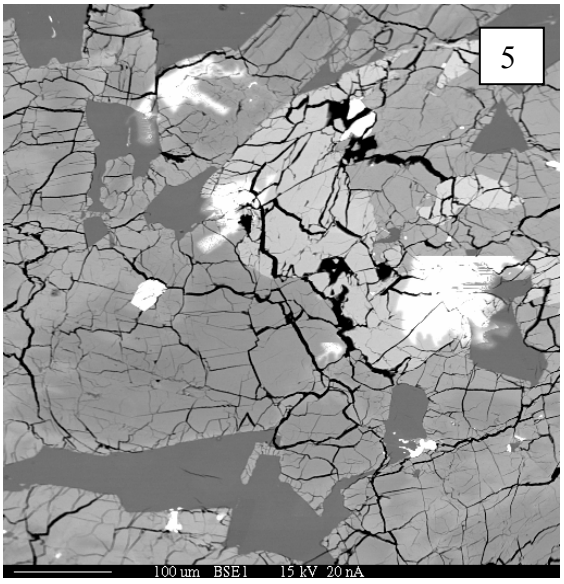
5
100 um BSE1 15 kV 20 nA

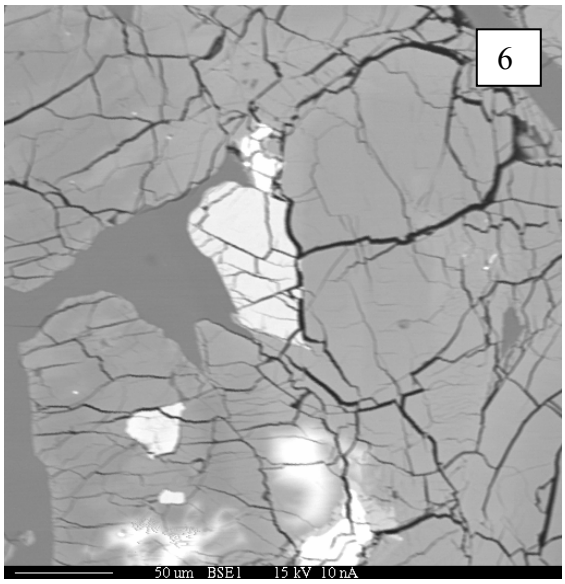
6
50 um BSE1 15 kV 10 nA

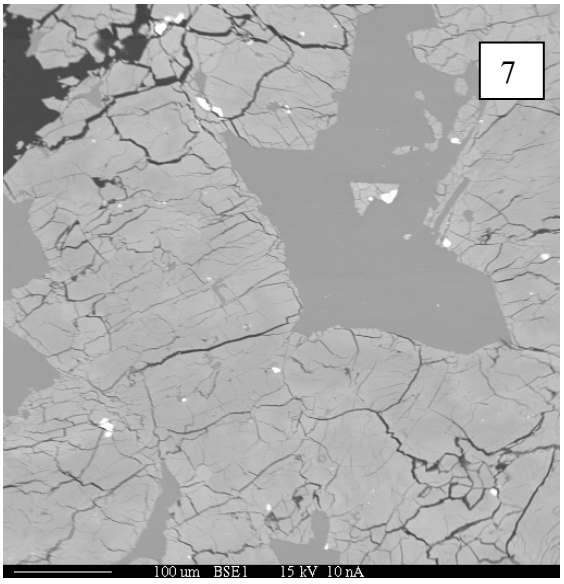
7
100 um BSE1 15 kV 10 nA

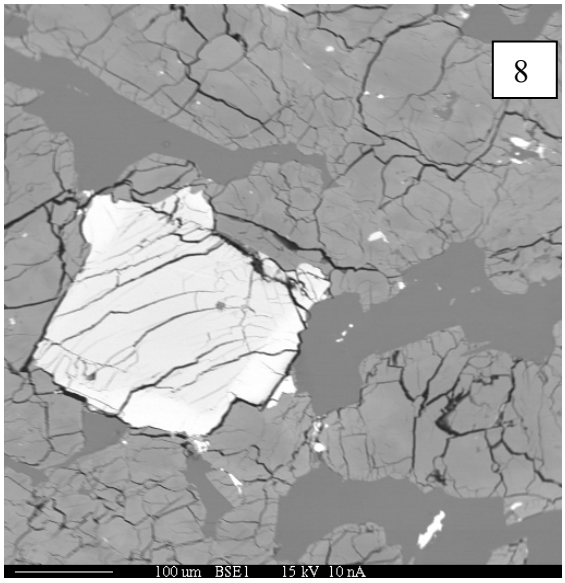
8
100 um BSE1 15 kV 10 nA

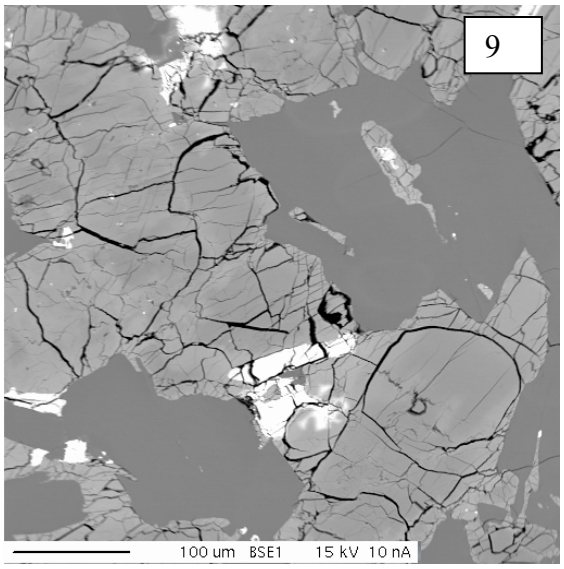
9
100 um BSE1 15 kV 10 nA

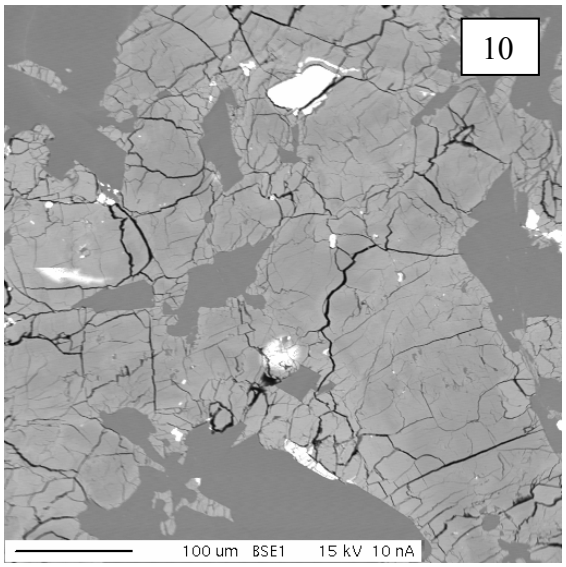
10
100 um BSE1 15 kV 10 nA

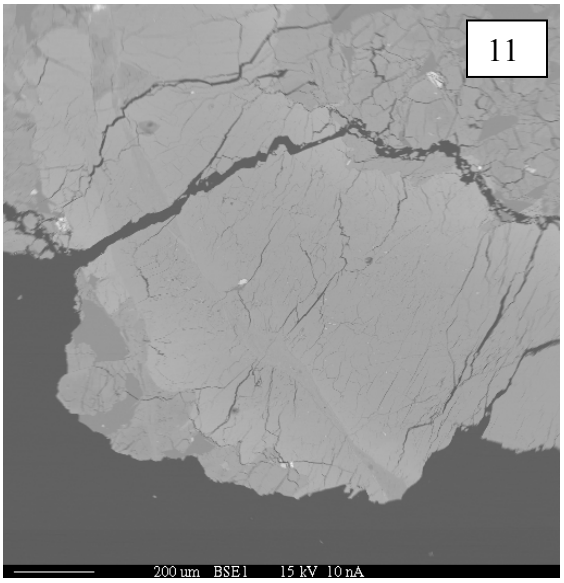
11
200 um BSE1 15 kV 10 nA

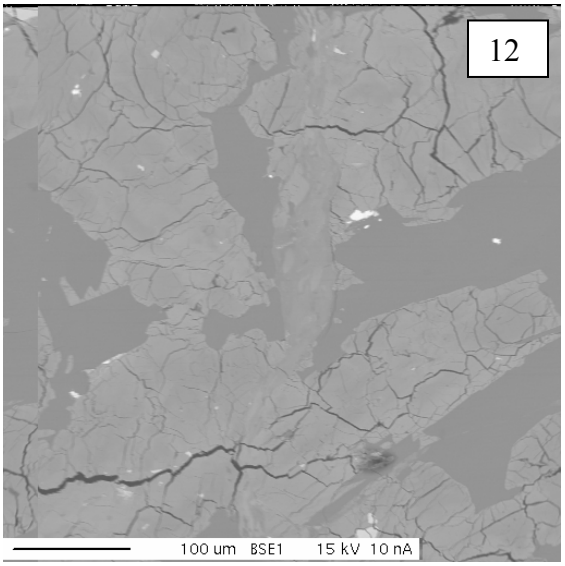
12
100 um BSE1 15 kV 10 nA

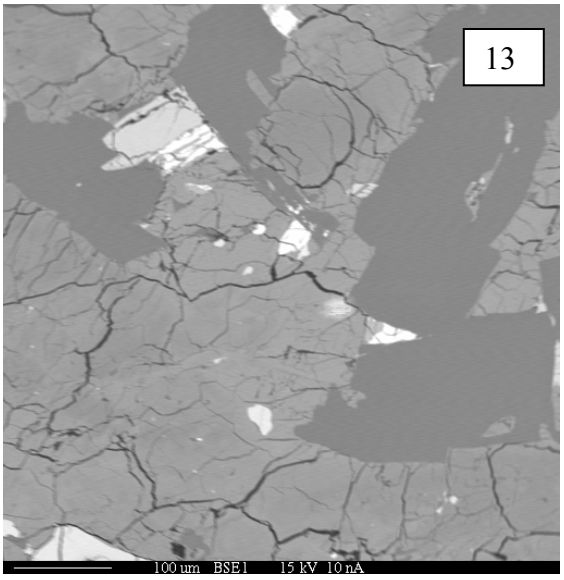
13
100 um BSE1 15 kV 10 nA

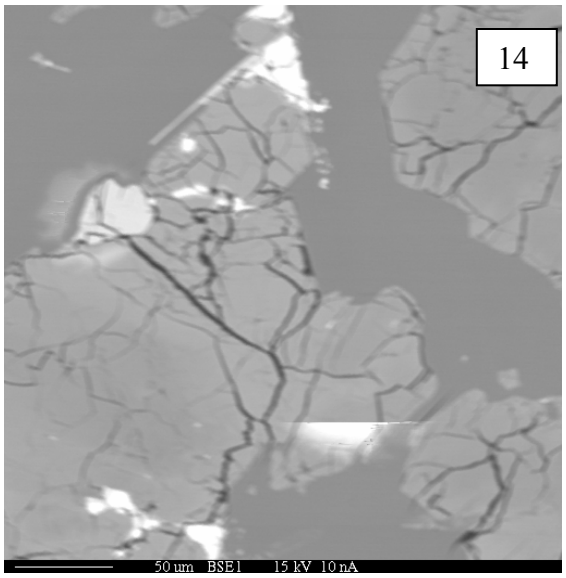
14
50 um BSE1 15 kV 10 nA

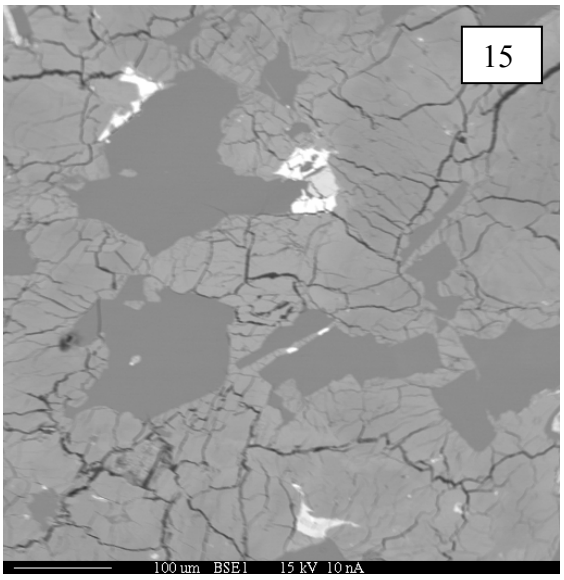
15
100 um BSE1 15 kV 10 nA

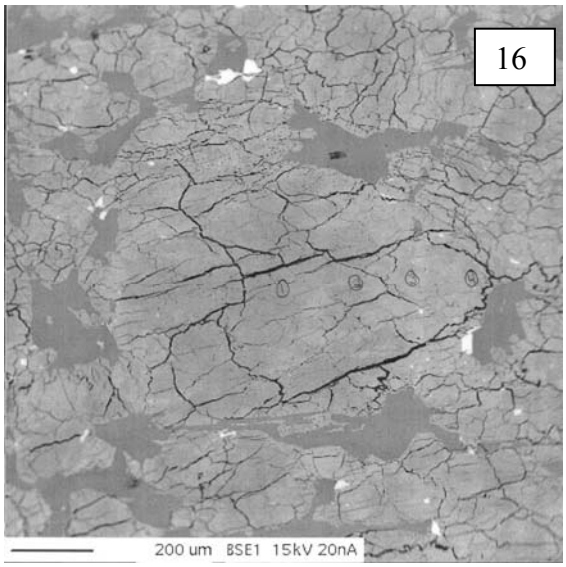
16
200 um 8SE1 15kV 20nA

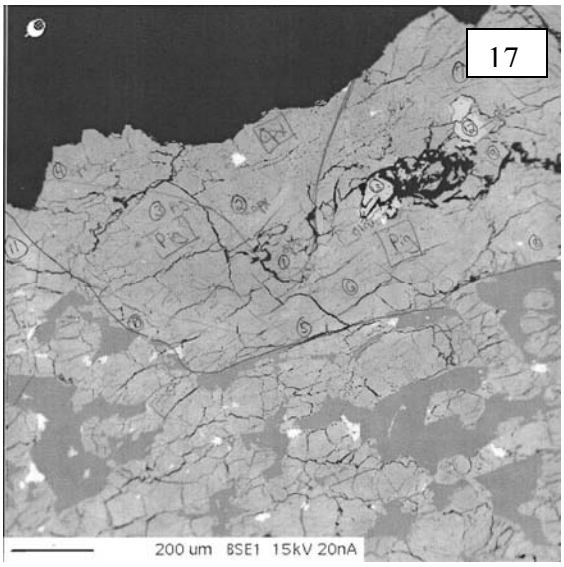
17
200 um 8SE1 15kV 20nA

79001,439 (LithA)

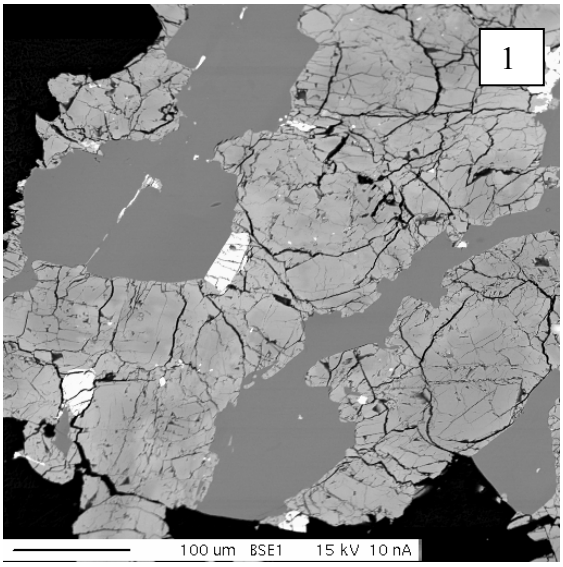
1
100 um BSE1 15 kV 10 nA

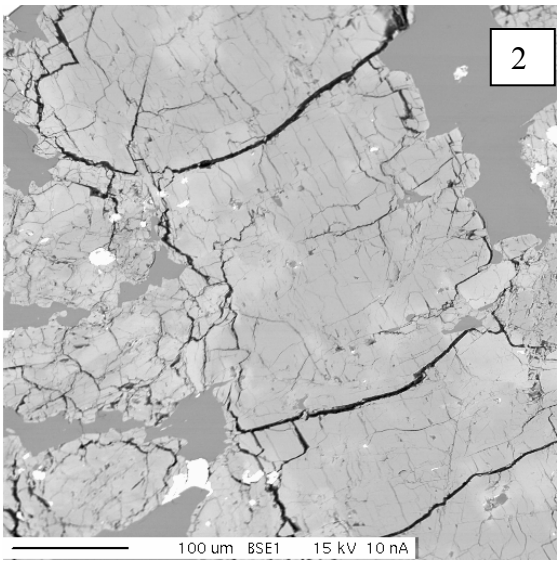
2
100 um BSE1 15 kV 10 nA

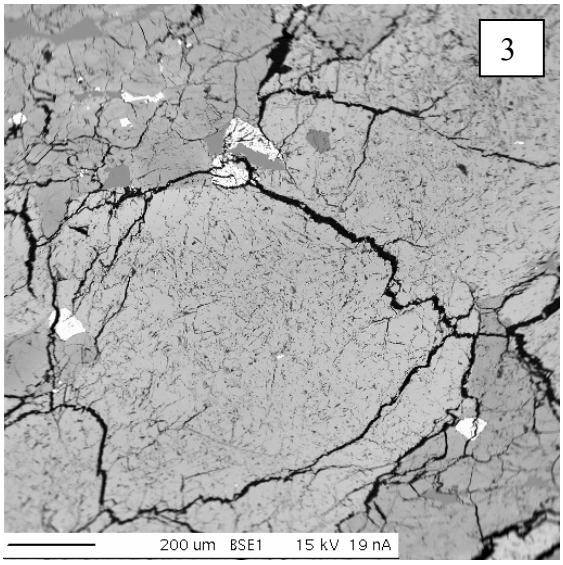
3
200 um BSE1 15 kV 19 nA

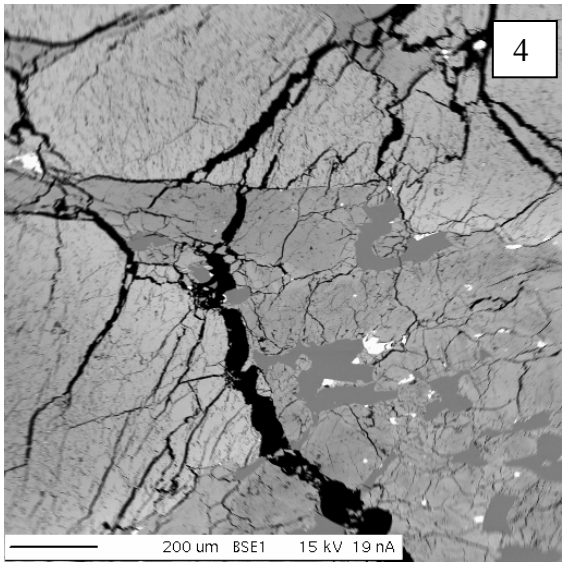
4
200 um BSE1 15 kV 19 nA

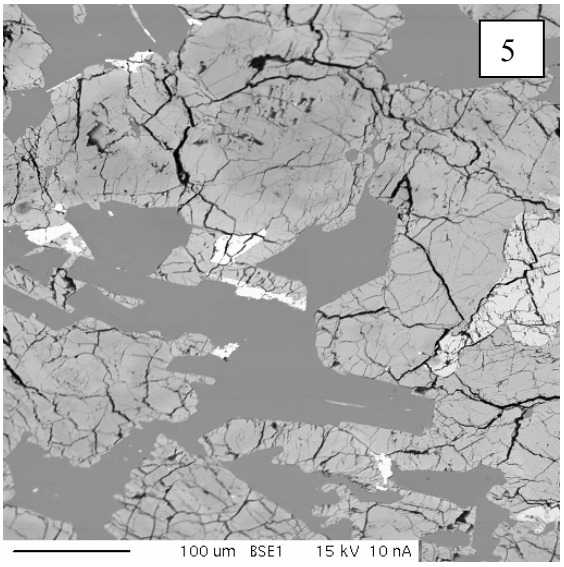
5
100 um BSE1 15 kV 10 nA

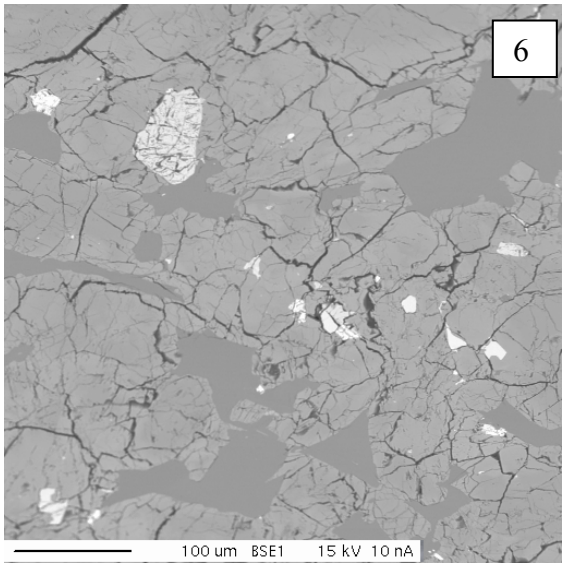
6
100 um BSE1 15 kV 10 nA

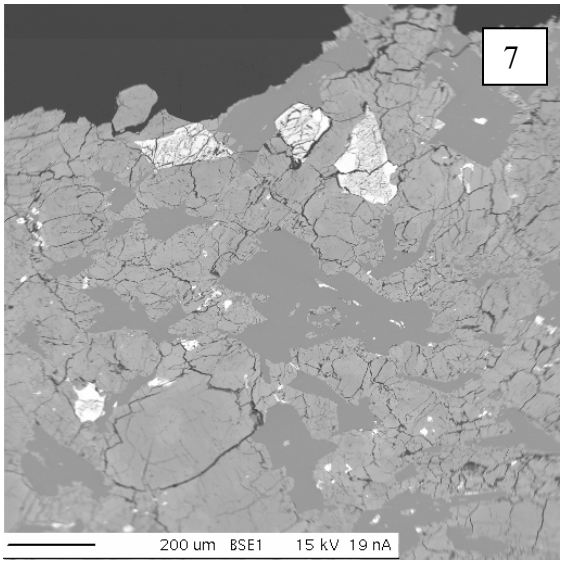
7
200 um BSE1 15 kV 19 nA

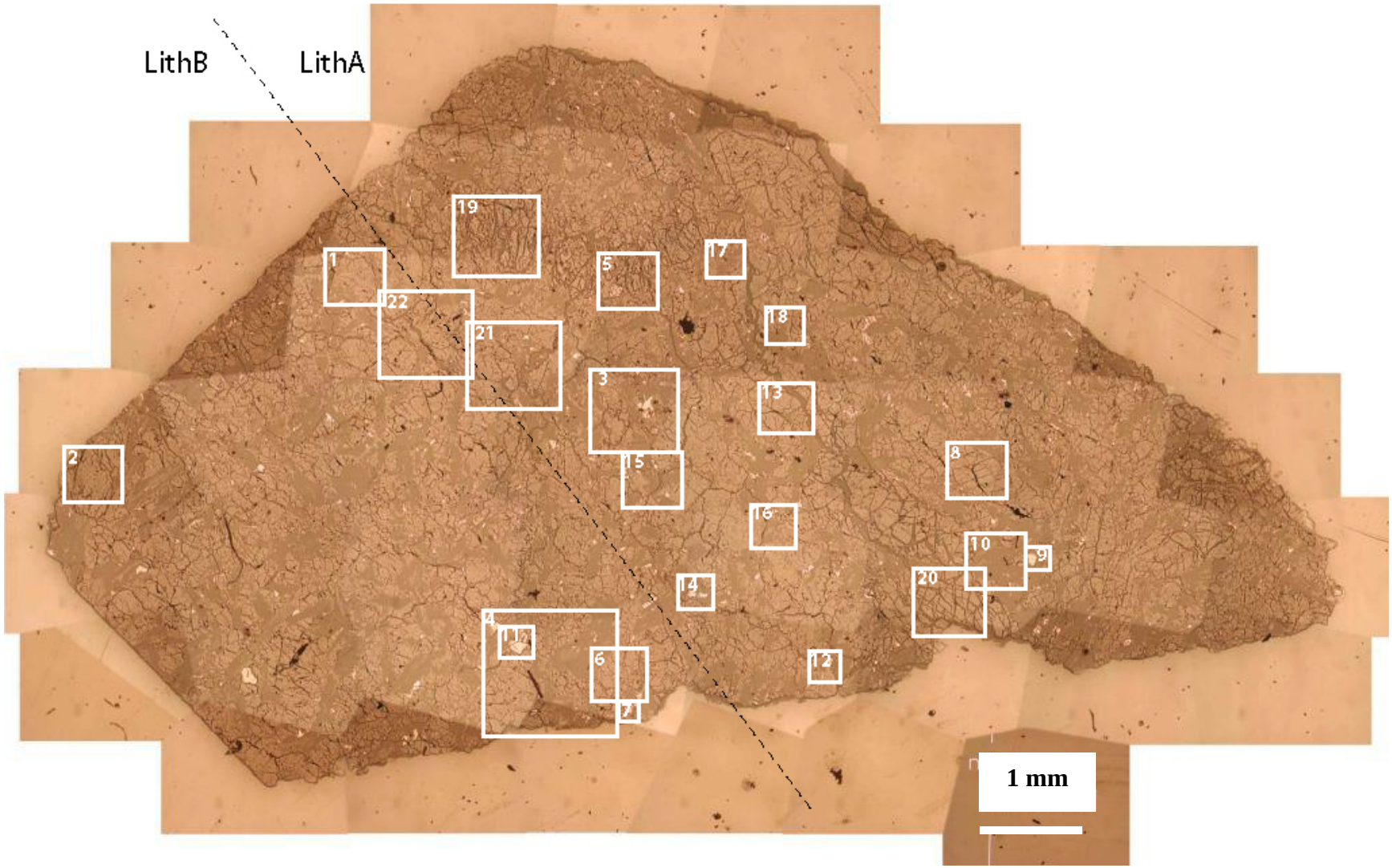

79001,615 (LithA/LithB)

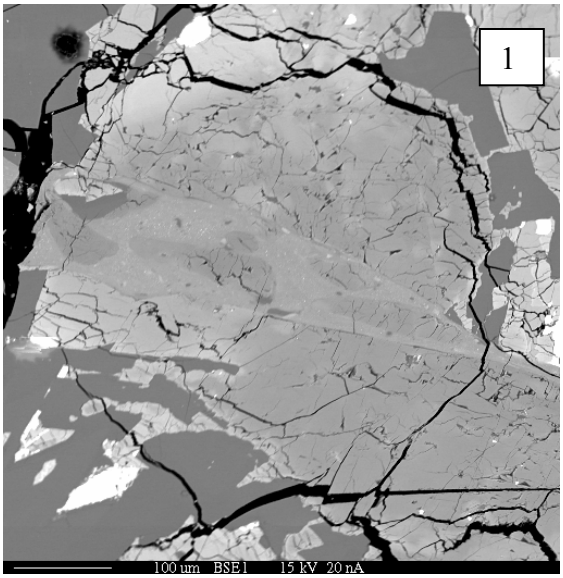
1
100 um BSE1 15 kV 20 nA

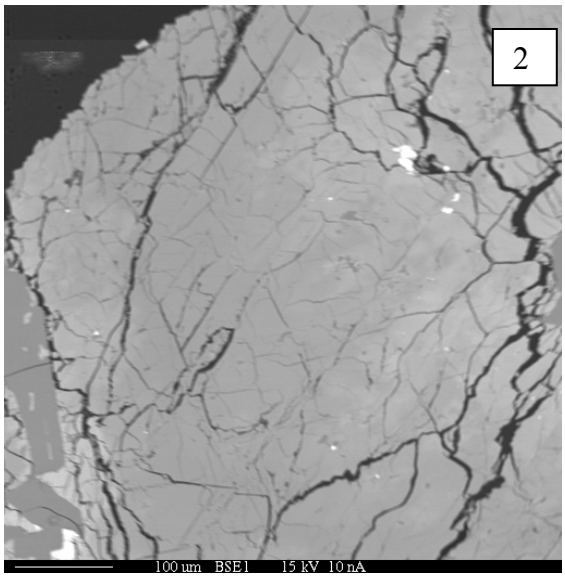
2
100 um BSE1 15 kV 10 nA

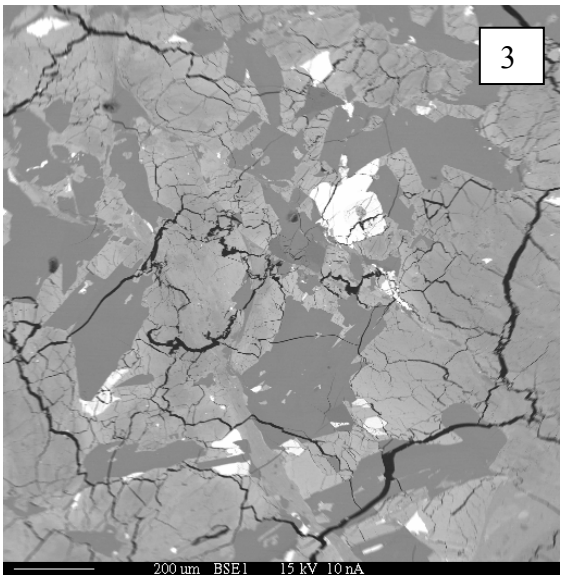
3
200 um BSE1 15 kV 10 nA

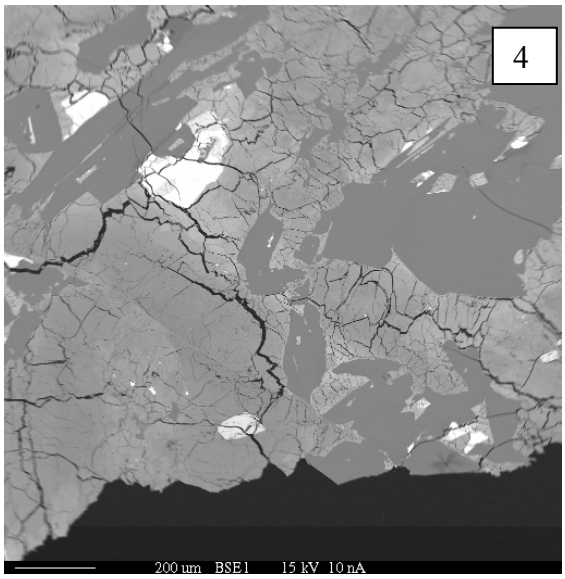
4
200 um BSE1 15 kV 10 nA

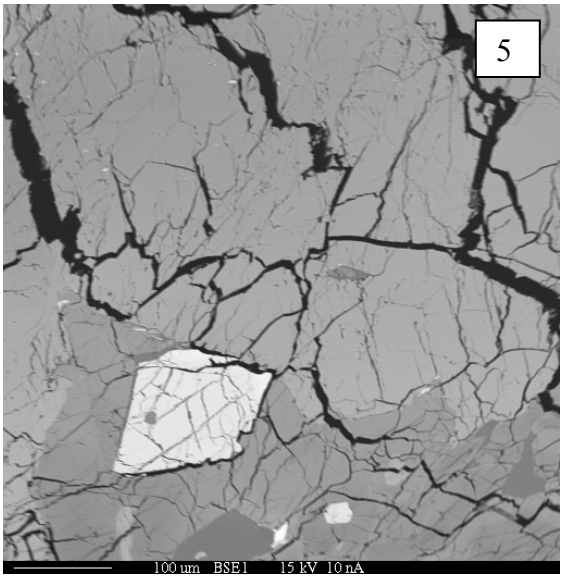
5
100 um BSE1 15 kV 10 nA

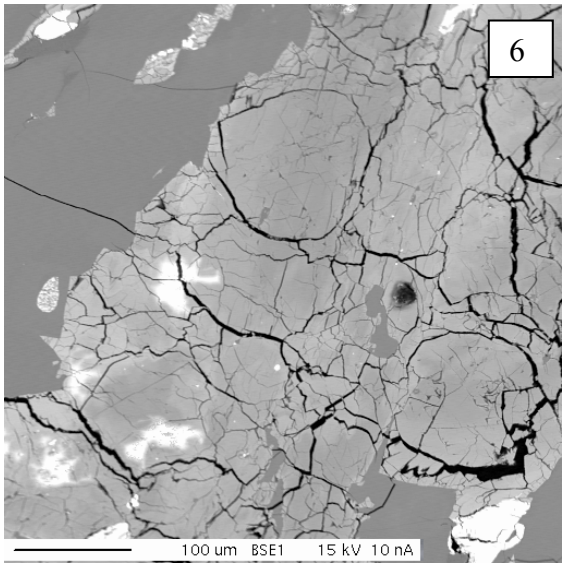
6
100 um BSE1 15 kV 10 nA

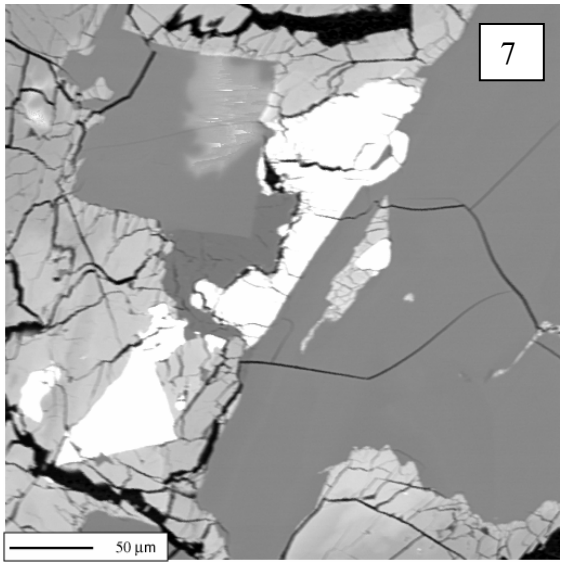
7
50 µm

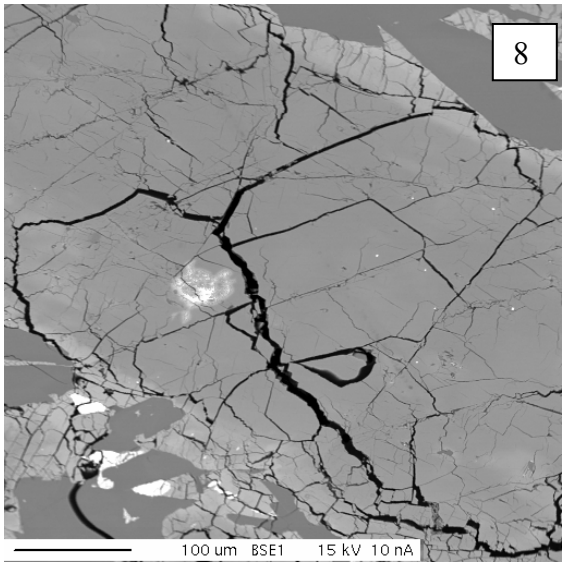
8
100 um BSE1 15 kV 10 nA

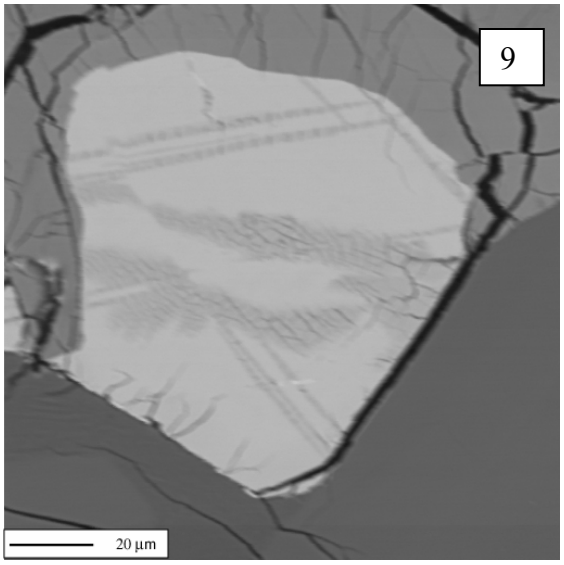
9
20 µm

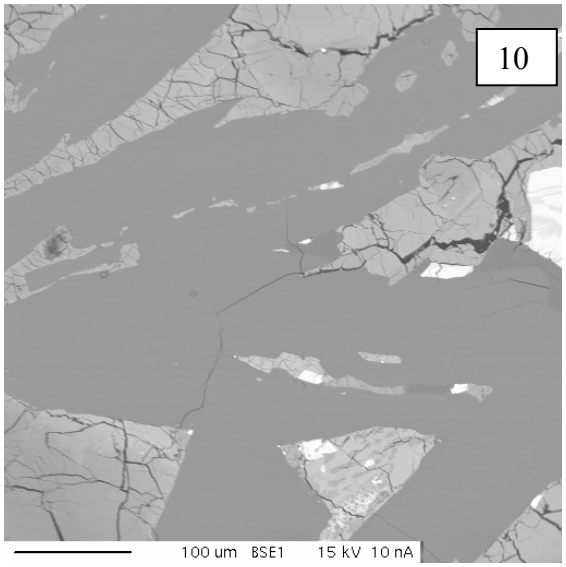
10
100 um BSE1 15 kV 10 nA

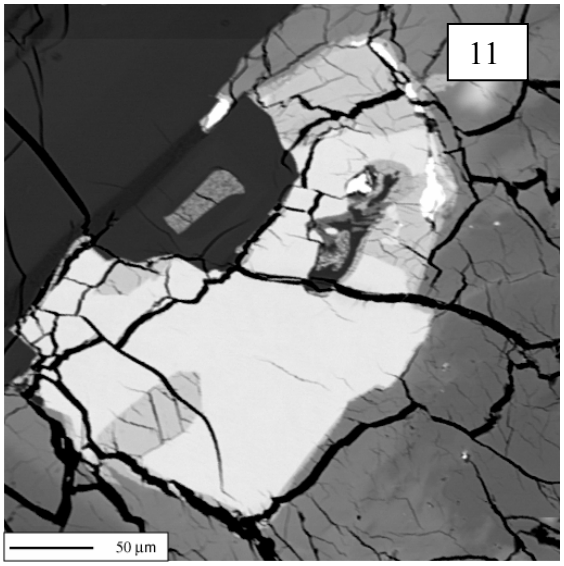
11
50 µm

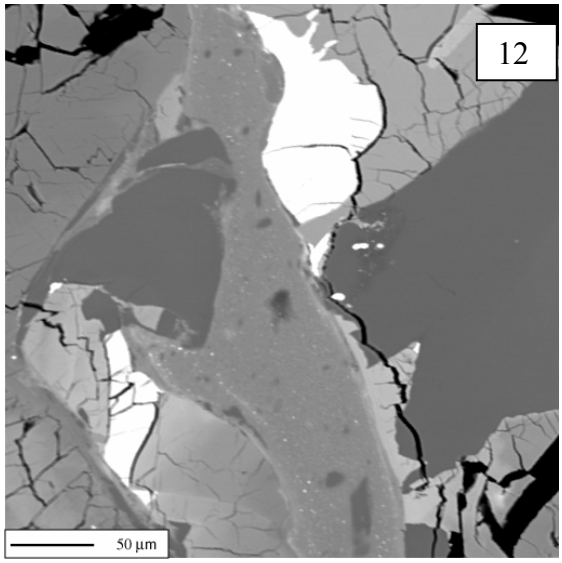
12
50 µm

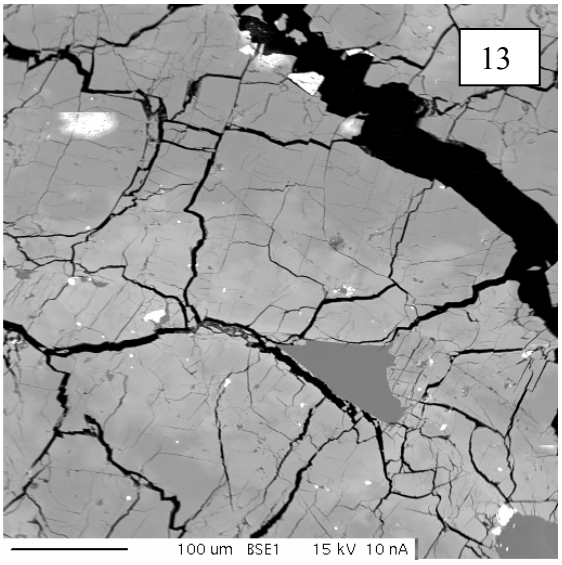
13
100 um BSE1 15 kV 10 nA

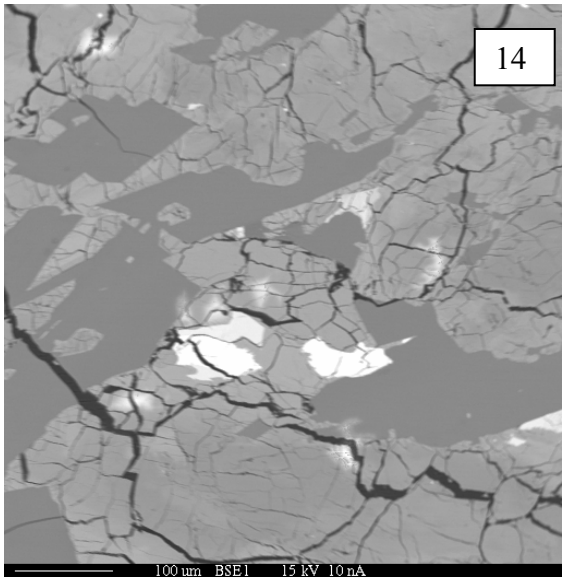
14
100 um BSE1 15 kV 10 nA

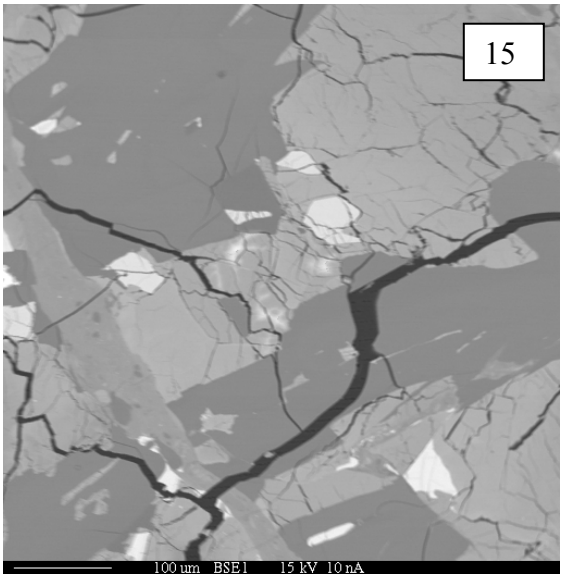
15
100 um BSE1 15 kV 10 nA

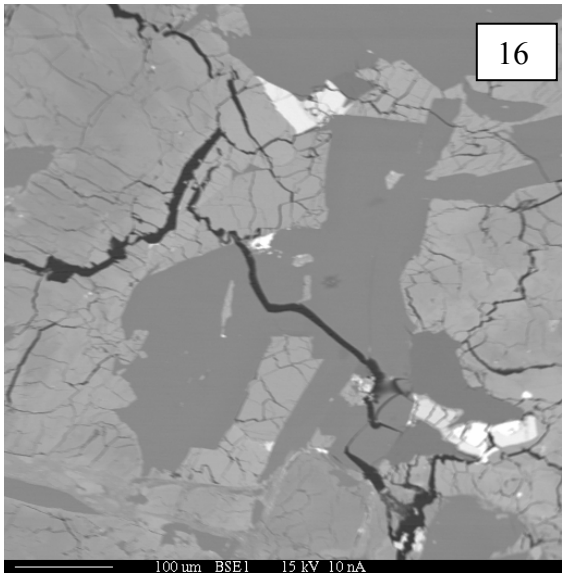
16
100 um BSE1 15 kV 10 nA

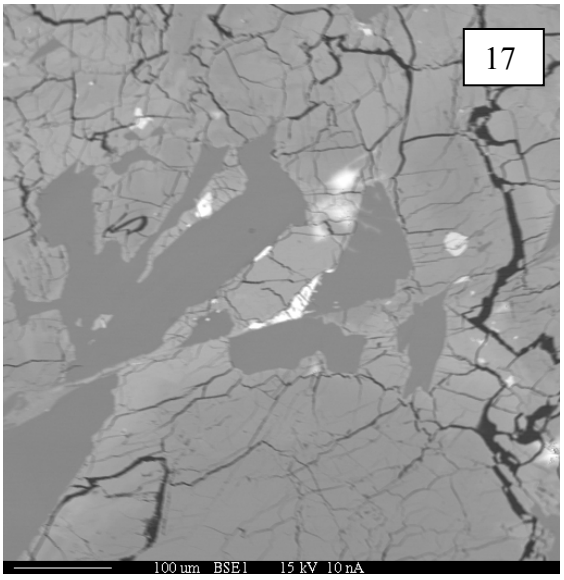
17
100 um BSE1 15 kV 10 nA

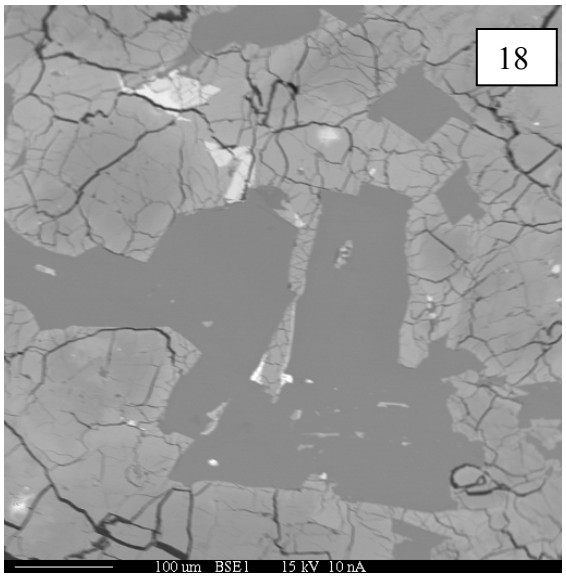
18
100 um BSE1 15 kV 10 nA

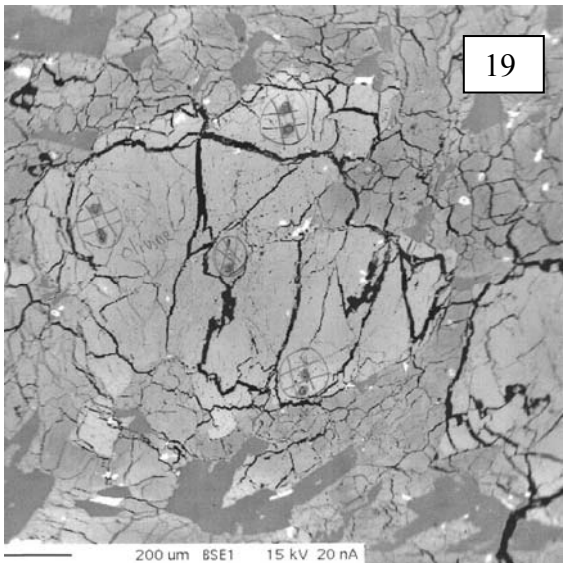
19
200 um BSE1 15 kV 20 nA

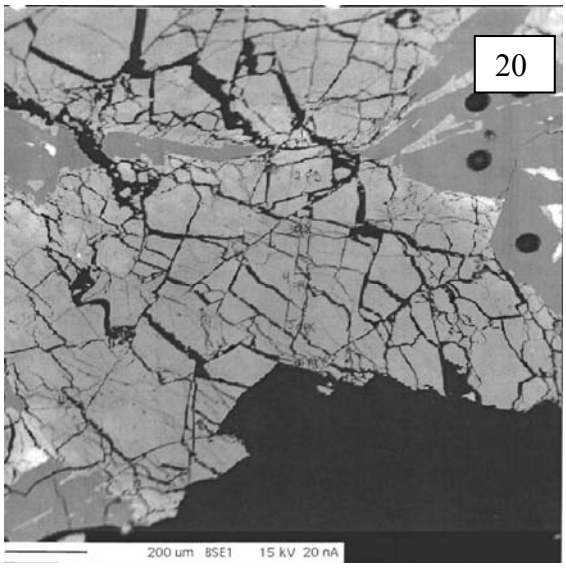
20
200 um BSE1 15 kV 20 nA

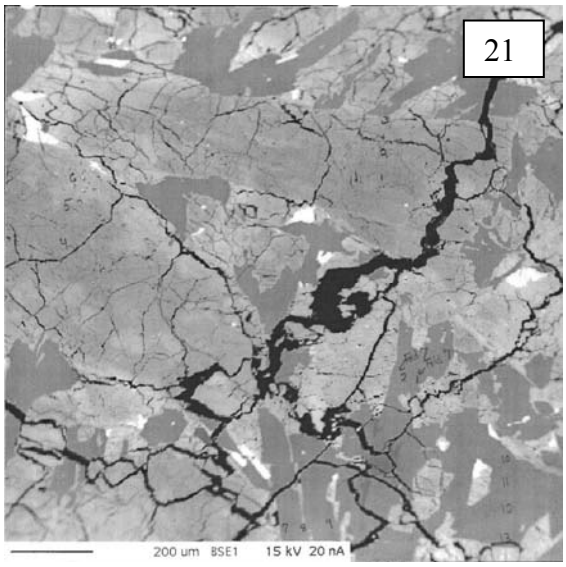
21
200 um 8SE1 15 kV 20 nA

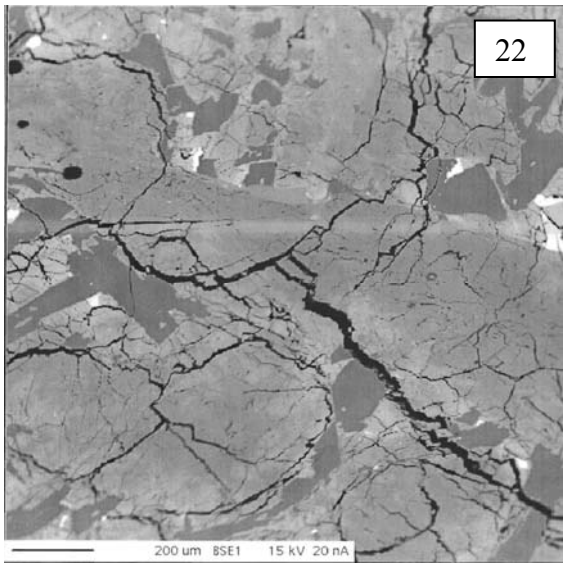
22
200 um 8SE1 15 kV 20 nA

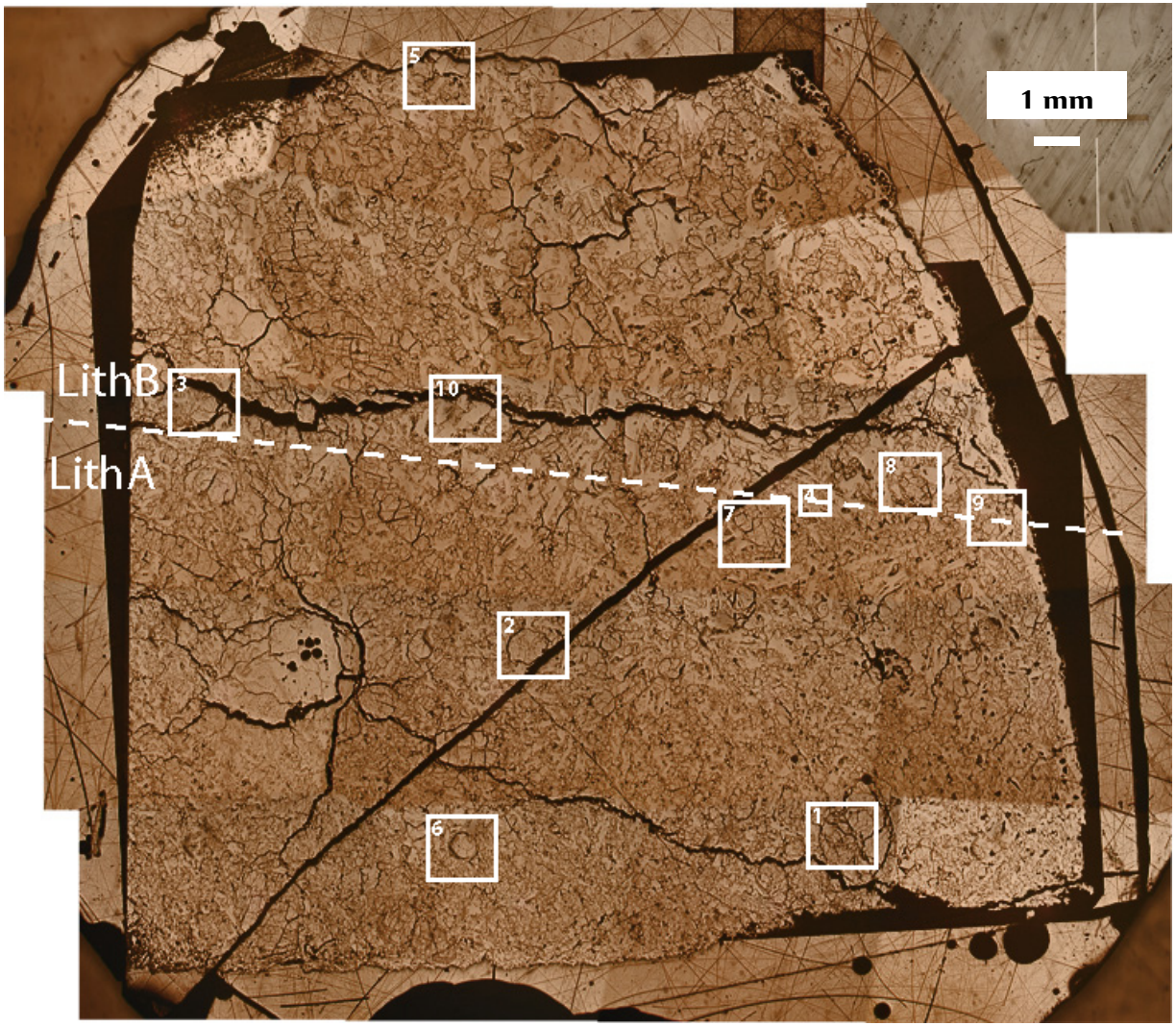

79001,39 (LithA/LithB)

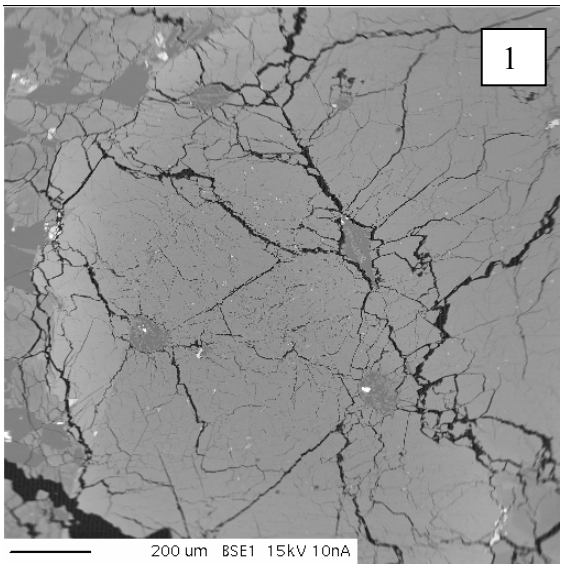
1
200 um BSE1 15kV 10nA

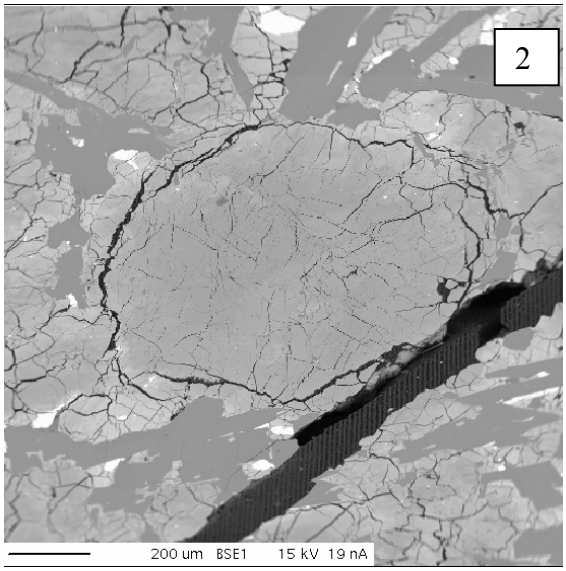
2
200 um BSE1 15 kV 19 nA

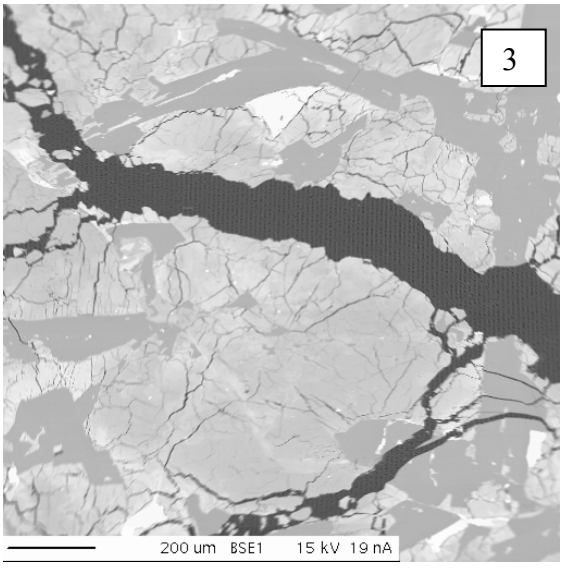
3
200 um BSE1 15 kV 19 nA

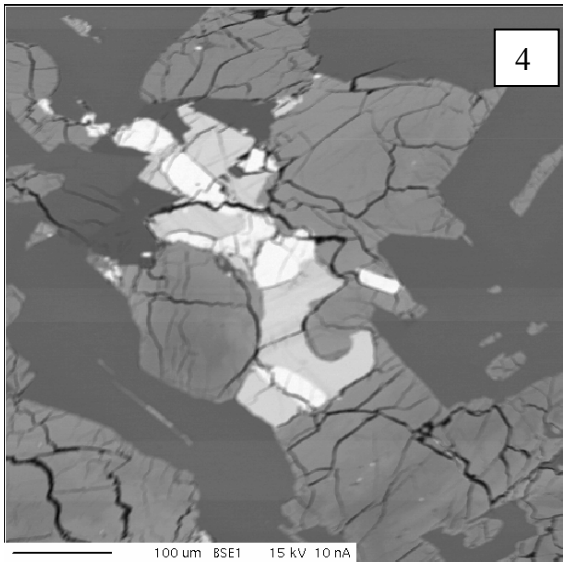
4
100 um BSE1 15 kV 10 nA

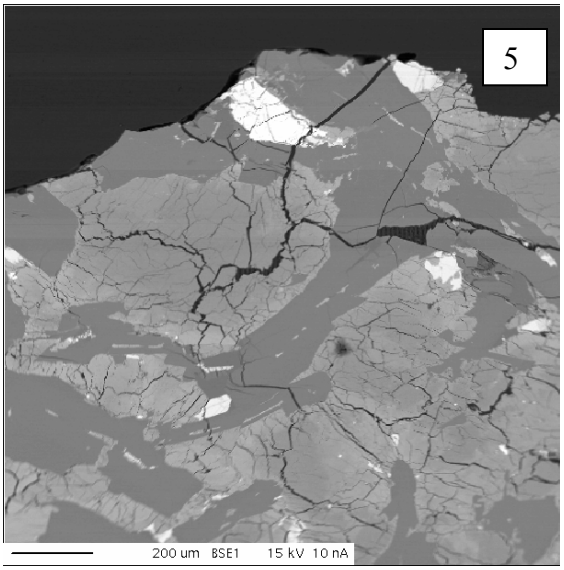
5
200 um BSE1 15 kV 10 nA

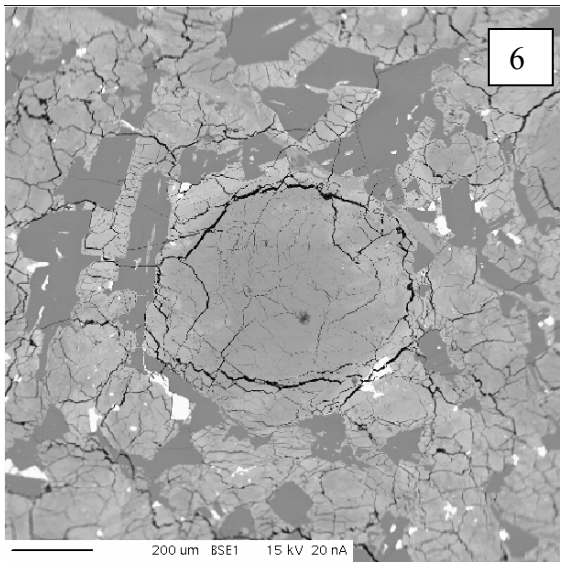
6
200 um BSE1 15 kV 20 nA

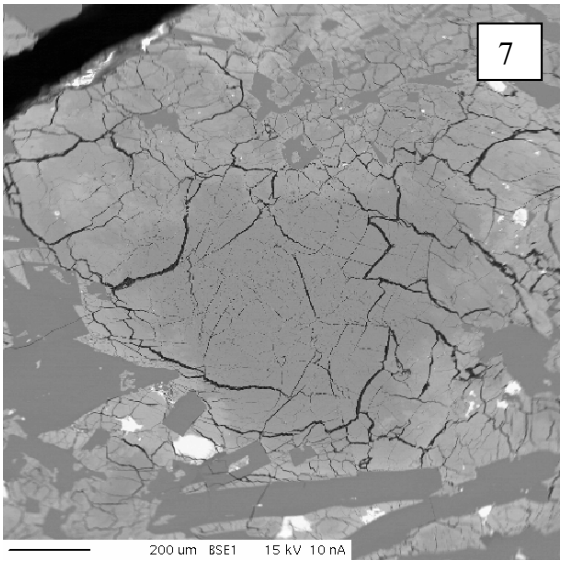
7
200 um BSE1 15 kV 10 nA

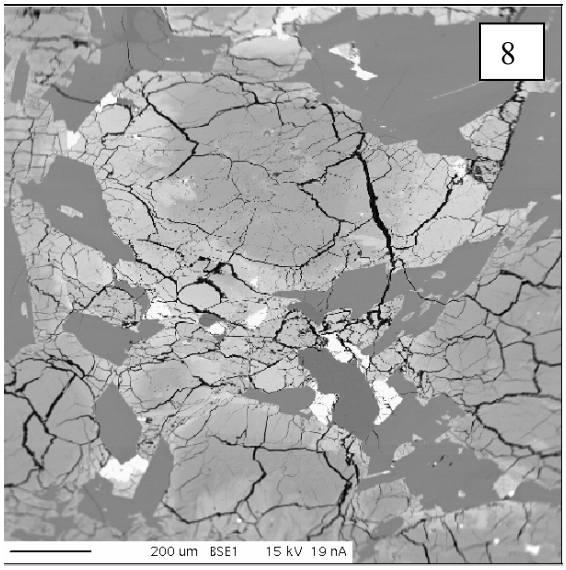
8
200 um BSE1 15 kV 19 nA

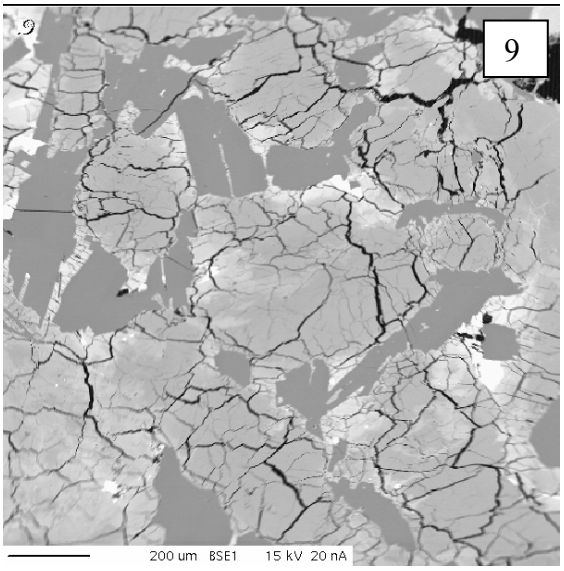
9
200 um BSE1 15 kV 20 nA

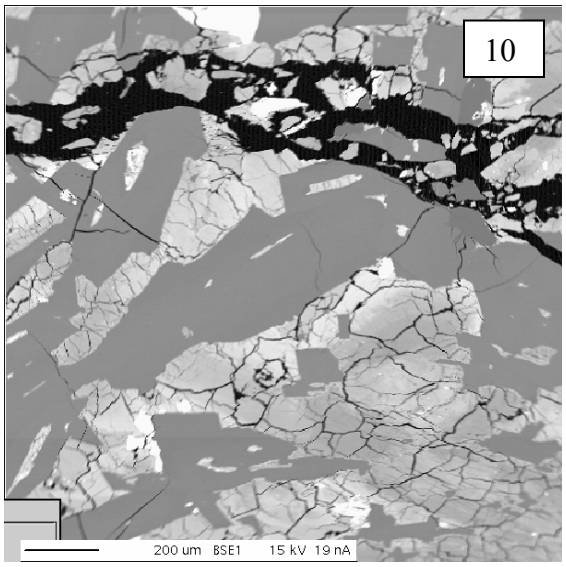
10
200 um BSE1 15 kV 19 nA

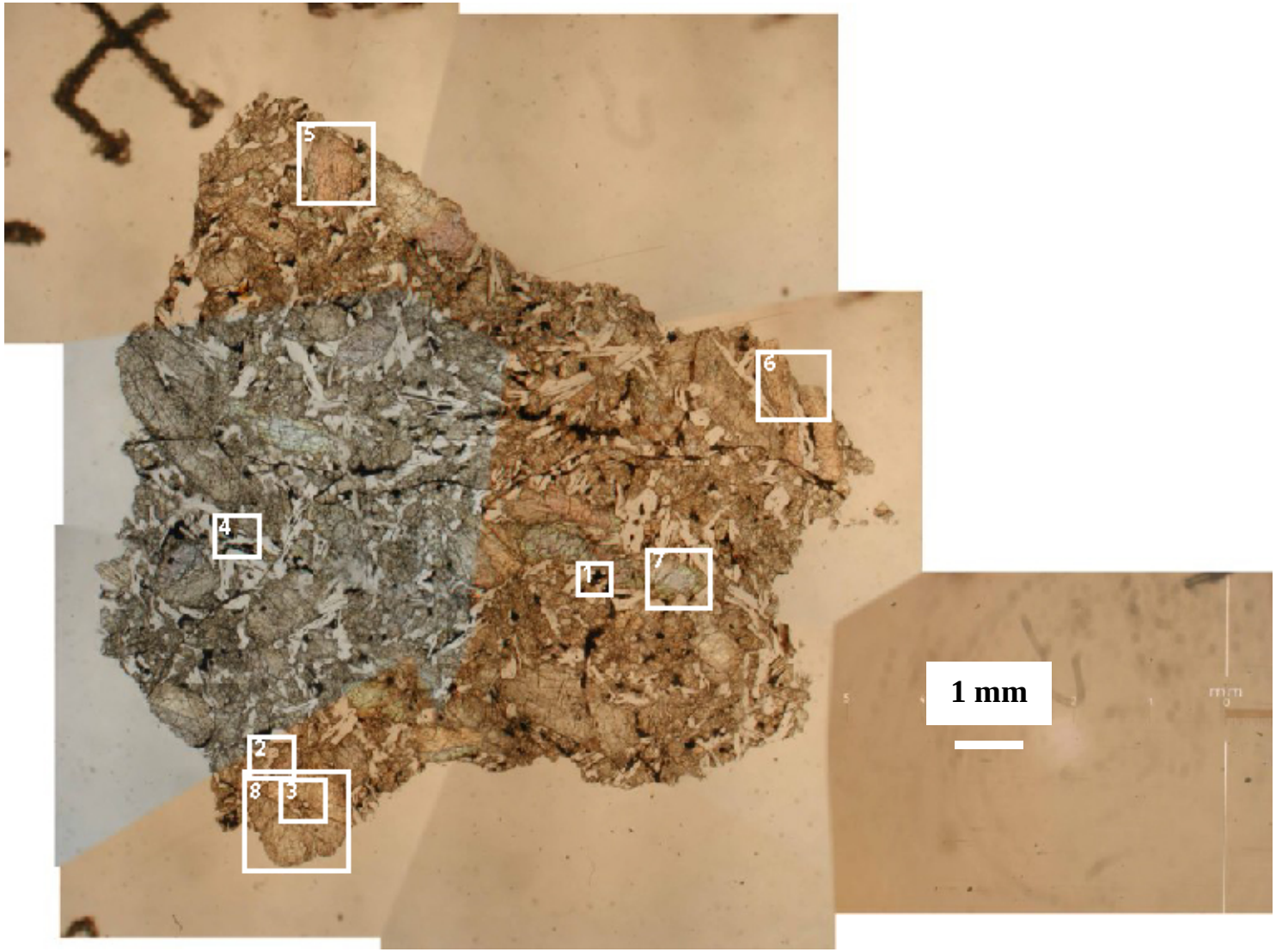

79001,457 (LithB)

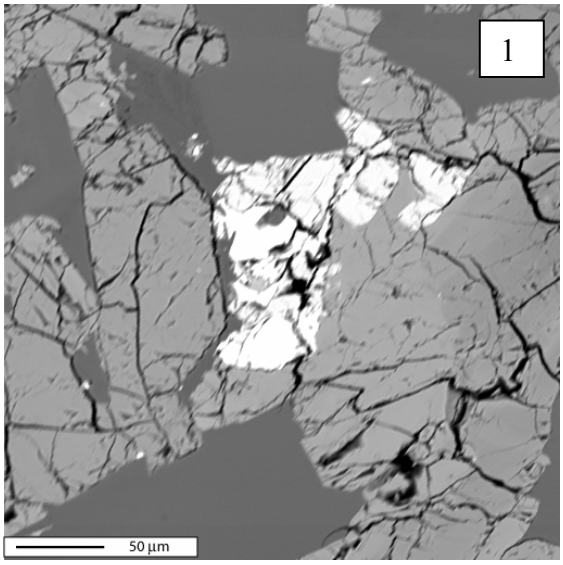
1
50 µm

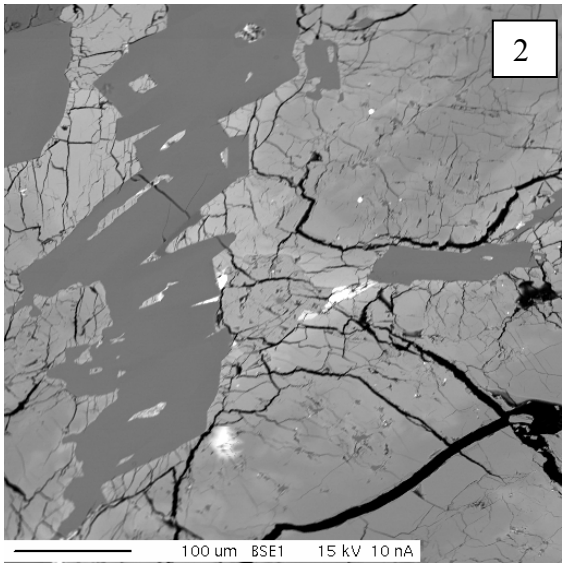
2
100 um BSE1 15 kV 10 nA

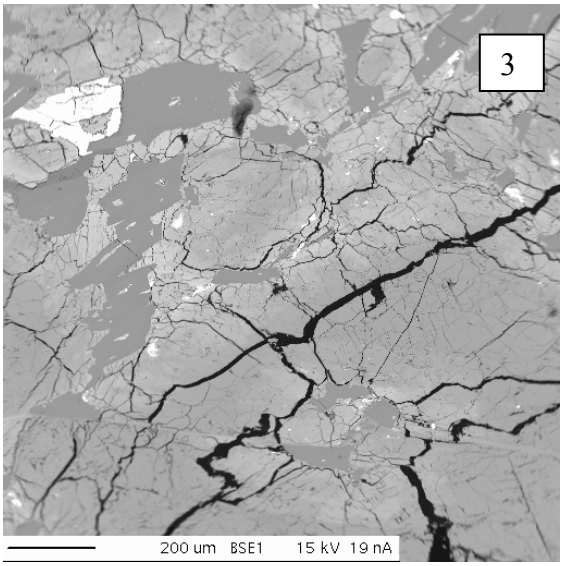
3
200 um BSE1 15 kV 19 nA

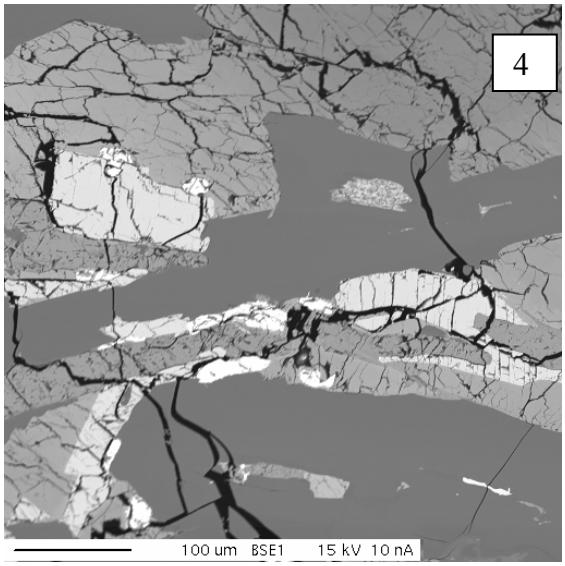
4
100 um BSE1 15 kV 10 nA

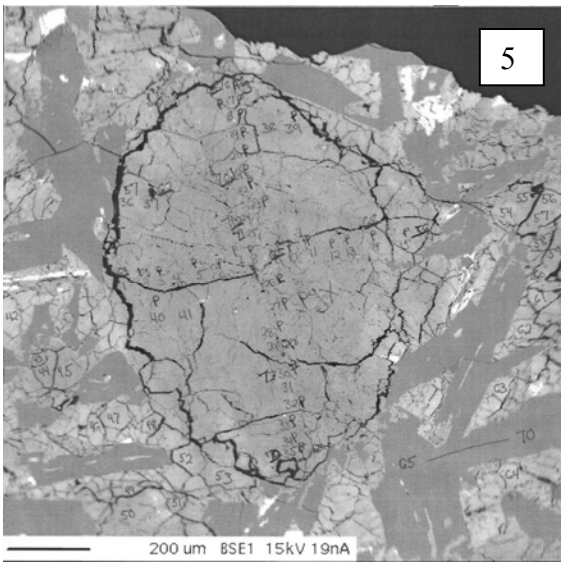
5
200 um BSE1 15kV 19nA

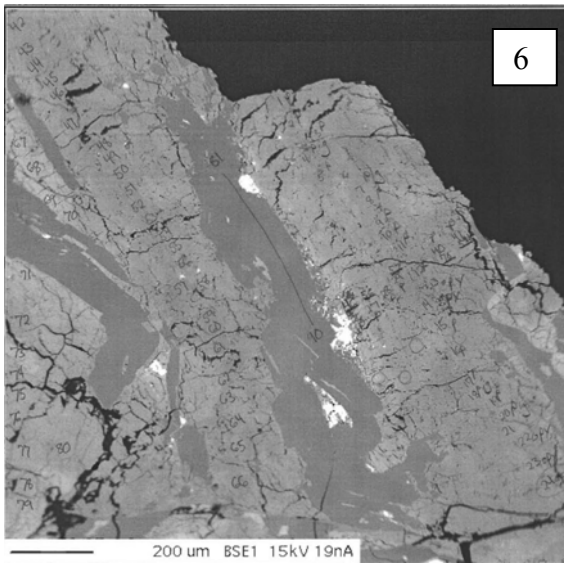
6
200 um BSE1 15kV 19nA

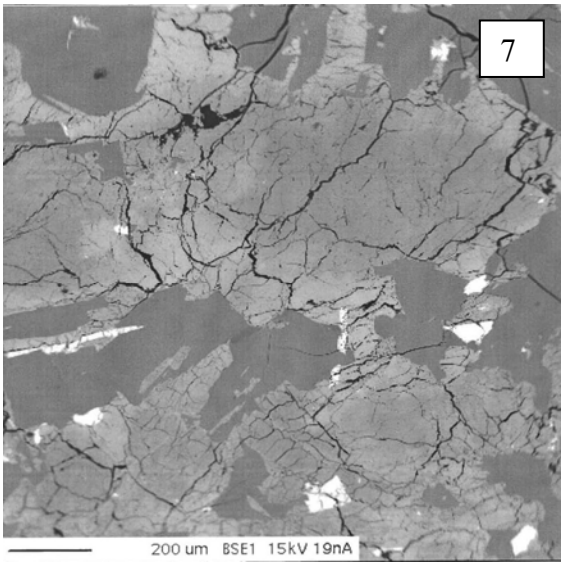
7
200 um BSE1 15kV 19nA

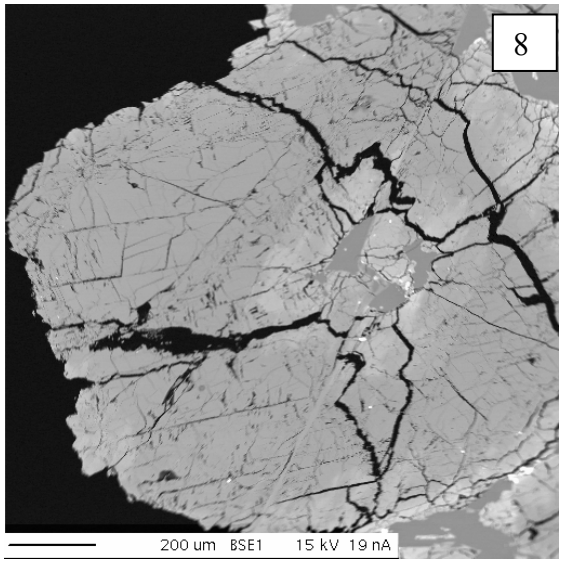
8
200 um BSE1 15 kV 19 nA

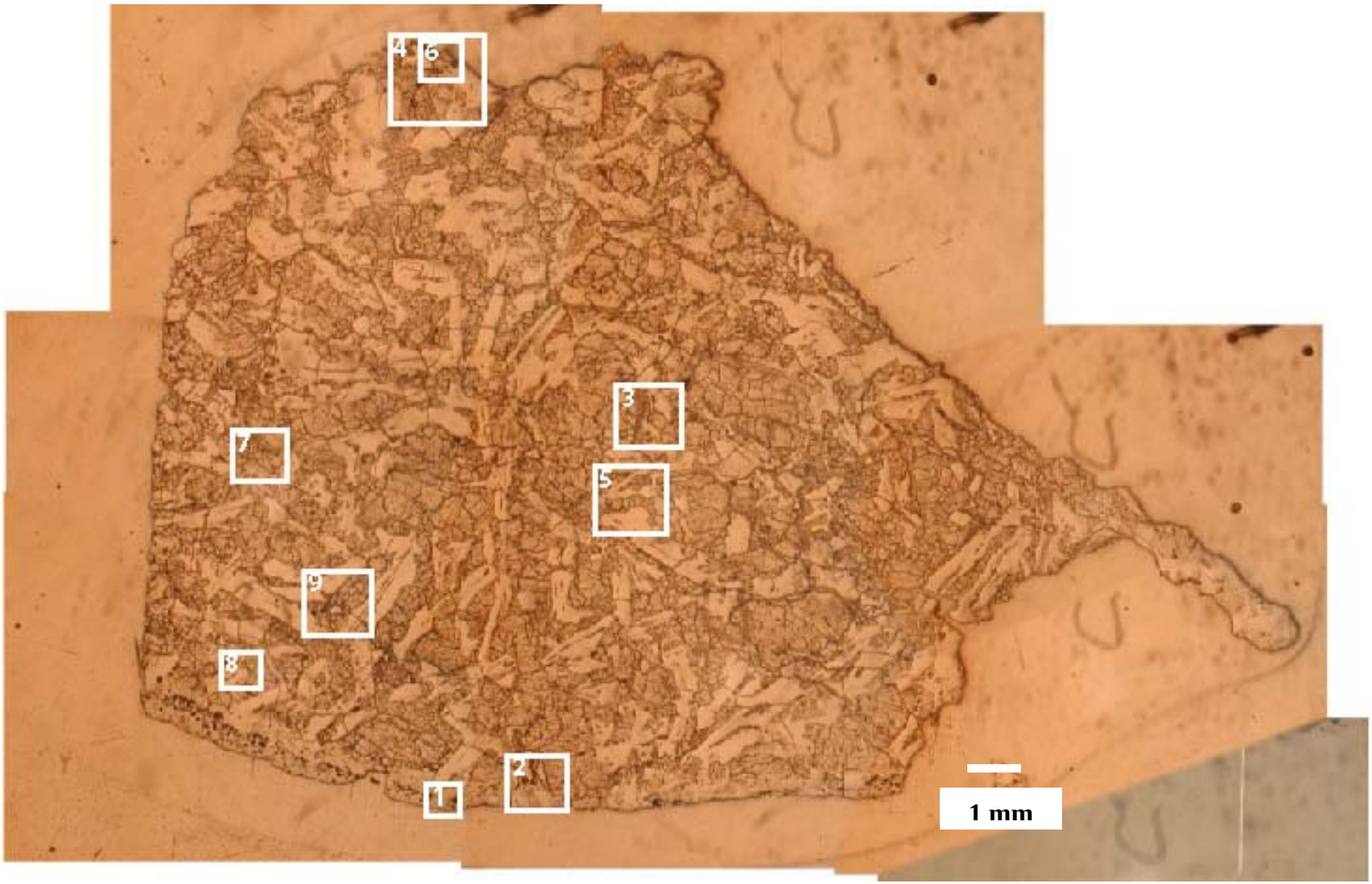

79001,392 (LithB)

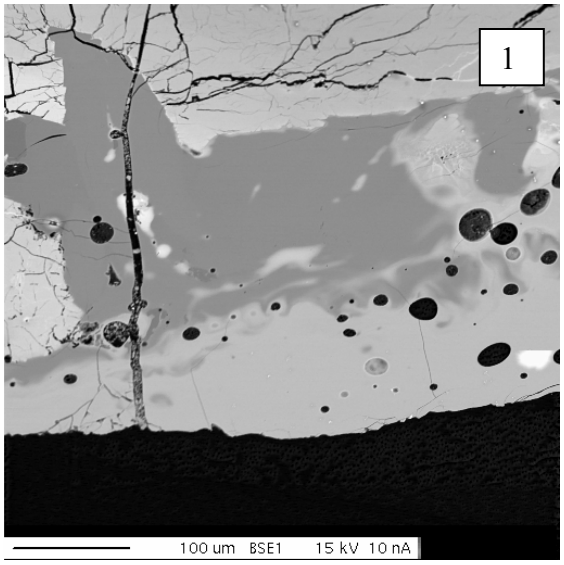
1
100 um BSE1 15 kV 10 nA

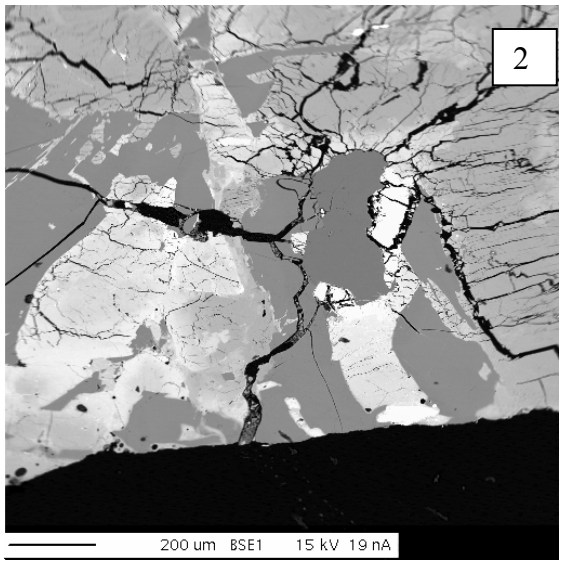
2
200 um BSE1 15 kV 19 nA

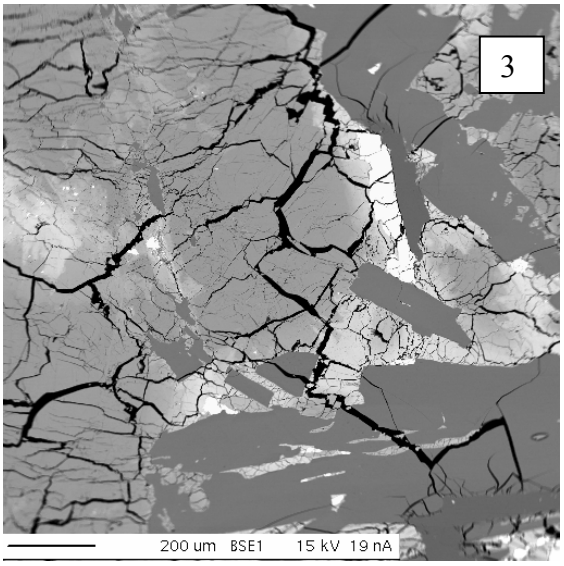
3
200 um BSE1 15 kV 19 nA

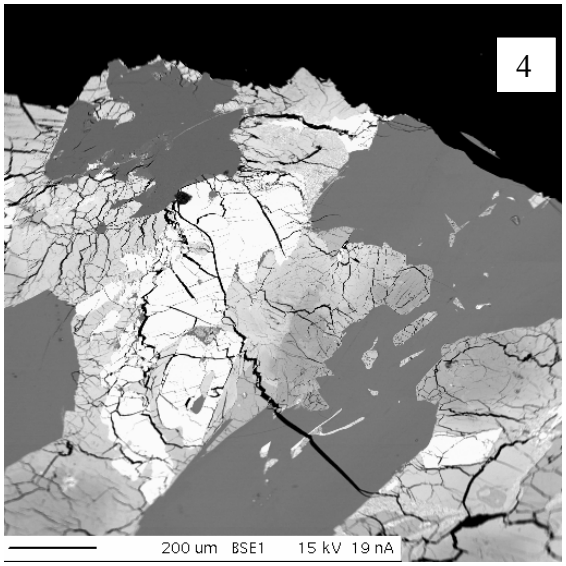
4
200 um BSE1 15 kV 19 nA

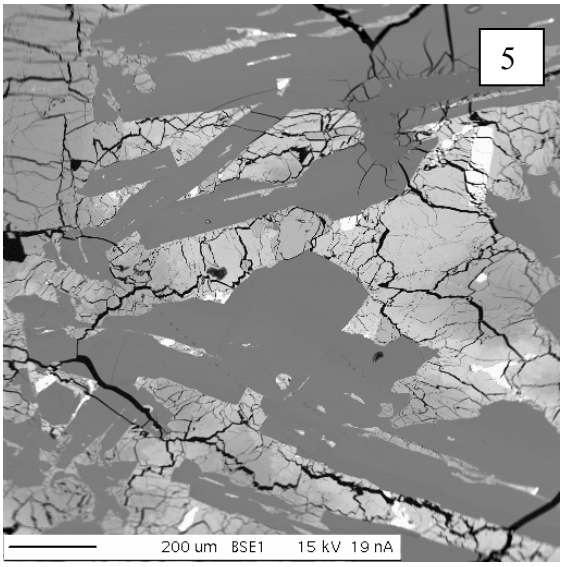
5
200 um BSE1 15 kV 19 nA

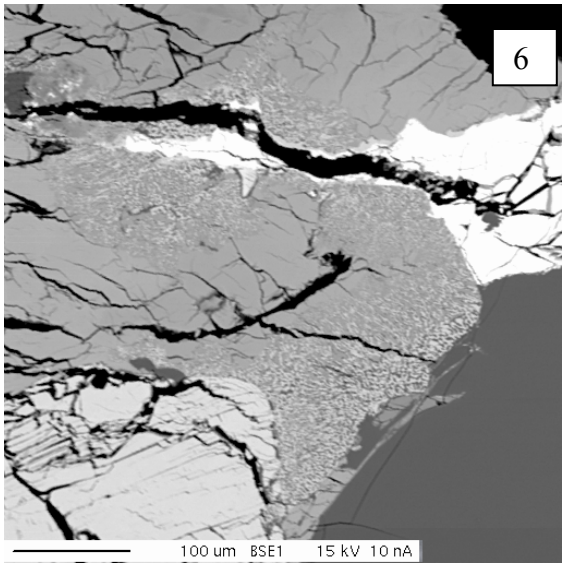
6
100 um BSE1 15 kV 10 nA

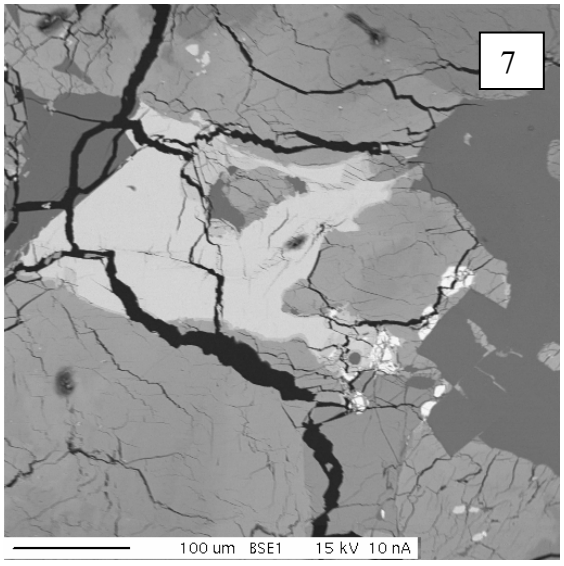
7
100 um BSE1 15 kV 10 nA

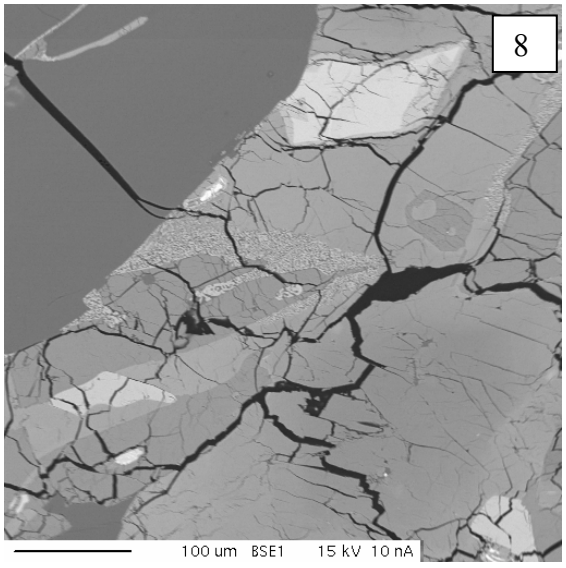
8
100 um BSE1 15 kV 10 nA

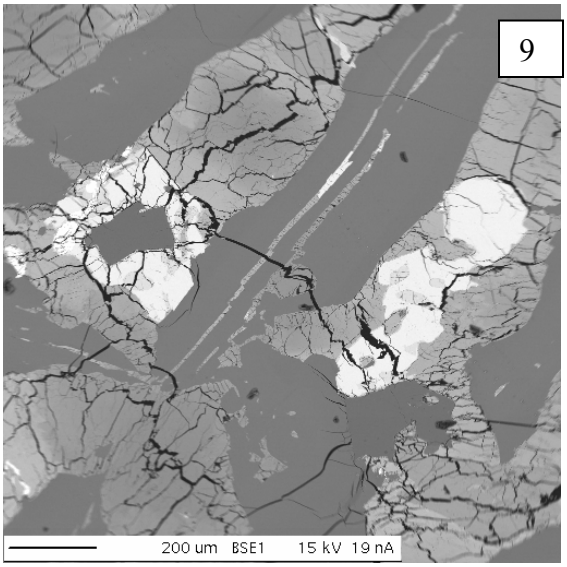
9
200 um BSE1 15 kV 19 nA

Mineral Data

All elements are in ppm. All Oxides are in wt. %.

Major- and Trace-Element Chemistry of LithA Pyroxenes

Element	jn16c03	jn16c04	jn16c05	jn16c07	jn16c08	jn16c09
Sc	32.6	38.5	49.0	30.5	46.7	40.1
Ti	702	1416	1563	685	1287	1038
V	172	175	249	177	210	222
Cr	2240	2121	3450	2483	2532	2964
Co	35.9	30.8	47.6	35.9	44.9	45.5
Ni	57.2	45.7	95.7	69.8	67.0	72.0
Zn	–	–	–	–	–	–
Ga	1.94	3.78	3.44	1.91	3.25	3.12
Rb	0.05	0.83	0.87	0.08	0.03	0.19
Sr	0.28	1.16	1.08	0.49	0.30	1.45
Y	1.83	3.94	4.45	1.60	2.99	2.88
Zr	1.57	10.3	5.96	1.29	3.34	3.37
Nb	0.05	0.22	0.26	0.05	0.05	0.11
Cs	–	–	–	–	–	–
Ba	0.18	1.07	1.30	0.16	0.13	0.55
La	0.01	0.06	0.06	0.01	0.00	0.04
Ce	0.02	0.14	0.15	0.03	0.02	0.11
Pr	0.01	0.03	0.03	0.01	0.00	0.02
Nd	0.04	0.18	0.16	0.04	0.04	0.13
Sm	0.05	0.16	0.15	0.04	0.05	0.10
Eu	0.02	0.06	0.06	0.02	0.02	0.04
Tb	0.03	0.08	0.10	0.03	0.05	0.06
Gd	0.14	0.42	0.41	0.15	0.20	0.28
Dy	0.28	0.66	0.79	0.26	0.47	0.47
Ho	0.07	0.15	0.17	0.06	0.12	0.11
Er	0.23	0.48	0.50	0.20	0.37	0.33
Yb	0.23	0.44	0.59	0.20	0.41	0.33
Lu	0.04	0.07	0.09	0.04	0.06	0.05
Hf	0.05	0.32	0.22	0.05	0.13	0.11
Ta	0.00	0.01	0.01	<0.001	<0.003	0.00
Pb	0.01	0.03	0.08	0.03	0.02	0.03
SiO2	52.6	52.1	51.8	53.7	52.9	50.0
TiO2	0.08	0.23	0.27	0.06	0.12	0.60
Al2O3	0.56	0.81	0.83	0.64	0.86	0.65
Cr2O3	0.44	0.44	0.53	0.42	0.41	0.13
MgO	23.4	19.9	18.8	23.5	21.7	14.9
CaO	4.28	5.12	6.10	3.65	5.55	5.22
MnO	0.55	0.64	0.64	0.54	0.65	0.94
FeO	16.5	20.5	21.1	17.7	18.5	27.4
Na2O	0.03	0.05	0.06	0.07	0.05	0.09
Sum	98.4	99.8	100.0	100.3	100.8	99.8

Major- and Trace-Element Chemistry of LithA Pyroxenes

Element	jn16c10	jn16c11	jn16c13	jn16c14	jn17c15	jn17c16	jn17c17	jn17c18
Sc	49.6	61.3	48.5	36.5	42.6	41.5	42.7	51.4
Ti	2307	3161	1682	1226	1135	1218	785	1140
V	147	112	222	188	243	200	232	274
Cr	1672	899	2688	2624	3433	2496	2978	3828
Co	45.6	51.5	36.6	44.1	53.8	40.1	44.9	63.6
Ni	48.8	52.7	57.6	93.8	83.1	53.1	66.9	115.0
Zn	–	–	–	–	67.3	55.0	51.4	76.9
Ga	4.06	7.02	4.17	3.39	3.25	3.52	2.64	2.99
Rb	0.02	0.03	0.45	0.89	0.08	0.14	0.06	<0.074
Sr	0.27	0.40	2.20	1.37	0.78	1.25	0.96	0.18
Y	4.85	3.95	5.92	3.49	2.56	3.31	2.06	2.35
Zr	2.39	7.09	7.46	4.41	2.60	2.69	0.53	0.97
Nb	0.03	0.04	0.16	0.12	0.06	0.06	0.03	0.05
Cs	–	–	–	–	<0.034	<0.019	<0.026	<0.048
Ba	0.05	0.16	1.01	0.70	0.25	0.42	0.13	0.09
La	0.01	0.00	0.13	0.06	0.02	0.05	0.01	<0.018
Ce	0.03	0.02	0.32	0.17	0.07	0.11	<0.020	<0.015
Pr	0.01	0.01	0.05	0.03	0.01	0.03	<0.012	<0.015
Nd	0.07	0.06	0.38	0.19	0.06	0.12	<0.11	<0.085
Sm	0.12	0.07	0.28	0.13	0.10	0.11	<0.096	<0.11
Eu	0.04	0.02	0.11	0.06	0.03	0.06	0.03	<0.029
Tb	0.08	0.06	0.13	0.07	0.04	0.06	0.03	0.05
Gd	0.36	0.23	0.66	0.36	0.27	0.30	0.15	<0.11
Dy	0.79	0.58	1.05	0.61	0.34	0.54	0.35	0.40
Ho	0.20	0.16	0.24	0.13	0.11	0.14	0.08	0.11
Er	0.59	0.57	0.67	0.42	0.27	0.42	0.27	0.29
Yb	0.66	0.74	0.68	0.38	0.39	0.37	0.30	0.38
Lu	0.11	0.13	0.10	0.07	0.06	0.06	0.04	0.06
Hf	0.13	0.37	0.30	0.17	0.10	0.10	<0.039	<0.050
Ta	<0.002	<0.002	0.01	0.00	<0.017	<0.010	<0.009	<0.017
Pb	0.02	0.02	0.06	0.03	0.16	0.05	0.04	0.07
SiO2	51.0	51.4	50.7	53.5	51.4	51.6	53.0	51.6
TiO2	0.32	0.49	0.27	0.14	0.24	0.22	0.13	0.33
Al2O3	0.68	0.69	0.92	0.93	0.75	0.70	0.83	0.72
Cr2O3	0.28	0.25	0.38	0.55	0.30	0.30	0.56	0.51
MgO	17.6	16.7	18.7	22.8	18.7	18.7	21.1	18.6
CaO	5.57	5.87	6.67	4.57	5.18	4.73	6.20	5.42
MnO	0.67	0.62	0.58	0.62	0.68	0.69	0.53	0.69
FeO	23.3	24.2	20.4	17.2	21.8	23.1	17.3	22.2
Na2O	0.07	0.07	0.08	0.03	0.07	0.05	0.06	0.04
Sum	99.5	100.2	98.7	100.4	99.1	100.1	99.7	100.0

Major- and Trace-Element Chemistry of LithA Pyroxenes

Element	jn17d04	jn17d05	jn17d08	jn17d09	jn17d10	jn17d11	jn17d12	jn17d13
Sc	31.7	45.9	33.0	40.5	44.0	42.4	30.2	46.0
Ti	609	1805	1048	1175	1456	1666	1514	1768
V	182	209	175	203	221	164	156	177
Cr	2441	2658	2208	2493	2589	1968	2092	2007
Co	39.8	47.9	33.6	35.3	30.8	37.8	33.8	29.7
Ni	75.9	63.8	48.3	58.5	41.6	49.7	58.0	45.0
Zn	44.3	77.3	43.9	45.1	44.3	62.3	45.1	47.3
Ga	1.97	4.44	2.65	2.91	4.00	4.85	3.13	4.97
Rb	0.02	0.09	0.16	0.25	0.15	0.09	0.38	0.03
Sr	0.12	0.83	0.52	0.69	0.79	1.45	1.19	0.88
Y	1.41	4.59	2.64	3.21	3.76	3.83	3.64	4.46
Zr	0.63	7.05	4.73	10.6	6.68	8.79	7.49	12.10
Nb	0.04	0.10	0.15	0.32	0.27	0.12	0.25	0.13
Cs	<0.015	0.02	0.02	0.02	0.03	0.01	0.03	<0.020
Ba	0.02	0.37	0.39	1.10	0.37	0.48	1.28	0.31
La	<0.010	0.06	0.04	0.02	0.04	0.01	0.07	0.02
Ce	<0.008	0.16	0.10	0.06	0.10	0.06	0.20	0.05
Pr	<0.006	0.02	0.02	0.01	0.02	0.01	0.03	0.01
Nd	<0.030	0.18	0.12	0.08	0.13	0.09	0.22	0.15
Sm	0.07	0.15	0.09	0.10	0.16	0.10	0.15	0.11
Eu	0.01	0.06	0.03	0.04	0.06	0.05	0.07	0.08
Tb	0.02	0.09	0.05	0.07	0.08	0.07	0.08	0.11
Gd	0.07	0.45	0.26	0.27	0.29	0.30	0.40	0.46
Dy	0.26	0.71	0.44	0.57	0.66	0.62	0.65	0.85
Ho	0.04	0.17	0.11	0.12	0.15	0.14	0.14	0.18
Er	0.18	0.58	0.32	0.40	0.47	0.46	0.44	0.50
Yb	0.20	0.58	0.32	0.44	0.42	0.52	0.43	0.50
Lu	0.03	0.10	0.05	0.06	0.07	0.08	0.06	0.09
Hf	<0.032	0.24	0.16	0.31	0.26	0.33	0.27	0.46
Ta	<0.011	<0.004	0.01	0.02	0.02	0.01	0.01	<0.010
Pb	0.02	0.02	0.01	0.02	0.03	0.02	0.02	0.03
SiO2	53.8	50.1	53.0	53.4	51.5	51.8	51.9	51.4
TiO2	0.12	0.60	0.17	0.15	0.39	0.23	0.17	0.39
Al2O3	0.21	0.67	0.91	0.90	1.02	0.82	0.65	0.96
Cr2O3	0.56	0.24	0.53	0.56	0.42	0.41	0.31	0.40
MgO	24.2	15.9	22.4	22.4	17.9	19.4	20.3	17.3
CaO	4.03	5.58	4.36	5.51	6.41	5.21	3.78	6.74
MnO	0.55	0.68	0.62	0.57	0.73	0.58	0.64	0.69
FeO	16.9	25.2	17.8	16.4	21.4	20.7	21.8	22.1
Na2O	0.04	0.08	0.04	0.05	0.08	0.10	0.03	0.07
Sum	100.4	99.1	99.8	100.0	99.8	99.2	99.5	100.0

Major- and Trace-Element Chemistry of LithA Pyroxenes

Element	jn17d14	jn17d15	jn17d18	jn17e03	jn17e04	jn16c12	jn17d06	jn16c15
Sc	46.8	41.0	41.2	55.3	34.9	51.0	48.7	42.6
Ti	1681	1562	<1650	2106	681	1713	2750	993
V	213	182	210	210	219	262	186	236
Cr	2672	2284	2576	2550	3437	3605	2556	3191
Co	44.9	37.8	37.6	49.3	54.2	61.5	47.2	45.8
Ni	64.3	69.3	54.3	60.4	114.0	101.0	63.1	84.6
Zn	65.2	58.8	52.6	76.8	54.5	–	82.3	–
Ga	4.17	4.22	<3.76	4.78	1.76	4.65	5.73	3.03
Rb	0.10	1.30	<2.25	0.10	0.02	0.53	0.13	0.80
Sr	0.67	1.54	<3.10	0.75	0.12	1.09	0.64	1.05
Y	3.76	4.61	<5.09	4.77	1.18	3.93	4.08	2.64
Zr	7.29	10.60	21.80	4.83	0.33	8.83	12.30	2.26
Nb	0.19	0.27	0.46	0.11	0.04	0.20	0.23	0.08
Cs	<0.011	0.11	<0.050	0.02	0.01	–	<0.011	–
Ba	0.40	2.00	<2.34	0.42	0.04	0.81	0.23	0.46
La	0.02	0.07	<0.16	0.03	0.01	0.05	0.03	0.02
Ce	0.07	0.19	<0.38	0.08	0.01	0.13	0.07	0.06
Pr	0.01	0.04	<0.068	0.02	<0.003	0.02	0.02	0.01
Nd	0.10	0.21	<0.44	0.12	<0.034	0.13	0.11	0.08
Sm	0.13	0.17	<0.32	0.14	0.03	0.14	0.13	0.08
Eu	0.04	0.07	<0.13	0.05	0.01	0.06	0.05	0.04
Tb	0.08	0.09	<0.14	0.09	0.02	0.07	0.07	0.05
Gd	0.30	0.46	<0.66	0.42	0.09	0.31	0.32	0.25
Dy	0.64	0.78	<0.89	0.76	0.15	0.60	0.63	0.44
Ho	0.14	0.19	<0.19	0.18	0.04	0.14	0.15	0.10
Er	0.44	0.56	<0.60	0.58	0.17	0.46	0.54	0.31
Yb	0.50	0.55	<0.57	0.58	0.18	0.53	0.58	0.33
Lu	0.08	0.09	0.11	0.10	0.04	0.08	0.10	0.05
Hf	0.26	0.31	0.63	0.17	0.02	0.29	0.54	0.09
Ta	0.01	0.01	<0.034	<0.004	<0.006	0.01	0.02	<0.002
Pb	0.03	0.08	<0.29	0.01	0.01	0.03	0.03	0.04
SiO2	51.9	51.9	51.6	50.2	53.4	52.9	53.2	52.7
TiO2	0.14	0.23	0.32	0.63	0.11	0.14	0.14	0.14
Al2O3	0.86	0.65	0.74	0.76	0.63	0.93	0.89	0.89
Cr2O3	0.41	0.28	0.37	0.12	0.53	0.55	0.42	0.51
MgO	19.9	19.2	17.8	13.5	23.3	21.7	22.0	21.3
CaO	5.84	5.02	5.34	6.09	3.98	6.18	5.12	5.70
MnO	0.60	0.67	0.65	0.82	0.52	0.49	0.55	0.61
FeO	19.5	22.2	22.5	27.6	16.3	17.1	17.8	17.3
Na2O	0.05	0.07	0.08	0.03	0.04	0.05	0.05	0.06
Sum	99.2	100.2	99.4	99.7	98.8	100.0	100.1	99.2

Major- and Trace-Element Chemistry of LithA Pyroxenes

Element	jn17d03	jn17d16	jn17d17	jn16c06
Sc	34.0	90.4	97.2	22.4
Ti	665	3363	3219	580
V	204	343	442	124
Cr	2886	3718	4722	2446
Co	41.0	43.7	48.6	42.6
Ni	95.5	116.0	62.5	112.0
Zn	44.0	65.9	77.1	–
Ga	1.94	8.24	8.88	1.61
Rb	<0.046	0.03	0.38	0.09
Sr	0.13	1.52	2.18	0.30
Y	1.38	9.23	8.73	1.23
Zr	0.48	16.30	31.30	1.03
Nb	0.04	0.09	0.62	0.04
Cs	0.03	0.02	0.04	–
Ba	0.03	0.15	1.43	0.13
La	<0.015	0.02	0.05	0.01
Ce	<0.016	0.13	0.17	0.03
Pr	<0.008	0.04	0.03	0.00
Nd	<0.083	0.29	0.32	0.04
Sm	<0.048	0.42	0.32	0.04
Eu	<0.016	0.12	0.12	0.01
Tb	0.02	0.22	0.18	0.02
Gd	<0.057	0.94	0.89	0.10
Dy	0.26	1.61	1.52	0.20
Ho	0.05	0.37	0.33	0.05
Er	0.15	1.08	1.02	0.15
Yb	0.25	0.96	1.02	0.16
Lu	0.03	0.16	0.16	0.03
Hf	<0.028	0.69	1.05	0.04
Ta	<0.013	<0.004	0.02	<0.003
Pb	<0.026	0.12	0.04	0.01
SiO2	52.3	50.9	51.2	54.3
TiO2	0.11	0.45	0.51	0.05
Al2O3	0.28	2.23	1.57	0.47
Cr2O3	0.41	0.74	0.63	0.42
MgO	24.6	15.1	13.8	26.0
CaO	3.83	14.2	15.8	2.57
MnO	0.61	0.48	0.48	0.54
FeO	15.7	15.4	15.0	15.9
Na2O	0.04	0.21	0.21	0.04
Sum	97.8	99.7	99.2	100.3

Major- and Trace-Element Chemistry of LithB Pyroxenes

Element	jn18b07	jn18b08	jn18b10	jn18b11	jn17a12	jn17a13	jn17a14	jn17a15
Sc	34.1	38.0	50.3	40.1	37.8	32.0	31.8	26.5
Ti	1168	2423	2121	973	858	806	850	528
V	152	174	165	227	204	180	158	157
Cr	2064	2314	1921	3121	2703	2526	2200	2780
Co	35.1	40.2	45.8	47.5	40.0	39.5	37.8	41.7
Ni	42.6	50.6	50.7	171.0	62.0	70.9	61.2	102.0
Zn	53.5	65.8	75.2	49.6	46.5	48.5	45.6	43.1
Ga	2.88	4.83	3.83	3.02	2.51	2.54	2.27	1.61
Rb	0.06	0.49	<0.046	0.12	0.06	1.60	0.14	0.04
Sr	0.31	3.23	0.30	1.10	0.56	1.02	0.63	0.16
Y	2.73	5.76	4.38	2.60	2.09	2.10	2.21	1.07
Zr	3.26	13.60	2.30	2.90	1.54	2.57	2.12	0.44
Nb	0.07	0.41	0.02	0.12	0.05	0.09	0.06	0.03
Cs	<0.019	0.04	<0.029	<0.020	0.01	0.10	<0.015	<0.018
Ba	0.13	2.68	0.09	0.42	0.17	0.48	0.28	0.03
La	0.02	0.12	<0.008	0.03	0.01	0.02	0.03	<0.007
Ce	0.05	0.29	0.04	0.11	0.03	0.08	0.08	0.01
Pr	0.01	0.06	<0.005	0.02	0.01	0.01	0.01	<0.005
Nd	0.08	0.33	0.09	0.11	0.04	0.09	0.08	0.03
Sm	0.07	0.25	0.16	0.08	0.06	0.07	0.09	0.03
Eu	0.02	0.08	0.03	0.03	0.02	0.03	0.02	0.01
Tb	0.05	0.12	0.09	0.05	0.04	0.04	0.04	0.02
Gd	0.19	0.61	0.36	0.29	0.17	0.18	0.18	0.05
Dy	0.40	0.91	0.82	0.43	0.37	0.33	0.36	0.16
Ho	0.11	0.20	0.16	0.10	0.09	0.08	0.09	0.04
Er	0.35	0.62	0.59	0.27	0.26	0.27	0.25	0.13
Yb	0.36	0.71	0.62	0.31	0.28	0.22	0.29	0.15
Lu	0.06	0.10	0.09	0.05	0.04	0.05	0.04	0.03
Hf	0.12	0.47	0.09	0.10	0.07	0.09	0.08	<0.019
Ta	<0.008	0.02	<0.008	<0.010	<0.003	0.00	<0.006	<0.005
Pb	0.03	0.14	<0.015	0.02	0.01	0.04	0.02	<0.014
SiO2	53.7	51.4	50.0	53.0	52.9	53.1	52.6	53.4
TiO2	0.09	0.35	0.63	0.10	0.12	0.08	0.10	0.10
Al2O3	0.63	0.87	0.64	0.60	0.85	0.56	0.61	0.73
Cr2O3	0.51	0.44	0.21	0.46	0.43	0.49	0.50	0.61
MgO	23.2	19.8	14.2	22.6	23.0	24.1	23.3	25.0
CaO	4.08	4.48	5.64	5.10	4.20	3.91	3.70	3.05
MnO	0.59	0.70	0.76	0.55	0.61	0.57	0.67	0.63
FeO	17.1	21.0	27.0	16.8	17.8	16.5	17.7	15.7
Na2O	0.04	0.07	0.05	0.04	0.06	0.09	0.06	0.07
Sum	100.0	99.1	99.2	99.3	99.9	99.4	99.1	99.3

Major- and Trace-Element Chemistry of LithB Pyroxenes

Element	jn17a16	jn17a17	jn17a18	jn17b03	jn17b07	jn17b08	jn17b10	jn17b11
Sc	39.1	74.3	38.3	36.0	38.9	50.2	38.6	35.3
Ti	755	3730	805	963	807	1507	922	702
V	234	128	212	198	215	266	219	220
Cr	3696	754	2767	2966	2996	3419	3482	4719
Co	54.1	49.1	44.5	51.1	46.3	56.6	57.5	75.4
Ni	123.0	48.6	71.5	103.0	88.3	87.1	129.0	254.0
Zn	56.3	128.0	50.7	58.3	52.1	72.9	61.6	75.4
Ga	2.10	6.96	2.59	2.50	2.36	3.98	2.87	2.04
Rb	<0.031	<0.030	0.11	0.08	<0.030	0.17	0.16	0.05
Sr	0.20	0.39	0.52	0.58	0.26	1.18	1.07	0.08
Y	1.55	3.80	2.55	2.26	2.00	4.29	2.21	1.03
Zr	0.65	7.60	1.95	1.87	0.85	4.71	2.21	0.35
Nb	0.04	0.02	0.06	0.07	0.04	0.13	0.07	0.05
Cs	<0.018	<0.015	0.02	<0.017	<0.011	0.02	0.02	<0.022
Ba	0.03	0.02	0.25	0.23	0.06	0.59	0.34	0.01
La	<0.006	0.01	0.03	0.02	0.01	0.07	0.02	<0.008
Ce	0.01	0.05	0.11	0.05	0.03	0.19	0.07	<0.009
Pr	<0.004	0.01	0.02	0.01	0.01	0.04	0.01	<0.005
Nd	<0.039	0.07	0.14	0.07	<0.035	0.23	0.08	<0.042
Sm	0.04	0.07	0.10	0.07	0.07	0.21	0.06	<0.067
Eu	0.01	0.05	0.05	0.03	0.02	0.06	0.03	<0.010
Tb	0.02	0.06	0.05	0.04	0.04	0.09	0.04	0.01
Gd	0.15	0.30	0.24	0.20	0.18	0.42	0.17	0.07
Dy	0.23	0.64	0.45	0.36	0.33	0.68	0.43	0.16
Ho	0.06	0.16	0.10	0.08	0.08	0.15	0.09	0.04
Er	0.17	0.52	0.31	0.27	0.24	0.51	0.26	0.12
Yb	0.19	0.71	0.30	0.25	0.27	0.52	0.28	0.12
Lu	0.04	0.13	0.05	0.05	0.05	0.08	0.05	0.02
Hf	0.03	0.38	0.08	0.08	0.03	0.20	0.08	0.03
Ta	<0.007	<0.005	<0.005	0.01	<0.005	0.01	<0.006	<0.009
Pb	<0.014	0.02	0.01	0.01	0.01	0.03	0.03	<0.015
SiO2	53.0	48.7	53.3	53.2	53.4	51.6	52.7	53.2
TiO2	0.13	0.70	0.13	0.29	0.11	0.30	0.23	0.05
Al2O3	0.74	0.67	0.73	0.90	0.77	0.94	1.02	0.49
Cr2O3	0.65	0.13	0.35	0.36	0.46	0.45	0.42	0.31
MgO	23.5	10.6	22.7	20.3	22.7	17.9	19.8	24.5
CaO	4.22	5.99	5.10	4.19	5.16	6.54	5.05	3.29
MnO	0.61	0.78	0.57	0.69	0.57	0.61	0.56	0.53
FeO	16.4	32.5	17.2	20.2	17.3	21.6	20.6	17.1
Na2O	0.07	0.05	0.04	0.06	0.08	0.08	0.08	0.07
Sum	99.3	100.1	100.1	100.3	100.5	100.0	100.5	99.6

Major- and Trace-Element Chemistry of LithB Pyroxenes

Element	jn17b12	jn17b13	jn17b14	jn17b16	jn17b18	jn17c03	jn17c04	jn17c05
Sc	36.4	65.5	30.0	52.9	32.5	40.0	50.1	35.4
Ti	875	2506	564	1132	644	1302	1269	911
V	215	203	180	270	188	201	205	170
Cr	3923	2131	2837	3124	2442	2572	2061	2036
Co	64.9	52.0	39.0	47.5	30.3	41.5	36.8	33.5
Ni	257.0	59.3	101.0	63.3	51.0	58.5	41.5	43.4
Zn	61.5	86.0	40.1	56.9	32.8	56.7	51.1	41.4
Ga	2.62	4.92	1.59	3.34	1.78	3.24	3.62	2.73
Rb	4.50	0.05	0.07	0.07	0.20	0.26	0.13	0.08
Sr	1.28	0.44	0.34	0.35	0.43	0.95	0.74	0.80
Y	1.78	5.51	1.28	2.93	1.83	4.49	3.54	2.38
Zr	2.60	2.14	0.40	1.24	0.86	5.51	1.73	1.97
Nb	0.09	0.03	0.03	0.04	0.03	0.11	0.03	0.06
Cs	0.15	0.01	0.01	0.01	0.01	0.02	<0.004	0.01
Ba	0.52	0.05	0.08	0.08	0.10	0.36	0.18	0.28
La	0.03	0.01	<0.004	0.01	0.01	0.09	0.01	0.02
Ce	0.09	0.04	0.02	0.03	0.03	0.24	0.03	0.06
Pr	0.01	0.01	0.00	0.01	0.00	0.04	0.01	0.01
Nd	<0.051	0.10	0.02	0.06	0.05	0.25	0.07	0.08
Sm	0.10	0.16	0.03	0.07	0.06	0.22	0.09	0.08
Eu	0.03	0.05	0.01	0.02	0.02	0.07	0.03	0.03
Tb	0.03	0.10	0.02	0.05	0.04	0.10	0.06	0.04
Gd	0.22	0.44	0.09	0.20	0.14	0.48	0.28	0.21
Dy	0.29	0.89	0.21	0.46	0.30	0.75	0.59	0.38
Ho	0.09	0.22	0.05	0.10	0.07	0.18	0.13	0.09
Er	0.21	0.70	0.15	0.37	0.23	0.50	0.45	0.29
Yb	0.22	0.75	0.16	0.40	0.24	0.49	0.52	0.29
Lu	0.05	0.12	0.03	0.06	0.04	0.08	0.07	0.05
Hf	0.10	0.13	0.02	0.07	0.05	0.18	0.09	0.08
Ta	<0.008	<0.003	<0.002	<0.002	<0.003	0.00	<0.004	0.00
Pb	0.06	0.01	0.01	<0.005	0.03	0.03	0.01	0.01
SiO2	53.3	48.3	54.1	52.1	53.3	52.0	52.1	53.8
TiO2	0.14	0.64	0.12	0.24	0.12	0.25	0.21	0.12
Al2O3	0.78	0.64	0.55	1.52	0.79	1.17	0.74	0.70
Cr2O3	0.48	0.09	0.42	0.42	0.49	0.43	0.18	0.43
MgO	24.3	9.5	24.6	19.6	23.0	18.8	18.0	23.3
CaO	3.77	6.43	3.37	5.49	4.60	4.74	4.50	3.75
MnO	0.53	0.85	0.63	0.70	0.59	0.65	0.78	0.60
FeO	16.5	32.7	16.9	19.8	16.7	21.8	22.9	16.9
Na2O	0.04	0.08	0.04	0.06	0.02	0.02	0.06	0.06
Sum	99.9	99.2	100.8	99.9	99.4	99.9	99.4	99.7

Major- and Trace-Element Chemistry of LithB Pyroxenes

Element	jn17c06	jn17c10	jn17c08	jn17b09	jn17b15	jn17b05	jn18b09	jn17b17
Sc	37.4	66.0	34.9	66.4	34.5	43.1	68.1	58.9
Ti	1002	2961	842	2387	1120	1390	5624	2880
V	185	155	164	261	154	162	241	123
Cr	2197	1281	1782	2759	2013	1523	2701	893
Co	34.6	44.2	17.3	52.3	38.8	39.1	57.1	31.5
Ni	47.0	52.4	23.8	66.8	67.5	49.8	58.6	48.4
Zn	45.3	104	22.2	84.2	48.9	57.0	114	80.2
Ga	2.76	6.16	3.43	5.63	2.67	3.28	9.05	6.11
Rb	0.30	0.04	0.05	1.13	0.26	0.14	0.30	0.42
Sr	0.81	0.65	1.50	1.15	0.78	0.90	1.16	1.45
Y	2.96	4.61	2.67	6.15	2.92	3.87	7.75	5.06
Zr	2.81	9.41	1.97	4.54	3.07	3.47	10.5	19.2
Nb	0.08	0.04	0.02	0.15	0.08	0.07	0.41	0.25
Cs	0.01	<0.012	<0.018	0.07	0.01	0.02	0.04	0.02
Ba	0.35	0.13	0.22	0.43	0.38	0.42	0.49	1.37
La	0.03	0.01	<0.008	0.05	0.04	0.04	0.05	0.03
Ce	0.09	0.04	0.04	0.14	0.09	0.12	0.14	0.10
Pr	0.02	0.01	0.01	0.03	0.02	0.02	0.03	0.02
Nd	0.13	0.08	0.06	0.24	0.12	0.15	0.21	0.16
Sm	0.11	0.14	0.12	0.22	0.11	0.14	0.21	0.19
Eu	0.04	0.04	0.05	0.07	0.04	0.05	0.07	0.07
Tb	0.06	0.08	0.04	0.12	0.06	0.07	0.15	0.11
Gd	0.29	0.41	0.29	0.57	0.28	0.34	0.79	0.45
Dy	0.51	0.80	0.46	1.00	0.50	0.71	1.40	0.88
Ho	0.12	0.17	0.10	0.23	0.11	0.14	0.30	0.21
Er	0.34	0.55	0.37	0.69	0.35	0.46	0.92	0.63
Yb	0.35	0.68	0.30	0.71	0.37	0.48	1.04	0.71
Lu	0.06	0.11	0.05	0.11	0.06	0.08	0.15	0.12
Hf	0.12	0.40	0.14	0.20	0.13	0.11	0.44	0.76
Ta	0.00	<0.005	<0.007	<0.006	0.00	<0.004	<0.011	0.01
Pb	0.02	0.03	<0.016	0.04	0.01	0.01	0.04	0.03
SiO2	53.6	49.7	53.1	51.0	54.0	53.5	50.6	54.7
TiO2	0.14	0.45	0.18	0.21	0.11	0.11	0.37	0.08
Al2O3	0.79	0.95	1.02	1.03	0.69	0.64	1.35	0.54
Cr2O3	0.50	0.36	0.47	0.56	0.43	0.41	0.36	0.64
MgO	22.3	12.4	20.6	17.8	23.7	22.8	14.1	26.3
CaO	5.30	6.98	5.88	8.50	3.98	4.50	8.02	2.34
MnO	0.63	0.68	0.62	0.54	0.57	0.46	0.65	0.47
FeO	17.0	27.7	18.1	19.7	16.8	18.2	24.4	15.0
Na2O	0.07	0.09	0.06	0.10	0.02	0.08	0.10	0.02
Sum	100.3	99.3	99.9	99.5	100.2	100.7	100.0	100.1

Major- and Trace-Element Chemistry of LithB Pyroxenes

Element	jn17c11	jn17c12	jn17c09	jn17c13	jn17c14	jn17c07	jn17b06
Sc	88.2	118.0	93.3	105.0	88.6	75.2	28.6
Ti	4157	5364	2956	3110	2826	1968	599
V	216	222	373	418	312	306	174
Cr	1958	1332	4129	4292	3151	3153	3695
Co	60.3	63.2	64.8	64.7	38.2	43.9	57.6
Ni	83.9	78.9	83.3	77.3	52.8	56.0	200
Zn	126	142	98.2	97.9	55.9	57.9	56.2
Ga	8.56	9.70	7.52	7.82	6.56	4.94	1.77
Rb	0.75	0.14	0.82	0.26	0.08	0.04	0.07
Sr	2.33	1.74	1.67	1.76	1.65	0.77	0.20
Y	7.82	8.55	8.76	8.94	8.55	6.01	1.01
Zr	21.6	11.9	9.19	7.92	7.50	2.46	0.58
Nb	0.41	0.13	0.24	0.14	0.05	0.03	0.04
Cs	0.04	<0.042	0.06	<0.053	<0.036	0.01	0.02
Ba	2.05	0.53	0.96	0.70	0.12	0.05	0.09
La	0.06	<0.026	0.05	0.05	0.04	0.01	0.01
Ce	0.18	0.09	0.19	0.16	0.15	0.06	0.02
Pr	0.04	0.02	0.03	0.02	<0.017	0.01	0.00
Nd	0.29	0.20	0.26	0.28	0.29	0.14	0.03
Sm	0.25	0.29	0.35	0.32	0.36	0.21	0.02
Eu	0.10	0.08	0.10	0.12	0.12	0.07	0.01
Tb	0.16	0.19	0.19	0.18	0.18	0.14	0.01
Gd	0.76	0.79	0.81	0.77	1.00	0.57	0.05
Dy	1.48	1.48	1.55	1.45	1.61	1.08	0.16
Ho	0.30	0.33	0.33	0.36	0.31	0.24	0.03
Er	0.92	1.02	1.00	1.09	1.01	0.70	0.13
Yb	1.19	1.24	1.00	0.98	1.02	0.73	0.17
Lu	0.20	0.21	0.15	0.15	0.15	0.11	0.02
Hf	0.91	0.56	0.34	0.36	0.45	0.16	0.03
Ta	0.02	<0.017	0.01	<0.035	<0.015	0.00	0.01
Pb	0.17	0.07	0.05	0.05	0.08	0.01	<0.013
SiO2	50.1	49.2	48.3	51.2	51.1	50.0	54.0
TiO2	0.56	0.56	0.64	0.31	0.42	0.52	0.0
Al2O3	0.90	0.88	2.21	1.83	1.25	0.96	0.4
Cr2O3	0.29	0.26	0.53	0.73	0.56	0.28	0.4
MgO	12.1	11.3	12.2	16.1	13.1	12.7	25.5
CaO	10.83	12.24	12.95	13.52	14.28	9.61	2.6
MnO	0.77	0.67	0.62	0.51	0.59	0.67	0.5
FeO	24.0	23.3	19.5	14.7	18.5	24.2	16.5
Na2O	0.10	0.12	0.15	0.13	0.15	0.11	0.0
Sum	99.7	98.6	97.1	99.1	99.9	99.0	100.1

Major- and Trace-Element Chemistry of LithA Maskelynite

Element	jn16a11	jn16a13	jn16a14	jn16a15	jn16a16	jn16a17
Sc	1.07	1.09	1.05	1.23	1.39	0.968
Ti	384	350	389	372	553	317
V	4.13	3.79	3.22	4.4	5.22	3.01
Cr	2.76	2.96	2.57	4.36	21.5	3.19
Mn	62.4	63.9	65.6	64.2	91.8	56.3
Co	0.623	0.69	0.57	1.01	0.86	0.48
Ni	0.829	1.38	1.34	3.98	1.66	0.559
Ga	43.5	44.5	44.5	33.6	66	43.9
Rb	7.96	2.17	0.916	1.12	4.16	0.21
Sr	78.9	74.7	71.6	73.3	89.4	70.2
Y	0.108	0.29	0.14	0.13	0.15	0.10
Zr	0.097	0.10	17.3	0.08	0.11	0.02
Nb	<0.0042	<0.0047	0.47	0.0053	<0.0029	<0.0020
Ba	7.09	8.22	5.85	5.85	16.8	5.24
La	0.05	0.05	0.04	0.05	0.04	0.04
Ce	0.09	0.16	0.09	0.08	0.10	0.08
Pr	0.01	0.02	0.01	0.01	0.01	0.01
Nd	0.05	0.08	0.06	0.08	0.07	0.07
Sm	<0.020	<0.023	<0.034	<0.018	0.08	0.02
Eu	0.78	0.74	0.74	0.69	0.88	0.76
Tb	<0.0041	0.01	0.01	0.01	<0.0034	0.01
Gd	0.06	0.07	0.05	0.02	0.03	0.04
Dy	0.04	0.05	0.03	0.05	0.03	<0.018
Ho	0.00	0.01	0.01	0.01	0.01	<0.0042
Er	<0.012	0.06	0.02	<0.013	0.02	0.01
Yb	<0.030	<0.017	<0.021	<0.028	<0.023	<0.021
Lu	<0.0041	0.00	<0.0046	<0.0032	<0.0027	<0.0051
Hf	<0.014	<0.0048	0.55	<0.012	<0.015	<0.012
Ta	<0.0036	<0.0035	0.01	<0.0042	<0.0071	<0.0037
Pb	0.04	0.08	0.06	0.05	0.13	0.04
Th	<0.012	<0.0064	<0.0071	0.01	<0.0073	<0.010
U	<0.0066	<0.0047	<0.0063	<0.0060	<0.0037	<0.0050
SiO2	53.1	53.7	52.7	54.7	53.9	53.2
Al2O3	29.6	29.1	29.2	28.2	29.1	29.2
MgO	0.1	0.1	0.1	0.1	0.1	0.2
CaO	12.5	11.9	12.0	10.8	11.6	11.9
FeO	0.7	0.6	0.6	0.5	0.5	0.5
Na2O	4.0	4.5	4.4	5.0	4.7	4.4
K2O	0.2	0.2	0.2	0.2	0.2	0.1
Sum	100.1	100.1	99.2	99.6	100.2	99.4

Major- and Trace-Element Chemistry of LithA Maskelynite

Element	jn16a18	jn16b03	jn16b04	jn16b05
Sc	1.03	0.976	1.18	0.939
Ti	319	402	335	306
V	3.54	2.62	3.7	3.03
Cr	2.91	1.69	2.39	2.32
Mn	62.3	52.1	69.7	52.6
Co	0.58	0.57	0.69	0.54
Ni	0.845	1.48	1.4	1.07
Ga	43.5	48.4	46	40.7
Rb	0.63	5.01	2.39	0.63
Sr	72.1	79.6	72.4	65.9
Y	0.10	0.11	0.90	0.17
Zr	0.02	0.40	0.19	0.03
Nb	<0.0026	0.0068	0.01	<0.0029
Ba	5.4	13.7	8.55	5.71
La	0.05	0.05	0.10	0.05
Ce	0.08	0.10	0.32	0.10
Pr	0.01	0.01	0.04	0.01
Nd	0.04	0.07	0.19	0.06
Sm	0.02	<0.024	0.09	0.03
Eu	0.75	0.81	0.74	0.70
Tb	0.01	0.01	0.03	0.01
Gd	0.03	0.02	0.17	0.04
Dy	0.02	0.04	0.11	0.04
Ho	0.01	0.01	0.04	0.01
Er	<0.0080	<0.013	0.07	0.02
Yb	<0.014	<0.036	0.11	0.01
Lu	<0.0032	<0.0027	0.01	<0.0028
Hf	<0.0080	<0.0092	<0.0077	<0.0097
Ta	<0.0038	<0.0060	<0.0059	<0.0031
Pb	0.04	0.08	0.09	0.06
Th	<0.0052	<0.0093	0.01	0.00
U	<0.0038	<0.0048	0.01	<0.0049
SiO2	53.5	53.7	52.7	54.8
Al2O3	28.9	28.7	29.5	28.4
MgO	0.19	0.1	0.1	0.1
CaO	12.1	11.5	12.0	10.9
FeO	0.76	0.5	0.4	0.6
Na2O	4.60	4.6	4.4	5.0
K2O	0.12	0.2	0.1	0.2
Sum	100.2	99.4	99.2	100.0

Major- and Trace-Element Chemistry of LithB Maskelynite

Element	jn16b06	jn16b07	jn16b08	jn16b09	jn16b10	jn16b11	jn16b12	jn16b13
Sc	1.03	0.757	1.1	1.04	1.05	0.856	1.14	1.11
Ti	315	286	484	313	308	413	385	364
V	3.39	3.34	2.33	3.41	3.23	1.85	3.81	3.1
Cr	2.82	<1.81	3.43	4.29	3.52	1.78	2.51	3.45
Mn	77.4	56.2	73.9	71.9	75	52.7	83.9	72.8
Co	1.07	0.50	0.76	0.67	0.58	0.48	0.71	0.71
Ni	7.33	0.85	1.81	1.27	0.94	0.838	1.67	2.14
Ga	43.8	35.4	81.9	42.6	47.2	60.6	42.5	57.7
Rb	2.02	0.247	5.79	0.33	0.634	1.05	0.862	2.53
Sr	68.4	64.9	106	67.8	68.4	74	70.3	78.7
Y	0.14	0.09	0.11	0.11	0.09	0.08	0.47	0.77
Zr	0.84	0.04	0.37	0.06	0.06	0.04	0.21	0.61
Nb	0.03	<0.0064	0.01	0.00	<0.0026	<0.0033	0.02	0.01
Ba	9.3	4.69	22.8	5.12	6.11	10.5	5.96	15.1
La	0.05	0.04	0.03	0.04	0.03	0.04	0.07	0.07
Ce	0.08	0.08	0.07	0.07	0.07	0.05	0.16	0.23
Pr	0.01	0.01	0.01	0.01	0.01	0.00	0.02	0.04
Nd	0.05	0.06	0.05	0.06	0.06	0.06	0.19	0.16
Sm	0.03	<0.046	<0.025	<0.037	<0.020	0.03	0.05	0.08
Eu	0.64	0.74	0.86	0.75	0.71	0.76	0.78	0.76
Tb	0.01	<0.0043	0.01	0.00	0.01	0.00	0.02	0.02
Gd	0.04	0.03	0.05	0.05	0.04	<0.030	0.08	0.12
Dy	0.03	<0.017	0.02	<0.020	0.03	0.01	0.17	0.13
Ho	0.00	<0.0075	<0.0043	0.01	0.00	<0.0059	0.03	0.03
Er	<0.012	0.04	<0.013	<0.014	<0.0094	<0.012	0.07	0.05
Yb	<0.015	<0.038	<0.027	<0.023	<0.017	<0.027	<0.038	0.05
Lu	0.00	<0.0052	<0.0039	<0.0038	<0.0036	<0.0052	0.01	<0.0057
Hf	0.03	<0.027	0.02	<0.014	<0.0099	<0.019	0.02	0.02
Ta	<0.0029	<0.013	<0.0046	<0.0065	<0.0045	<0.0068	<0.0067	<0.0068
Pb	0.12	0.02	0.17	0.09	0.06	0.04	0.05	0.22
Th	<0.0099	<0.0051	<0.011	<0.0055	<0.0054	<0.011	<0.010	0.01
U	<0.0054	<0.011	<0.0069	<0.0046	<0.0046	<0.0076	<0.0076	0.00
SiO2	53.7	54.2	52.6	53.7	53.9	56.3	53.6	52.6
Al2O3	28.8	28.9	29.8	28.9	29.5	27.4	29.0	29.7
MgO	0.1	0.1	0.2	0.2	0.1	0.1	0.2	0.1
CaO	11.2	11.8	13.0	12.3	12.1	10.0	12.1	12.2
FeO	0.5	0.5	0.5	0.9	0.4	0.9	0.7	0.5
Na2O	4.7	4.5	3.8	4.1	4.2	5.2	4.4	4.1
K2O	0.1	0.1	0.1	0.1	0.1	0.2	0.1	0.2
Sum	99.3	100.0	100.0	100.2	100.3	100.2	100.2	99.5

Major- and Trace-Element Chemistry of LithB Maskelynite

Element	jn16b14	jn16b15
Sc	1.05	1.04
Ti	347	389
V	3.58	2.6
Cr	2.91	2.56
Mn	72.2	63.6
Co	0.57	0.48
Ni	1.05	0.723
Ga	49	58
Rb	0.362	1.86
Sr	72.4	76.9
Y	0.25	0.12
Zr	0.12	0.04
Nb	0.00	<0.0019
Ba	5.87	9.59
La	0.06	0.04
Ce	0.16	0.08
Pr	0.02	0.01
Nd	0.12	0.07
Sm	0.05	0.03
Eu	0.78	0.82
Tb	0.01	<0.0047
Gd	0.07	0.03
Dy	0.05	0.02
Ho	0.01	<0.0039
Er	0.03	0.01
Yb	0.03	<0.024
Lu	0.00	<0.0057
Hf	<0.0090	<0.0098
Ta	–	<0.0034
Pb	0.04	0.06
Th	<0.0044	<0.0058
U	<0.0063	<0.0029
SiO2	52.9	53.8
Al2O3	29.1	29.1
MgO	0.1	0.1
CaO	12.1	11.4
FeO	0.5	0.6
Na2O	4.3	4.6
K2O	0.1	0.2
Sum	99.2	99.7

Major- and Trace-Element Chemistry of LithA Olivine Megacrysts

Element	jn18b15	jn18b18	jn18b17	jn18a11	jn18a17	jn18a13
Sc	9.13	20.7	8.26	9.83	8.29	9.51
Ti	73.9	4186	74.8	51.4	127	52.9
V	14.7	62.8	14.1	18.9	11.6	20.7
Cr	296	1362	251	385	251	517
Co	90.7	83.7	86.5	89.9	85.6	90.2
Ni	245	164	210	248	285	285
Zn	95	92.7	97	95.5	78.2	97.5
Ga	0.39	2.73	0.31	0.55	0.47	0.66
Rb	<0.033	0.036	<0.027	<0.042	<0.041	<0.030
Sr	0.05	5	0.021	<0.011	0.026	0.023
Y	0.17	34	0.17	0.18	0.1	0.19
Zr	0.15	45.4	0.1	<0.041	1.03	0.044
Nb	0.012	1.46	<0.008	<0.011	0.014	0.008
Cs	<0.014	<0.015	<0.015	<0.018	0.02	<0.012
Ba	0.042	0.29	0.012	<0.009	0.045	0.012
La	<0.006	1.36	<0.005	<0.006	<0.009	<0.005
Ce	0.004	3.68	<0.006	<0.011	<0.006	<0.006
Pr	<0.006	0.6	<0.004	<0.006	<0.009	<0.003
Nd	<0.022	3.28	<0.029	<0.036	<0.045	<0.025
Sm	<0.026	2.45	<0.023	<0.032	<0.030	<0.034
Eu	<0.007	0.8	0.013	<0.006	<0.010	<0.007
Tb	<0.006	0.91	<0.004	<0.007	<0.005	<0.003
Gd	<0.027	5.27	<0.016	<0.050	<0.027	<0.014
Dy	0.022	6.79	<0.029	<0.026	<0.019	0.018
Ho	<0.007	1.34	0.008	0.009	<0.007	0.006
Er	0.021	4.04	0.027	0.042	0.026	0.022
Yb	0.062	3.46	0.052	0.076	<0.040	0.051
Lu	0.011	0.53	0.013	0.015	0.011	0.013
Hf	<0.017	1.99	<0.019	<0.021	0.076	<0.013
Ta	<0.005	0.099	<0.006	<0.008	<0.009	<0.006
SiO2	35.4	35.2	35.7	35.6	36.1	35.9
Cr2O3	0.07	0.00	0.08	0.08	0.05	0.07
MgO	25.5	26.2	27.2	27.7	29.2	29.4
CaO	0.30	0.24	0.24	0.27	0.27	0.26
MnO	0.73	0.66	0.66	0.65	0.60	0.60
FeO	38.3	38.8	36.9	36.6	34.5	34.5
Sum	100.4	101.1	100.7	100.8	100.7	100.7

Major- and Trace-Element Chemistry of LithA Olivine Megacrysts

Element	jn18a18	jn18b05	jn18a12	jn18b13	jn18b06	jn18b16	jn18b14	jn18a16
Sc	11.1	8.14	8.96	8.23	7.41	7.55	7.29	6.45
Ti	37.3	47	51.4	78	41.9	42.9	28.6	29.6
V	21.4	14.1	23.2	13.2	17	12.5	17.1	13.3
Cr	464	304	595	320	352	262	356	327
Co	87.5	82.5	90.9	84.7	84.1	77.5	81.2	83.8
Ni	279	293	360	326	321	255	396	399
Zn	84.1	83.3	97.3	86.4	76.7	78.5	70.7	75
Ga	0.49	0.45	0.69	0.33	0.38	0.34	0.32	0.27
Rb	<0.014	<0.027	<0.026	<0.027	<0.049	<0.022	<0.016	<0.037
Sr	0.022	0.037	0.028	<0.006	<0.009	0.027	0.035	<0.010
Y	0.23	0.15	0.18	0.17	0.12	0.15	0.13	0.074
Zr	0.072	0.03	0.049	0.021	<0.035	0.038	0.053	<0.033
Nb	0.007	<0.005	0.008	<0.006	<0.013	<0.009	0.008	<0.014
Cs	<0.006	<0.009	<0.014	<0.014	<0.021	<0.010	<0.012	<0.025
Ba	0.031	0.067	0.03	<0.007	0.019	0.022	0.021	<0.013
La	<0.004	<0.004	<0.008	<0.006	<0.010	<0.005	<0.005	<0.011
Ce	<0.003	<0.004	<0.006	<0.003	<0.010	0.005	<0.005	<0.008
Pr	<0.002	<0.002	<0.004	<0.003	<0.005	<0.003	<0.004	<0.006
Nd	<0.016	<0.020	<0.026	<0.023	<0.028	<0.024	<0.022	<0.027
Sm	<0.020	<0.016	<0.019	<0.023	<0.047	<0.034	<0.033	<0.043
Eu	<0.005	<0.005	<0.007	<0.007	<0.010	<0.005	<0.008	<0.011
Tb	0.003	<0.004	<0.004	<0.004	<0.004	<0.002	<0.005	<0.008
Gd	<0.010	<0.019	<0.037	<0.013	<0.029	<0.017	<0.017	<0.041
Dy	0.022	<0.013	0.016	0.016	<0.017	<0.021	<0.015	<0.030
Ho	0.008	0.004	0.007	<0.006	<0.008	0.006	<0.004	0.007
Er	0.045	0.028	0.024	0.029	0.022	0.028	0.016	<0.025
Yb	0.065	0.064	0.054	0.075	<0.037	0.048	0.033	<0.036
Lu	0.013	0.012	0.011	0.013	<0.006	0.007	0.01	<0.006
Hf	0.007	<0.014	<0.017	<0.015	<0.026	<0.012	<0.012	<0.023
Ta	<0.002	<0.004	<0.006	<0.004	<0.008	<0.005	<0.006	<0.006
SiO2	35.7	36.1	36.4	36.7	36.8	36.6	38.1	37.6
Cr2O3	0.12	0.02	0.07	0.03	0.05	0.05	0.05	0.01
MgO	29.7	30.0	30.9	30.7	32.5	32.7	34.4	35.3
CaO	0.26	0.26	0.24	0.25	0.28	0.19	0.23	0.19
MnO	0.61	0.60	0.55	0.60	0.50	0.53	0.49	0.52
FeO	34.2	33.7	32.8	31.9	30.7	30.2	26.6	27.2
Sum	100.6	100.6	101.0	100.1	100.8	100.2	99.9	100.8

Major- and Trace-Element Chemistry of LithA Olivine Megacrysts

Element	jn18c03	jn18b03	jn18a14	jn18b04	jn18a15
Sc	7.46	7.75	6.75	7.81	6.48
Ti	38.4	41.5	30.7	43.9	26.1
V	35	37.3	18.8	47.2	28.9
Cr	2050	1607	596	2370	1720
Co	75.7	82	80.8	78.3	81.2
Ni	401	419	417	411	493
Zn	78.6	66.2	67.4	60.6	65.2
Ga	0.67	0.5	0.37	0.51	0.45
Rb	<0.013	<0.019	<0.023	<0.013	<0.039
Sr	0.066	0.016	0.016	0.014	0.019
Y	0.14	0.11	0.07	0.12	0.072
Zr	0.042	0.029	0.029	0.065	0.031
Nb	0.02	0.012	0.012	0.026	0.021
Cs	<0.008	<0.010	<0.013	<0.007	<0.012
Ba	0.016	0.028	0.031	0.021	0.029
La	<0.003	<0.004	<0.006	<0.003	<0.005
Ce	<0.002	<0.004	<0.004	<0.003	<0.007
Pr	<0.002	<0.002	<0.005	<0.002	<0.004
Nd	<0.008	<0.022	<0.030	<0.015	<0.022
Sm	<0.014	<0.012	<0.030	<0.015	<0.023
Eu	<0.003	<0.005	<0.005	<0.005	<0.006
Tb	<0.002	0.003	<0.003	0.002	<0.004
Gd	<0.010	<0.013	<0.014	<0.015	<0.024
Dy	0.018	0.019	0.018	0.017	<0.016
Ho	0.003	0.004	<0.004	<0.004	<0.004
Er	0.025	0.014	0.017	0.018	<0.016
Yb	0.034	0.032	<0.022	0.045	<0.022
Lu	0.008	0.008	<0.006	0.008	0.005
Hf	<0.007	<0.009	<0.013	<0.010	<0.009
Ta	<0.002	<0.005	<0.005	<0.004	<0.004
SiO2	37.6	37.9	38.0	38.1	38.5
Cr2O3	0.09	0.09	0.07	0.08	0.10
MgO	36.4	37.3	37.2	38.1	38.9
CaO	0.22	0.26	0.22	0.18	0.19
MnO	0.45	0.46	0.42	0.45	0.42
FeO	26.9	24.8	24.6	23.7	22.4
Sum	101.7	100.8	100.6	100.5	100.6

VITA

Michael Mellin was raised in the small town of Kuna, Idaho and graduated from Kuna High School in 1996. He then attended the University of Idaho and graduated with a B.S. in Geology from the University of Idaho. From there he worked as a Field Geologist in San Francisco, CA and Knoxville, TN. Michael obtained his M.S. in Geology at the University of Tennessee, and is currently pursuing a career in economic geology.